Phase Transformation Kinetics and Microstructure of Carbide and Diboride Based Ceramics

Dissertation
of the requirements for the Degree
of Doctor of Engineering
submitted by

Edith Roland Fotsing

from Bamendjou (Cameroon)

Approved by the
Fakultät für Bergbau, Hüttenwesen und Maschinenwesen
of the Technische Universität Clausthal

Day of the oral examination

March 15, 2005

Vorsitzender der Promotionskommission: Prof. Dr. rer. nat. A. Wolter
Hauptberichterstatter: Prof. Dr.-Ing. G. Borchardt
Berichterstatter: Prof. Dr.-Ing. J. G. Heinrich

Table of contents

List of physical symbols

α [°]	Contact angle between the nucleus and the surface of the grain boundary.
θ [°]	Bragg angle
λ [Å]	Wavelength
σ [Jm^{-2}]	Interfacial energy
ν [s^{-1}]	effective attempt frequency (~ 10^{13} s^{-1})
ρ [m^{-1}]	Density of the grain boundary
a [Å]	Width of the grain boundary
FWHM [°]	Full width at half maximum of the characteristic XRD reflex
C_m [at. %]	Concentration of a species in the matrix
C_p [at. %]	Concentration of a species in the precipitate
C_s [at. %]	Concentration of a species at the matrix-precipitate interface
d_{hkl} [Å]	Inter-planar spacing (distance between two atomic planes)
D_B [m^2s^{-1}]	Diffusion coefficient at the grain boundary
D_V [m^2s^{-1}]	Diffusion coefficient in the volume
ΔG^* [eV]	Gibbs free energy of nucleation
ΔG [eV]	Total Gibbs free energy difference
ΔG_v [eV]	Gibbs free energy difference due to the volume
ΔH_T [eV]	Total activation enthalpy
ΔH_g [eV]	Activation enthalpy of growth
ΔH_D [eV]	Activation enthalpy of diffusion
ΔH_N [eV]	Activation enthalpy of nucleation
ΔH_{SD} [eV]	Activation enthalpy of self-diffusion
h [µm]	Thickness of cylindrical precipitates
I(T) [$m^{-3}s^{-1}$]	Nucleation rate
I_B(T) [$m^{-2}s^{-1}$]	Nucleation rate at grain boundaries
I_V(T) [$m^{-3}s^{-1}$]	Nucleation rate in the volume
J_V [$m^{-2}s^{-1}$]	Atom flux in the volume
J_B [$m^{-2}s^{-1}$]	Atom flux at grain boundaries
k(T) [s^{-1}]	Rate constant
k_B [JK^{-1}]	Boltzmann constant
N(T) [m^{-3}]	Density of nuclei
N_0 [m^{-3}]	Density of pre-existing nuclei (see SiC films)
N_B	Number of precipitates at the grain boundary

N_V	Number of precipitates in the volume
N_{0V} [m^{-3}]	Density of pre-existing nuclei in the volume
N_{0B} [m^{-2}]	Density of pre-existing nuclei at the grain boundary
n(t)	JMAK exponent
r* [nm]	Radius of crystallites after the first crystallisation stage of SiC films.
R(t) [µm]	Time dependent radius
$R_c(t)$ [µm]	Critical radius of a crystallite
T [°C]	Temperature
t [s]	Time
t* [s]	Annealing time corresponding to experimental data point, where the two processes overlap (for more detail see crystallisation kinetics of amorphous SiC films)
Δt [s]	Duration of the precipitation (see diboride solid solutions)
U(T,t) [ms^{-1}]	Growth rate
U_0 [ms^{-1}]	Pre-exponential factor of the thermally activated growth rate
V_0 [m^3]	Total volume
V^e [m^3]	Extended volume
V^t [m^3]	Transformed volume
$X^e(T,t)$	Extended volume fraction
X(T,t)	Crystallised volume fraction
$Y_V(t)$	Precipitated fraction in the volume

List of abbreviations

CVD	Chemical vapour deposition
CS	Combustion synthesis
DSC	Differential scanning calorimetry
DTA	Differential thermal analysis
EDS	Energy dispersive X-ray spectroscopy
EDX	Energy dispersive X-ray diffraction
GB model	Grain boundary model
HRTEM	High resolution transmission electron microscopy
IFACS	Induction field activated combustion synthesis
JMAK	Johnson-Mehl-Avrami-Kolmogorov model
LPD	Liquid phase deposition
MBE	Molecular beam epitaxy
PIPS	Precision ion polishing system
SEM	Scanning electron microscopy
SAD	Selected area of diffraction of a crystalline SiC film
TEM	Transmission electron microscopy
XRD	X-ray diffraction

1. Summary

The present work deals with the crystallisation kinetics of thin amorphous SiC films deposited on crystalline silicon and glassy carbon substrates via a r. f. magnetron sputtering technique as well as with the precipitation kinetics of transition metal diboride solid solutions.

Amorphous silicon carbide films sputtered on crystalline silicon substrates were investigated in the temperature range between 1200 °C and 1350 °C under argon atmosphere. XRD diagrams as well as the electron diffraction patterns of the annealed SiC films led to the conclusion that the amorphous SiC films crystallised in the ß-SiC structure.

TEM experiments on cross-sectioned samples showed spherical crystallites with an average diameter between 30 and 70 nm, which indicates a three-dimensional growth process. Under the assumption that the volume of the crystallised phase is proportional to the integrated intensity of the Bragg peaks, a two-step behaviour of the crystallisation kinetics was obtained. Values of JMAK exponents between 1.6 and 2.5, obtained with the classical JMAK model, are in contradiction to the TEM measurements. In order to determine kinetic parameters, a modified JMAK model describing the isothermal transformation of amorphous SiC into ß-SiC has been proposed. This model, based on the assumption of pre-existing crystallites, enables the determination of growth rates for three-dimensional crystallites formed in the earlier stage of the process. Moreover, the obtained thermally activated rate constants of growth obeyed an Arrhenius behaviour leading to an overall activation enthalpy of growth of (4.1 ± 0.7) eV. This value coincides within error margins with the overall activation enthalpy of crystallisation found in the literature and suggests that growth plays the determinant role in the crystallisation of SiC films.

Regarding the SiC films deposited on carbon substrates, conclusions concerning the structure of the crystallised phase are mostly the same. However, an increase of the stability of the SiC films is observed. The value of the JMAK exponent ($n = 1$) is also in contradiction with TEM observations. Therefore, the kinetics was interpreted by the same modified JMAK model used in the case of silicon substrates. The rate constants of growth obtained by the proposed model led to an activation enthalpies of (8.9 ± 0.9) eV.

The faster crystallisation behaviour of the films on silicon substrates is expected to be due to presence of superabundant points defects, which diffuse from the substrate into the film and accelerate the incorporation of atoms from the amorphous into the crystalline phase. Investigations on amorphous films with nominal composition $Si_{0.33}C_{0.66}$ deposited on Si substrates result approximately in the same activation enthalpy of crystallization of (4.6 ± 1.5) eV as for the SiC films for this diffusion controlled process. The difference between the activation enthalpy of crystallisation for the films deposited on the silicon substrate and those deposited on the glassy carbon substrate indicates clearly a direct influence of substrates on the crystallisation kinetics.

The second part of the present thesis deals with the investigation of the precipitation kinetics and the microstructure in the supersaturated solid solution (Ti, W, Cr)B_2. A comparative study was done with respect to the influence of the composition and of Co impurities on the precipitation process. Two groups of samples with nominal composition $(Ti_{0.3}W_{0.5}Cr_{0.2})B_2$ and $(Ti_{0.4}W_{0.5}Cr_{0.1})B_2$ were investigated at temperatures between 1450 °C and 1700 °C under argon atmosphere. After annealing, a secondary phase with W_2B_5 structure is precipitated with platelet-like morphology. SEM measurements proved that, for all types of samples, nuclei at the grain boundaries were the starting point of further growth into the volume in a two-dimensional growth process.

Least-squares fitting of the time dependent experimental data to the classical JMAK equation led to JMAK exponents between 1.4 and 1.8, which could not satisfactorily explain the two-dimensional growth observed on SEM micrographs. A modified JMAK model based on heterogeneous nucleation at grain boundaries and diffusion controlled growth within the bulk was proposed. A continuous decrease of the JMAK exponent from $n = 2$ to $n = 0.5$ during the precipitation process is found as a result of the simulations. The comparison of the time dependence of the precipitation kinetics with the proposed model enabled the determination of the thermally activated nucleation rate at the grain boundaries with an activation enthalpy of nucleation of (3.6 ± 0.3) eV. The measurement of the size of the precipitates as a function of annealing time and temperature allows to determine an activation enthalpy of growth of (3.6 ± 0.3) eV in accordance with tracer self-diffusion measurements. Moreover, the temperature dependent rate constants determined using the classical JMAK model led also to a total activation enthalpy of (3.4 ± 0.5) eV.

Samples without chromium did not present any precipitation. The activation enthalpies obtained with samples containing 20 at. % Cr and those with 10 at. % Cr show identical rate constants. Impurity Co atoms were found to introduce pre-existing nuclei, which may help to enhance the particle density without influencing the kinetics of the precipitation process.

2 Introduction

The properties of materials depend on chemical composition and microstructure. Thus, the common way to improve materials properties is the control of changes of the composition and/or the microstructure [Cah99]. An understanding of phase transformation led progressively to the improvement of the processing conditions and consequently to that of the material properties [Chr75]. In physical metallurgy, crystallisation, grain growth and hardening of ceramics as consequences of the phase transformations were optimised [Kin60].

As experimental procedures for the study of the kinetics of phase transformations two ways were adopted: the non-isothermal transformation at constant heating rate which led to a rapid expansion of DSC (Differential Scanning Calorimetry) or DTA (Differential Thermal Analysis) combined with thermogravimetric analysis. The second procedure is the isothermal transformation method where a continuous thermal treatment was made at constant temperature. For each experimental method a suitable model for the evaluation of the kinetic and thermodynamic parameters was needed.

The first model has been introduced by Johnson and Mehl followed by Avrami and Kolmogorov around 1940. This model (JMAK) was based on the combination of three specific partial processes, namely the nucleation, the growth and the impingement of growing particles, and was convenient to describe isothermal transformation. This model may enable the determination of kinetic parameters such as the rate constant, the Avrami exponent and the activation enthalpy. The nucleation considered can be continuous or discontinuous. Site saturation can also be observed, i.e. all nuclei were present before the growth started. The growth could be diffusion controlled or interface controlled, depending on the type of transformation. The impingement considered was hard impingement, i.e. spatial interaction of homogeneously dispersed particles. This model has been widely adopted, but its general applicability is still under discussions. The simple JMAK model was be applied in many cases although some basic assumptions in the derivation of the model did not always hold, and led to erroneous results. A generalisation of the JMAK model for the non-isothermal case [Vas00] or by assuming an isokinetic range of temperatures and concentrations where an additive rule could be applied [Zha00], led to the Ozawa or Kissinger model [Kis57], [Kis57], [Oza71], which enabled the investigation of non-isothermal transformations.

Despite of the important advances in the measurement methods as well as in the determination of the kinetic parameters of the phase transformations, several areas of this research field still need more attention. For instance, the high crystallisation or precipitation temperature of some non-oxyde ceramics does not enable the use of DSC or DTA to follow this process. In this case a cyclic thermal treatment consisting of isothermal annealing followed by rapid quenching has to be considered. Furthermore, a complete kinetic theory dealing with heterogeneous nucleation is not available. Therefore, the kinetics has to be separately derived, depending on the complexity of each system. The present thesis is concerned with the investigation of the phase transformation kinetics and the microstructure of SiC films and of transition metal diborides at high temperatures and under isothermal conditions. Recognising and describing precisely the phase transformation governing each of the above systems, adequate kinetic models based on the JMAK model have been proposed to evaluate the kinetic parameters. In particular, a general kinetic model taking into account the contribution of the grain boundaries to the precipitation kinetics of diboride based materials has been introduced, and a direct comparison to classical JMAK model has been performed.

In order to follow the evolution of the crystallisation or the precipitation as well as of the microstructure, XRD (X-ray diffraction), EDX (energy dispersive X-ray analysis), SEM (scanning electron microscopy), TEM (transmission electron microscopy) were particularly useful.

3 Literature overview

3.1 Amorphous silicon carbide films

Silicon carbide (SiC) is the only binary compound of silicon and carbon which exists as a solid phase [Ell65] and also the most used non-metallic hard material. Polishing devices as well as coatings and heating elements for high temperature furnaces are classical applications of SiC. Several methods have been used to produce SiC in commercial quantity. Besides the conventional and classical powder ceramic methods [Rie96], new methods based on the pyrolysis and thermolysis of pre-ceramic polymers at temperature of about 1000 °C were proposed for the fabrication of SiC [Rie96], [Bil00], [Kur99]. The resulting silicon carbide is amorphous, free of sinter additives and characterised by a high purity and homogeneous elemental distribution.

The use of Chemical Vapour Deposition (CVD) [Nis80], [Nis83], Molecular Beam Epitaxy (MBE) [Fuy89] and Liquid Phase Deposition (LPD) led for the first time to the growth of pure stoichiometric SiC single crystal films with definite polytype and with special doping elements on silicon or silicon carbide substrates. Further development of CVD for the growth of SiC films on diverse substrates is the diode or radio frequency (r. f.) magnetron sputtering technique which presents some advantages such as smaller grain size and a better adhesion [Lut98].

Another preparation method of amorphous SiC films based on spin or dip coating routes using liquid poly(carbo)silane followed by a thermolysis in an inert atmosphere was also proposed [Hei97], [Hei96].

Amorphous silicon carbide (a-SiC) films have found growing interest due to the potential applications for optoelectronic devices [Pow88], where the optical and electronic properties of a-SiC films can be tailored by tuning the defect density. For instance, hydrogen incorporation decreases the defect density down to 10^{17} cm^{-3} and leads to high photoluminescence yield at room temperature. Therefore, hydrogenated amorphous silicon carbide films (a-SiC:H) are suitable for visible light emission diodes (LEDs) [Nas82], [Ham88]. Interesting applications of amorphous silicon carbide are also membranes for high temperature pressure sensors and heat conducting thin films [Kle01].

Since about 1980, the interest in using SiC as a semiconductor material, due to its wide band gap (2.2-3.3 eV), has considerably increased.

The crystalline form of SiC (c-SiC) presents attractive physical properties, i.e. high temperature of fusion, high thermal conductivity (4.9 $Wcm^{-1}K^{-1}$), high electron mobility, large breakdown electric field strength (2.2×10^6 V cm^{-1}) and a high electron drift velocity

(2.0 x 10^7 cms^{-1}). It is the most suitable semiconductor material for high temperature or/and high frequency applications (Table 3.1) [Pow92], [Dav93], [Iva95], [Pal88], [Ruf94].

Only some authors investigated the crystallisation behaviour of amorphous SiC films deposited via CVD [Cal01] or the r.f. magnetron sputtering [Sho87] in order to determine related kinetic parameters (JMAK exponent and rate constants).

Table 3.1: *Comparison of the properties of 3C-SiC, 6H-SiC, Si, GaN and diamond [Dav93].*

	3C-SiC	6H-SiC	Si	GaAs	GaN	Diamond
Band gap [eV]	2.3	3.0	1.1	1.4	3.4	5.5
Fusion temperature (°C)	> 2800	> 2800	1420	1238	1700	Phase transition
Electron mobility (cm^2/Vs)	1000	600	1400	8500	600	2200
Thermal conductivity ($Wcm^{-1}K^{-1}$)	5	3-5	1.5	0.5	1.5	20
Dielectric constant K	9.7	10	11.8	12.8	9.5	5.5

A particular property of silicon carbide is the number of its polytypes due to the various possibilities of stacking sequence of the tetrahedron layers, which are the basic features of the SiC structure. Structures, which can be developed from the same building units and the same principles of their mutual arrangement, are considered as polytypes. Polytypes can be observed as a special case of polymorphism or allotropy and particularly with laminated structures [Kle90]. From the literature more than 180 polytypes of SiC are already known, differentiated and represented by the Ramsdell notation [Ram74], which uses numbers and letters. The number gives the stacking sequence and the letter the Bravais lattice of the crystal obtained (Table 3.2).

***Table 3.2:** Ramsdel notation, stacking sequences and lattice parameters of some SiC-polytypes [Ram74].*

Ramsdell-Notation	Stacking sequence	Lattice constants
3C	…ABC..	a = 4.36 Å
2H	…AC'…	a = 3.08 Å c = 5.04 Å
4H	…ABAC'…	a = 3.08 Å c = 10.08 Å
6H	…ABCA'C'B'…	a = 3.08 Å c = 15.12 Å
15H	…ABCB'A'BCAC'B'CABA'C'…	a = 3.08 Å c = 37.81 Å

From all polytypes, the basic structures of SiC are 3C-SiC (ß-SiC) with a cubic structure and 2H-SiC with a hexagonal structure (Fig. 3.1).

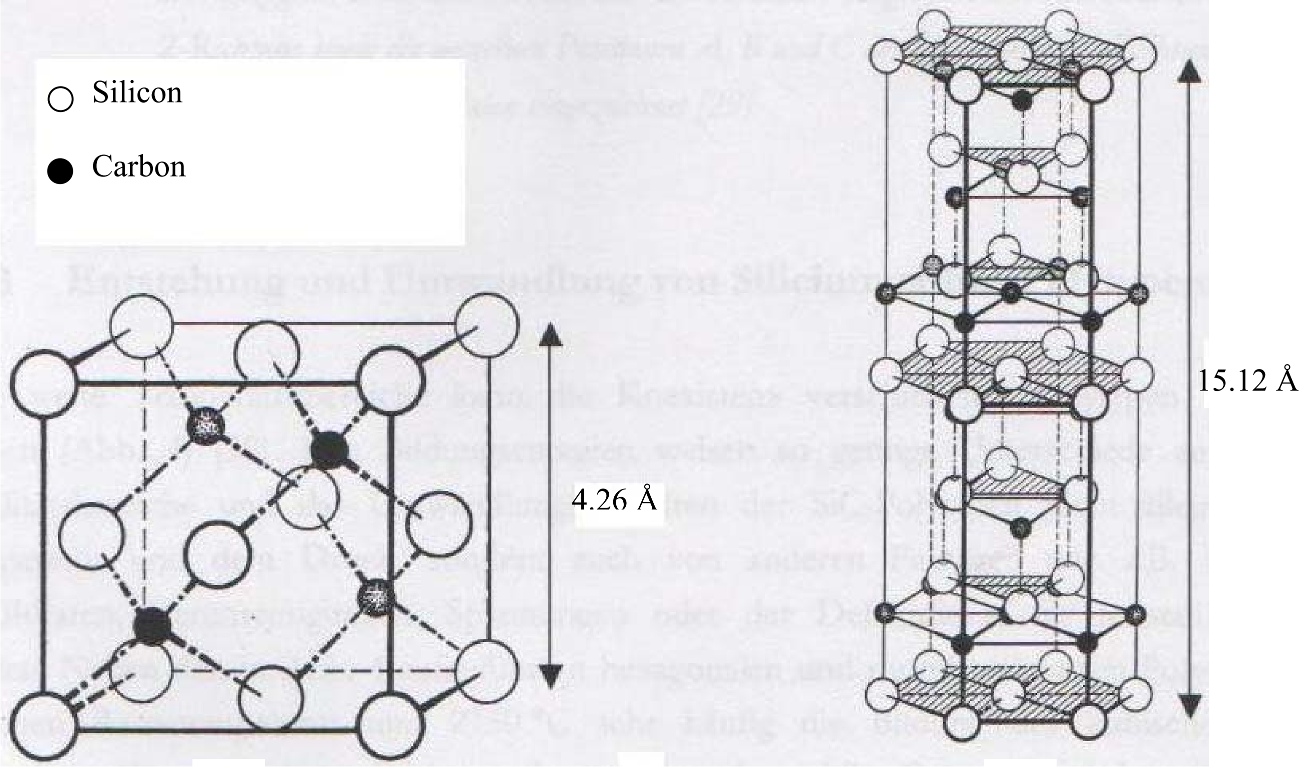

a) b)

***Fig. 3.1:** Lattice structure of a) 3C-SiC (ZnS structure) and b) 6H-SiC [Rau00].*

3.2 Diboride solid solutions

The high melting point, the hardness, the electrical and thermal conductivity and the high oxidation resistance are attractive properties which make diborides of transition metals suitable for various applications in the aeronautic as well as in the automotive industries [Cas77]. Until now several methods have been used to synthesise diboride solid solutions, the goal being generally to improve their density and their toughness. Early investigators have used different methods to prepare metal borides, e.g. electrolysis of fused salt baths containing oxides of metals and boron, and reduction of oxide mixtures with carbon and direct synthesis of elements. The last method consists of sintering or melting the constituents together at temperatures between 1200 °C and 2000 °C, under vacuum in a resistance furnace with graphite tube or high frequency induction furnace [Kies50]. More recently Hisashi and co-workers [His2001] produced solid solutions and composites in the TiB_2-WB_2-CrB_2 system from elemental reactants using the field-activated pressure-assisted synthesis method and employing the Spark Plasma Sintering *(SPS)*. This apparatus is a uniaxial *100 kN* press combined with *15 V, 5000 AC-DC* power supply to simultaneously provide pulsed current and pressure to the sample-die assembly. The obtained sample shows a highest density of 94 % corresponding to a hardness of *22.7 GPa*. Masachika [Mas03] improved this method by introducing the Induction-field-Activated-combustion synthesis (IFACS) to synthesise the binary solid solution TiB_2-WB_2 from elemental reactants in a considerably reduced preparation time.

Diborides-based materials are fairly brittle. Therefore, there is a need to modify their microstructure so as to improve their toughness. Due to the fact that some binary transition metal diboride systems of AlB_2 structure type reveal large mutual solid solubility ranges, tailored precipitation can be used for in-situ reinforcement strategies. The platelet-like precipitations with high aspect ratio should improve the fracture toughness [Fab83]. The first investigations on the solubility of CrB_2, TiB_2, TaB_2, ZrB_2 in WB_2 and MoB_2 were carried out by Post et *al*., achieving a solubility of WB_2 in TiB_2 larger than 50 mol % [Pos54]. Telle investigated the quasi-binary system of TiB_2-WB_2 in the temperature range 1500 °C to 2500 °C [Tel92]. WB_2 exhibits a high solubility in TiB_2 having 8-10 mol % at 1500 °C with a maximum solubility of 63 mol % at the eutectic temperature 2030 °C (Fig. 3.2). The solubility of TiB_2 in W_2B_5 is low (about 1-3 mol %) in the whole temperature range so that an immiscibility gap within the system TiB_2-WB_2 is formed which provided the opportunity to tailor an *in-situ* growth of a platelet-shaped $(W,Ti)B_2$ phase with low TiB_2 content from the supersaturated matrix.

The quasi-binary system TiB_2-CrB_2 is governed by a solubility gap with a critical point at 2000 °C and 20 mol % CrB_2 followed by a continuous solid solubility at higher temperature which is limited by the solidus line at 2200 °C. The solubility of TiB_2 in CrB_2 increases from 45 mol % at 1500 °C to 80 mol % at 2000 °C whereas the CrB_2 content in TiB_2 within the solubility gap is less than 1 mol % below 1800 °C.

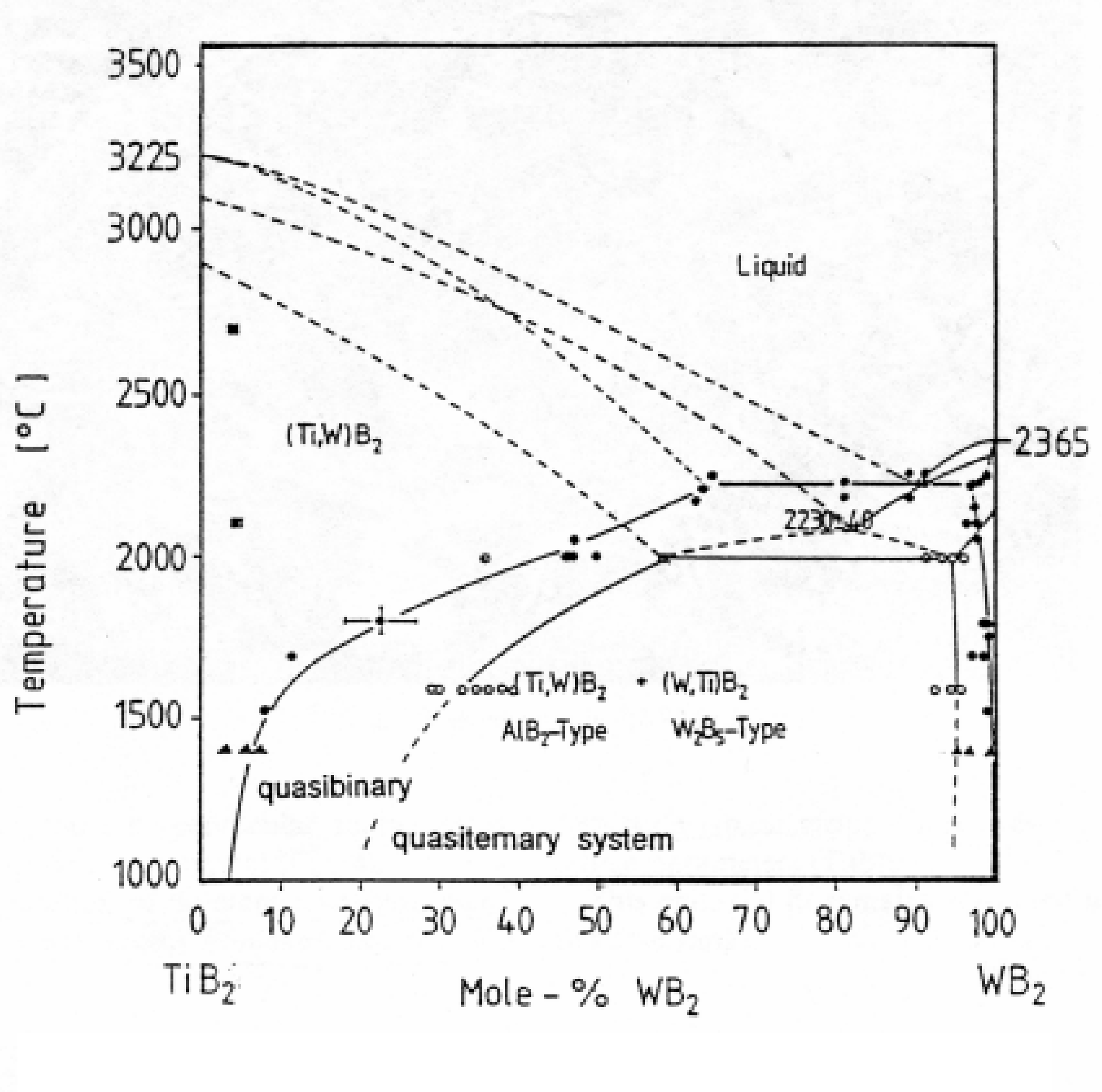

Fig. 3.2: *Quasi-binary phase diagram TiB_2-WB_2 [Tel92]. The circles represent the projection of the diagram with 10 - 20 mol % CrB_2 [Mit98]*

The eutectic system W_2B_5-CrB_2 exhibits an increase in the solubility of W_2B_5 in CrB_2 from 22 mol % at 1500 °C to 37 mol % at the eutectic temperature [Tel92]. Mitra [Mit98] investigated also the influence of CrB_2 on the constitution of the TiB_2-WB_2 phase diagram. The addition of CrB_2 (between 10 mol % and 20 mol %) leads to the extension of the solid solution with TiB_2 structure and to a reduction of the immiscibility gap between W_2B_5 and TiB_2. As a result, an increase of the solubility of W_2B_5 in TiB_2 is achieved and a high amount of W_2B_5 precipitates can be obtained. Furthermore, a phase with ß-WB structure, depending on the concentration of Ti, W and Cr, is also obtained.

The structures of TiB_2, WB_2 and CrB_2 can be described as alternate boron and transition metal layers. TiB_2 and CrB_2 crystallise in the hexagonal structure of AlB_2-type with space group *p6/mmm*, consisting of alternate metal and boron layers so that the stacking sequence can be summarised as AHAHAH. A represents the layers of the metals and H those of the boron atoms [Pos54]. The W_2B_5 lattice possesses another metal position and one more puckered boron layer K' leading to the stacking sequence AHAK'BHBK'A (Fig. 3.3), [Lun68]. ß-WB crystallises in an orthorhombic structure with the space group *Cmcm*.

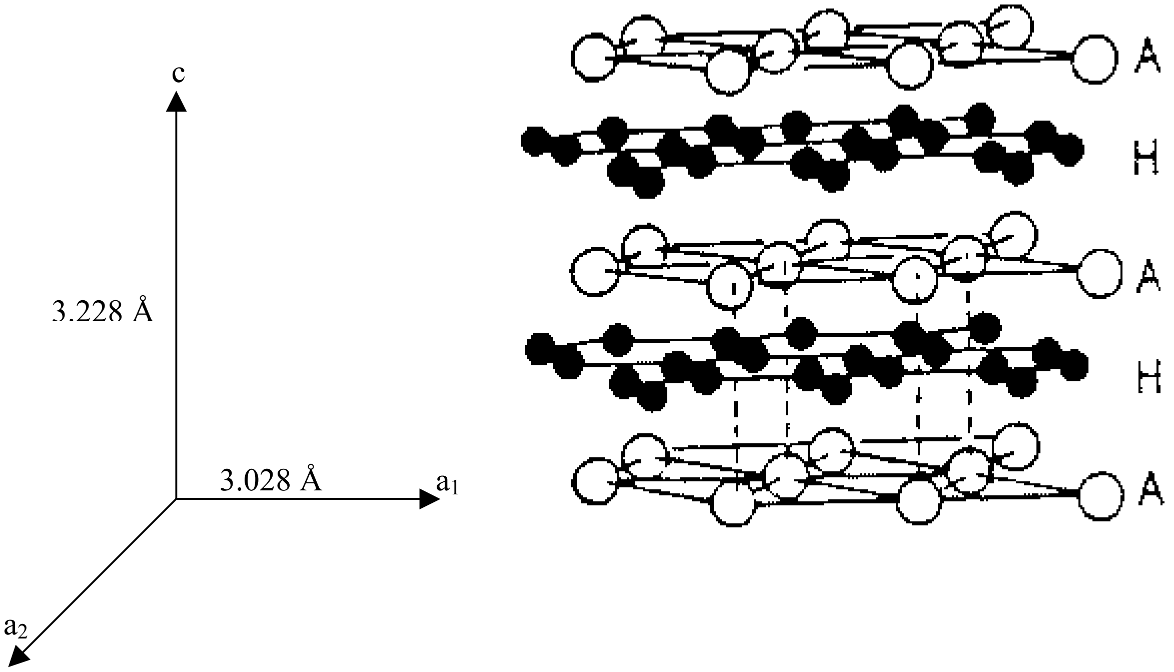

Fig. 3.3a: *AlB_2 structure type of TiB_2 and CrB_2 [Pos54]* .

In the quasi-ternary system $(Ti,W,Cr)B_2$ several phases can precipitate within the supersaturated TiB_2 matrix. Up to now, phases crystallising in W_2B_5 and ß-WB structures have been reported [Mit97]. The ß-WB structure grows epitaxially and parallel to the $\{1\bar{1}00\}$ prism planes of the TiB_2 structure.

Using the energy filtering TEM [Rei95] by taking electron spectroscopic images produced by inelastically scattered electrons, qualitative information on the chemical composition and the distribution of the elements Ti, Cr, W and B can be obtained [Hof96]. One of the results reported is the good fit of the lattices at the interface, i.e. $c(TiB_2)$ is parallel to a(WB) and $a(TiB_2)$ is parallel to c(WB). Moreover it is proved that ß-WB is the high temperature form of monoboride, which converts reversibly into α-WB below 2100 °C and can be stabilised by the incorporation of up to 40 at. % Ti [Kuz69] or 20 at. % Cr [Tel68]. Using the HRTEM observations, a spinodal-like decomposition is also detected [Sch01].

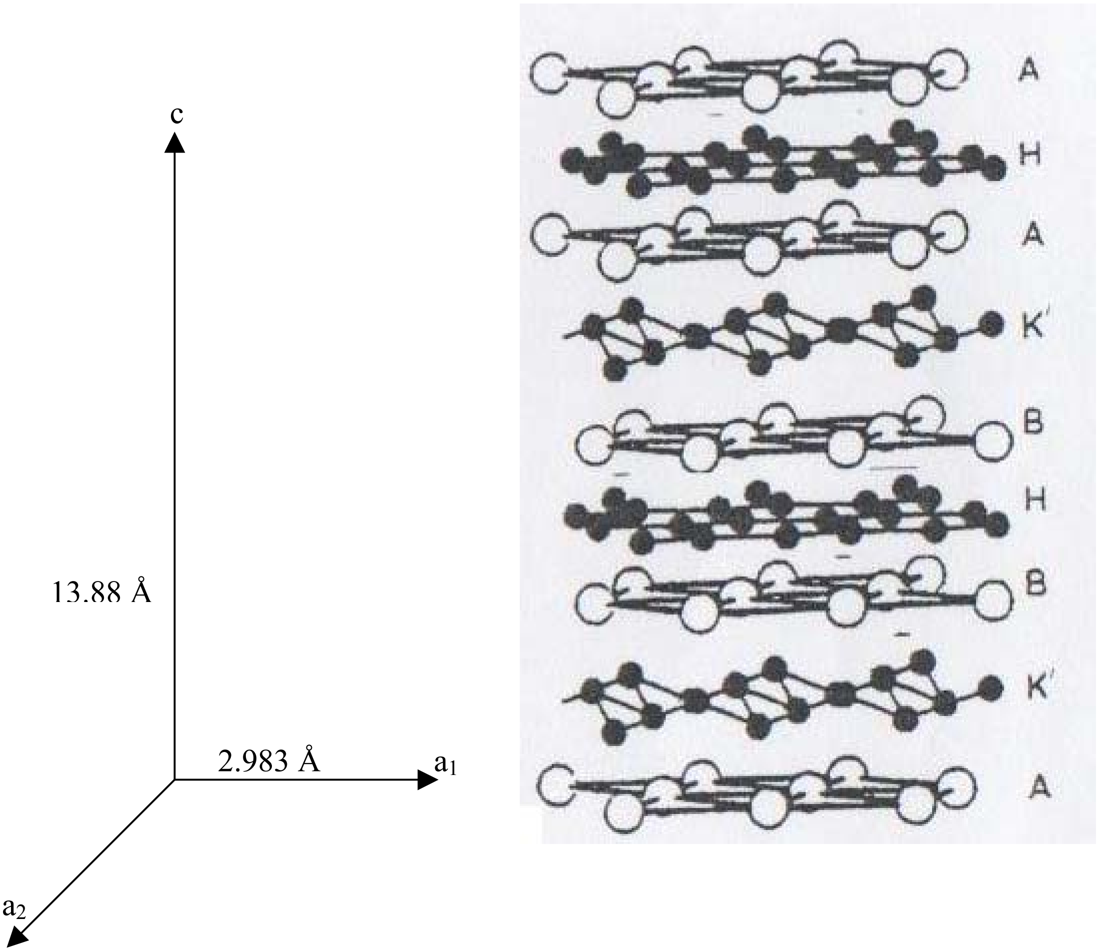

Fig. 3.3b: *W_2B_5 structure type [Hig86].*

4 Theoretical background

4.1 Classification of phase transformation

The word “transformation” used in the general sense means an extensive re-arrangement of the atomic structure. The driving force for any transformation is the difference in Gibbs free energy of the initial and final state. This energy has to be minimised for each stable phase formed. In general, an intermediate stage of the assembly can be divided into microscopically distinct regions of which some are transformed and others are not. This means that most transformations in materials science are heterogeneous.

We will focus our attention on the “nucleation and growth“ transformation since it is the most common solid-state transformation. This group can be subdivided into two categories:

- long range transport which corresponds to the diffusion-controlled transformations
- interface-controlled transformations

Throughout this thesis, we will try to highlight the kinetics of these two types of transformations within the framework of the various studied systems.

4.2 General kinetic theory

As mentioned above, the description of the solid-state transformation kinetics remains a field of great interest, where the contributions from Johnson and Mehl and later from Avrami and Kolmogorov known as the Johnson-Mehl-Avrami Kolmogorov (JMAK) theory are and have been influential.

Experimentally, two different approaches can be used. While the JMAK model is suitable for isothermal transformation kinetics, i.e. the investigations are carried out at constant temperature, the dynamic or non isothermal state transformation at constant heating rates can be easily treated using the Kissinger or Ozawa methods [Kis57], [Oza71].

4.2.1 Johnson-Mehl-Avrami-Kolmogorov model (JMAK)

The derivation of the JMAK kinetics is based on the combination of three processes: nucleation, growth and impingement of randomly distributed nuclei. The impingement is considered as hard impingement of homogeneously dispersed particles [Avr39], [Joh39].

This model is based on the concept of extended volume. The extended volume corresponds to the volume occupied by the nucleated particles, which grow infinitely and without impingement. Considering the number of nuclei $N(T,\tau)$ formed in a unit volume at time τ in the absence of other growing particles and supposing that each particle grows in an infinitely large parent phase, the volume of nuclei that grow from τ until time t is given by:

$$V^e = \int_0^t V_0 I(T,\tau) V(T,\tau,t) d\tau \tag{4.1}$$

where I(T,τ) is the nucleation rate and *V(T,τ,t)* is, at time t, the d-dimensional volume ($1 \leq d \leq 3$) of a particle which is born at time τ. V^e is the extended volume.

This volume is a function of a d-dimensional factor f_d and the radius of the born nuclei.

In reality, the nuclei are not growing into an infinitely parent phase and V^e does not account for the overlap of particles, i.e. hard impingement and also their possibly surrounding diffusion field, i.e. soft impingement. Consequently, a relationship between the extended volume and the actual transformed volume V^t is required.

The particles are randomly distributed throughout the volume. This assumption is justified in the homogeneous as well as in the heterogeneous nucleation. In the second case, the formation of nuclei takes place at randomly dispersed nucleation sites.

Supposing that the actual volume at time *t* is V^t, with an infinitesimal increase of the time *dt*, the extended and transformed volume will increase by dV^e and dV^t. From the change in the extended volume, only a part will contribute to the change of the actual transformed volume, namely a part as large as the untransformed volume fraction. Hence,

$$dV^t = \left(1 - \frac{V^t}{V_0}\right) dV^e \tag{4.2}$$

Dividing equation (4.2) by V_0 a similar equation for the transformed volume fraction can be obtained:

$$\frac{dX(T,t))}{1 - X(T,t)} = dX^e(T,t) \tag{4.3}$$

The integration leads to

$$X(T,t) = 1 - \exp\left[- X^e(T,t)\right] \tag{4.4}$$

With

$$X^e(T,t) = \int_0^t I(T,t) V({}'T,\tau,t) d\tau \tag{4.5}$$

Generally, in order to derive the explicit analytical formulation of the transformed volume fraction, the extended volume is calculated using the appropriate nucleation and growth models according to equation (4.5) and substituted into equation (4.4).

It is important to mention the fact that the correction in equation (4.2) and (4.3) depends on the impingement model. For extreme cases, where no correction is required because there is no impingement, we have $X(T,t) = X^e(T,t)$ for $X^e(T,t) \leq 1$, and $X(T,t) = 1$ for $X^e(T,t) > 1$. For any impingement model, it is impossible to have $X(T,t) > X^e(T,t)$ or $X(T,t) > 1$. t is the annealing time and varies from zero to the time corresponding to the full crystallisation.

Depending on the nucleation and growth models other corrections have been proposed. Lee and Kim [Lee90] proposed an alternative approach to the impingement problem by introducing an adjustable fitting parameter *c* termed "impingement parameter". From the equation $\frac{dX(T,t)}{dX^e(T,t)} = (1 - X(T,t))^{1+c}$, they showed that *c = 0* corresponded to the JMAK kinetics whilst for *c = 1* the equation first derived by Austin and Rickett to investigate the kinetics of decomposition of Austenite [Aus38] was obtained.

4.2.2 Nucleation

During a phase transformation, interfaces developed between the old and the new phases and possible misfit strain are introduced into the system. Whereas the production of the new phase releases Gibbs free energy, the creation of the interfaces and the introduction of strain raise the Gibbs energy. In the classical theory [Chr75] a particle born in the new phase must have a critical size, corresponding to a minimum free energy, in order to grow, if not it increases the energy and is forced to shrink. The formation of particles with the adequate critical size is called nucleation.

Let us consider a spherical particle, with radius *R,* nucleated from a parent phase A (Fig. 4.2). An infinitesimal variation of the radius from R to $R + dR$ leads to a variation *dG* of the total Gibbs free energy due to the nucleation

$$d\Delta G = -4\pi R^2 \Delta G_V dR + 8\pi R \sigma dR \tag{4.6}$$

Where ΔG_V is the free Gibbs energy difference due to the volume and σ is the interfacial energy per unit area interface. The use of the minimum energy ($\frac{d\Delta G}{dR} = 0$) leads to the critical radius of the particle:

$$R_c = \frac{2\sigma}{\Delta G_V} \tag{4.7}$$

By integrating equation (4.6) and substituting *R* by R_c, the gibbs free energy of nucleation ΔG^* can be evaluated as follows:

$$\Delta G^* = \frac{16\pi\sigma_3}{3\Delta G_V^2} \tag{4.8}$$

ΔG^* can be approximated as $\frac{A}{\Delta T^2}$ [Por81] (where A is a constant depending on the interfacial energy per unit area and on the entropy ΔS of formation) since the Gibbs free energy due to the volume is proportional to the undercooling or the overheating ΔT, with respect to the temperature at which the two phases are in equilibrium.

According to equation (4.7), it clearly appears that the critical radius can be directly defined by the undercooling or the overheating. If ΔT is small, the critical radius is bigger and the density of the nuclei is smaller than in the case of a higher ΔT.

Furthermore, if the undercooling or the overheating is very large, ΔG^* can be considered to be very small. Therefore, the nucleation rate per unit volume I(T), i.e. the rate of formation of particles with critical radius, is only determined by the atomic mobility for transport through the interface, which can be given by an Arrhenius term:

$$I(T) = I_0 \exp\left(-\frac{\Delta H_N}{k_b T}\right) \tag{4.9}$$

where I_0 is a pre-exponential factor ($I_0 \approx \nu \exp\left(\frac{\Delta S}{k_b}\right)$), ΔH_N is the temperature dependent activation enthalpy for nucleation ΔS is the entropy, ν is the effective attempt frequency and k_b is the Boltzmann constant.

The nucleation model considered can be continuous (constant, decreasing or increasing), i.e. the nucleation rate is temperature dependent according to an Arrhenius equation, or site saturation, where all nuclei are present before the growth starts. A mixture of both can also be considered. (Fig. 4.1).

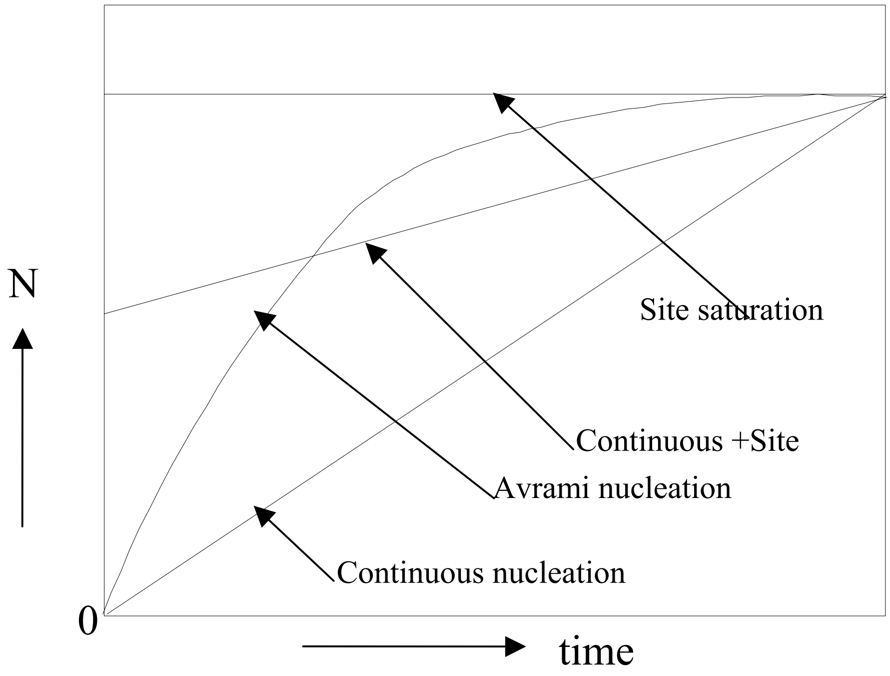

Fig. 4.1: *Schematic diagram of the number of nuclei (N) as a function of time at constant temperature for different nucleation models [Kem01].*

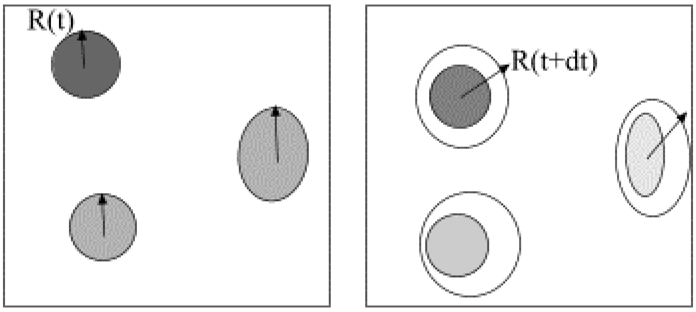

Fig. 4.2: *Evolution of the radius of the nuclei after an infinitesimal increase of time.*

4.2.3 Growth and JMAK exponent

The growth processes can be volume diffusion controlled [Wer50] where long range compositional changes take place during the phase transformation, or interface controlled in the absence of compositional changes, e.g. in cases of allotropic phase transformations.

In general, the radius *R(T,τ,t)* is obtained by the integration of the growth rate *U(T,t).* For instance, for a constant nucleation rate and any radius dependent particle growth, *U(T, r(τ,t))*, the radius has the form

$$R(T,\tau,t)=\left[U(T)(t-\tau)\right]^{\frac{1}{m}} \tag{4.10}$$

with

$$U(T)=U_0\exp\left(-\frac{\Delta H_g}{k_bT}\right) \tag{4.11}$$

where m is a growth mode factor, e.g. m = 1 for interface controlled growth and m = 2 for diffusion controlled growth. *U(T)* is the temperature dependent growth rate and ΔH_g is the activation enthalpy for the growth process

The extended volume fraction can then be explicitly calculated from equation (4.5) and given by

$$X^e(T,t)=\int_0^t I(T,t)f_dU^{\frac{d}{m}}(T)(t-\tau)^{\frac{d}{m}}d\tau \tag{4.12}$$

where d (Table 4.2) is the dimensionality of the growth and f_d a geometrical factor (2π for two dimensional and 4π/3 for three-dimensional growth).

For special cases, where the nucleation and growth rates are constant with respect to time, the transformed volume fraction can be given by

$$X(T,t)=1-\exp\left[-(k(T)t)^n\right] \tag{4.13}$$

with

$$k(T)=\sqrt[n]{\frac{f_dI_0(T)U^{\frac{d}{m}}(T)}{\frac{d}{m}+1}} \tag{4.14}$$

and

$$n=\frac{d}{m}+1 \tag{4.15}$$

k(T) is a temperature dependent rate constant and *n* is the JMAK exponent.

The above treatment leads to explicit expressions of the JMAK exponent n, the free enthalpies ΔH and the constant rates k(T) (Table 4.1).

According to the JMAK theory, the dimensionality and the growth morphology of the particles can be determined through the JMAK exponent, which is defined as the slope of the straight line $\ln(-\ln(1-X(T,t)))$ versus $\ln(t)$ according to equation (4.13). For small variations of the crystallised volume fraction the so-called local JMAK exponent can be defined and can be given analytically as,

$$n(T,t) = \frac{d\left[\ln\left(-\left(\ln\left(1 - X(T,t)\right)\right)\right)\right]}{d\left[\ln(t)\right]}, \tag{4.16}$$

or directly from the extended crystallised volume fraction:

$$n(T,t) = \frac{d\left[\ln\left(X^{e}(T,t)\right)\right]}{d\left[\ln(t)\right]} \tag{4.17}$$

If the time dependence is the same during the whole transformation process, that is to say, if there is no change of the microstructure during the transformation, the JMAK exponent should remain constant throughout the whole process. However, in the case of increasing or decreasing nucleation rate, the JMAK exponent is not constant but continuously increases or decreases, and gives at the end of the transformation an extreme value corresponding to site saturation or constant nucleation (Table 4.2).

Table 4.1: *Expression of the JMAK exponent, the rate constants and the activation enthalpies for different types of nucleation.*

Isothermal transformations		
	Continuous nucleation	**Site saturation**
JMAK exponent (n)	$\frac{d}{m} + 1$	$\frac{d}{m}$
Activation enthalpy (ΔH)	$\frac{(n-1)\Delta H_g + \Delta H_N}{n}$	ΔHg
Rate constant (k)	$\sqrt[n]{\frac{f_d I_0(T) U^{n-1}(T)}{n}}$	$\sqrt[n]{f_d I_0 U^{n}(T)}$

Table 4.2: *Equivalent JMAK exponents for different growth geometries.*

Dimensionality	Nucleation model	Interface controlled transformation (m = 1)	Diffusion controlled transformation (m = 2)
Three-dimensional d = 3	Site saturation	3	1.5
	Conti. nucleation	4	2.5
	Decreasing nucleation	3-4	1.5-2.5
Two-dimensional d = 2	Site saturation	2	1
	Conti. nucleation	3	2
	Decreasing nucleation	2-3	1-2
One-dimensional d = 1	Site saturation	1	0.5
	Conti. nucleation	2	1.5
	Decreasing nucleation	1-2	0.5-1.5

4.3 Modified JMAK models

The domain of validity of the JMAK model is still a point of interest in the field of transformation kinetics since the JMAK exponent cannot always be interpreted directly on the basis of Table 4.2. In general the JMAK exponent appears to range between the values expected for site saturation and continuous nucleation. In this case, it may be deduced that, either the nucleation is of intermediate type or a combination of two different growth (interface and diffusion) models or that there are some other parameters, such as critical radius of nucleation at grain boundaries, which were not taken into account while deriving the JMAK equation. Since the rate constant *k(T)* is a stable parameter and does not change from a model to another, the most critical point of the validity of the JMAK theory is the interpretation of the JMAK exponent. In fact, many anomalous JMAK exponents and non-linear Avrami plots have been observed in the crystallisation process of metallic glasses or solid solutions. Greer found no explanations to abnormal values of the JMAK exponent varying from 0.7 to 4.87 for the crystallisation of Metglas 2605 $Fe_{80}B_{20}$ [Gre82]. Likewise, Nicolaus studied the crystallisation of amorphous $Co_{33}Zr_{67}$ and found a value of n =2.44 that is lower than the value expected (n = 3) for the polymorphic crystallisation process [Nic92]. Ghosh [Gho91] attributed the rise of the local JMAK exponent at high values of transformed volume fraction in the crystallisation of amorphous $Ni_{24}Zr_{76}$ alloys ribbons, to the impingement effect at the final stage of the process. Holzer [Hol91] claimed that the anomalous JMAK exponent in the crystallisation of Al-Cu-V alloys is a consequence of an inhomogeneous distribution of pre-exiting nuclei. It appears clearly that systems that follow exactly the JMAK model are rare. Therefore, following these observations and considering that the JMAK exponent is directly correlated to the growth dimensionality, it can be deduced that the microstructure (for example the effect of the critical radius) [Her97], the nucleation modus (effect of the grain boundaries) and the variation of the chemical composition (soft impingement) on the initial growth rates may play an important role in the interpretation of the values of the JMAK exponent. Thus, it is clear that the JMAK model holds for some cases, especially for polymorphic phase transformation, but has to be modified or newly derived to describe specific cases. Several approaches have already been proposed. Extension of the JMAK model to perform the calculation of time-dependent grain-size populations providing more detail on the microstructure was presented [Cre96], [Cre97]. Considering position-dependent nucleation sites, a modified JMAK model based on non-randomly (non-Poisson distribution) distributed particles [Ueb96] [Pin02] was investigated by the means of Monte Carlo simulations. Other effects such as surface nucleation [Kel85], anisotropic particles [Wei96] and finite size [Lev97] on the JMAK theory have also been discussed.

4.3.1 Soft impingement

In a simple way, one can consider that nuclei are formed by fluctuations in the disordered phase and, in the initial stage of the growth, the species rejected from the crystalline phase will pile up ahead of the interface until metastable local equilibrium is reached. Therefore, the growth rate can be taken as

$$\frac{dR}{dt}=\frac{D(T)}{R}\frac{C_s-C_m}{C_s-C_p} \tag{4.18}$$

where C_p, C_s and C_m are the concentrations of the slowest species diffusing inside the precipitate, at the surface and far from the precipitate, respectively. The above equation shows that the growth rate of an isolated particle depends on the concentration value far from the particle. If the effect of the rest of the growing particle on this value is neglected, then $C = C_0$ (concentration of the diffusing element at $t = 0$). This approximation is usually known as diffusion controlled growth with hard impingement. However, the validity of this approximation depends on the difference $C_s - C_m$. If the difference is very large, the excess or the defect of the species in the untransformed phase will affect the growth very little. But the presence of the solute in the matrix due to the growth of neighbouring particles will reduce this difference and at the end of the transformation, one can have $C_s - Cm \rightarrow 0$. Thus, as a second approximation, we can consider the variation of C during the transformation as soft-impingement. Investigations on a FINEMET material of composition $Fe_{73.5}Si_{17.5}CuNb_3B_5$ lead to the conclusion that the soft impingement growth mechanism is responsible for the anomalous behaviour of the Avrami exponent and that decreasing nucleation rate plays only a second role [Pra98]. The modelling of the soft impingement diffusion controlled precipitation is presented in the appendix (8.1).

4.3.3 The effect of the grain boundaries

Grain boundaries can play a significant role in the crystallisation or precipitation kinetics for several reasons. First of all, the local free energy of boundary regions is higher than in the bulk of the grain implying that the driving force for nucleation of crystalline nuclei is much higher than within the grain body. Secondly, boundaries have structure components such as non-coincident sites where the transition between atomic configurations occurs more easily than anywhere else in the bulk. This results in a fast atomic diffusion on boundaries and therefore reduces the kinetic barriers for nucleation and growth of the new phase on boundary regions.

Talking about grain boundary or other free surfaces and corners implies necessarily the notion of heterogeneity, which is an inherent property of crystallisation. Heterogeneous crystallisation is understood as nucleation distributed non-uniformly in the bulk. Grain boundaries are the most favourable regions for nucleation of a new phase; therefore one can assume that nucleation occurs preferentially at grain boundaries (Fig. 4.3).

When the distances between nuclei in the boundary region have become comparable with their sizes, the total flux to the nuclei decreases because of the competitive growth. Consequently, the crystallisation becomes much slower in the last stage. The possibility of nucleation and growth of crystalline phase in the bulk after overlapping of diffusion zones of growing nuclei in the boundaries thus appears (Fig. 4.3).

The details on the modelling of the heterogeneous nucleation followed by the three-dimensional growth of particles proposed by Bakai can be found in the appendix (8.2).

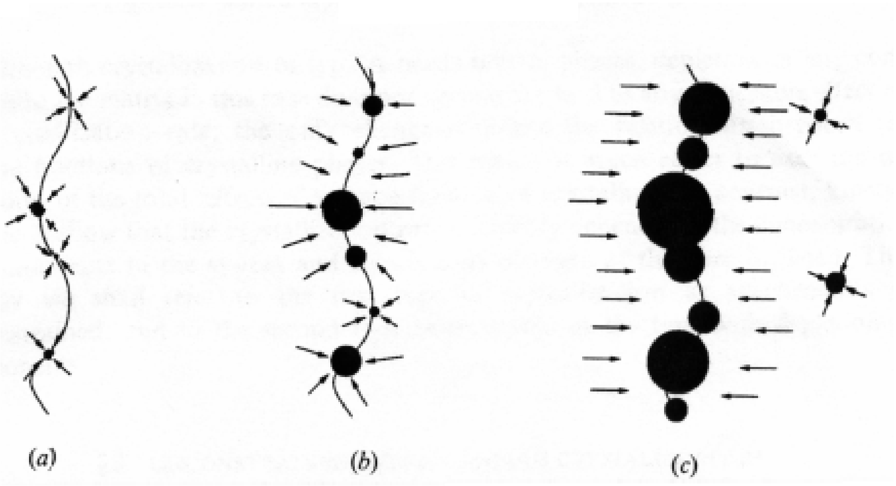

Fig. 4.3: *Different stages of the growth of crystalline nuclei at grain boundaries: (a) independent nuclei growth at boundaries; (b) crossover to overlapping of regions of influence; (c) growth in the bulk [Bak02].*

5 Experimental procedure

5.1 Sample preparation

5.1.1 Amorphous silicon carbide thin films

Silicon carbide thin films were prepared by co-sputtering of carbon and silicon using a 3'' US GUN low profile planar magnetron source (AP&T, Nürtingen, Germany) (Fig. 5.1). It was mounted on a standard DN 150 CF double cross chamber equipped with pre-sputter shutter and sample positioner allowing the variation of distances (100-200 *mm*) between magnetron and substrate. Carbon strips (99,99 %, Goodfellow, Bad Nauheim, Germany) of 5 x 25 mm^2 were radially fixed at equal distances on a 3'' silicon base target (99,99 %, Norwegian Talc, Bad Soden, Germany). The process was carried out under argon atmosphere. Using the above method, SiC films of 1 μm thickness were deposited on glassy carbon and single crystalline silicon substrates, which were polished beforehand and cleaned with ethanol in an ultrasonic bath. The chemical composition of the thin films is determined to be stoichiometric SiC by non–Rutherford Backscattering Spectroscopy (n-RBS) using elastic 3.5 MeV $^4He^+$ particles at a scattering angle of 171 ° [Lut98]. The characterisation and the preparation of the amorphous SiC films have been made in cooperation with the "Institut für Kernphysik" of the "J. W. Goethe-Universität Frankfurt" and the "Institut für Instrumentelle Analytik" of the "Forschungszentrum Karlsruhe".

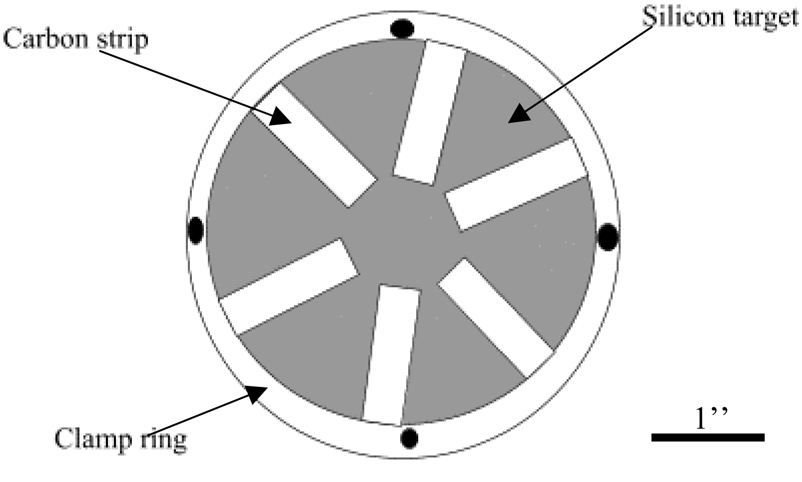

Fig. 5.1: *A 3'' silicon target with radially mounted carbon strips.*

5.1.2 Transition metal diboride based materials

The samples investigated in this work were produced by a high-pressure reaction sintering process at the “Institut für Gesteinshüttenkunde” of the University of Aachen (Germany). As raw materials, TiB_2, WB_2 and CrB_2 powders (H. C. Starck Goslar, Germany) were used. The impurities were less than 1 wt%. The weighed materials were dry-mixed in a mixer and subsequently attrition milled with WC/Co hard metal balls in a steel vessel containing isopropanol in order to increase the sinter activity. The dried powders were then uniaxially hot pressed at *1800 °C* for *30* minutes under 1 atm argon pressure with *60 GPa*. The hot-pressed specimens were annealed at *2000 °C* for 8 hours to homogenize the solid solution of (Ti, W, Cr) B_2. The samples showed a relative density of 90 %.

In order to investigate the effect of the preparation process on precipitation behaviour, the samples were classified into two series containing milled (A) and not milled (B) samples. For each group, the samples are separated into A523, B352 etc… to represent the titanium (Ti), tungsten (W) and the chromium (Cr) concentration in at. % contained in the samples (Table 5.1).

Table 5.1: *Codification of the investigated samples.*

Group A (milled)		Group B (not milled)	
A352	$(Ti_{0.3}W_{0.5}Cr_{0.2})B_2$	B352	$(Ti_{0.3}W_{0.5}Cr_{0.2})B_2$
		B451	$(Ti_{0.4}W_{0.5}Cr_{0.1})B_2$
		B550	$(Ti_{0.5}W_{0.5})B_2$

5.2 Isothermal treatment

For the diborides, small platelets (about 5x5x2 mm^3) were cut from the interior of the hot pressed samples, polished with diamond paste and cleaned with ethanol. To observe phase separation, the platelets were annealed in the temperature range between 1400 °C and 1700 °C in argon atmosphere (980 mbar) for periods between 1 to 40 h. To avoid formation of oxide layers and possible contamination during annealing, the samples were placed on top of each other with the polished surfaces, mounted in a crucible and surrounded by fine grain powder of TiB_2. To ensure isothermal conditions, very high heating and cooling rates were realised by a special mechanical transfer unit, with which samples could be placed in the hot zone of the furnace under argon atmosphere within 5 minutes. The furnace used an Al_2O_3 tube with a steel head cooled by a cold water circuit (Fig. 5.2).

For SiC films, the thermal treatment procedure was the same as described above except that the annealed films were surrounded with fine SiC powder to avoid oxidation at temperatures between 1200°C and 1600°C for glassy carbon substrates and between 1200 °C and 1400 °C because of the lower temperature of the silicon substrate.

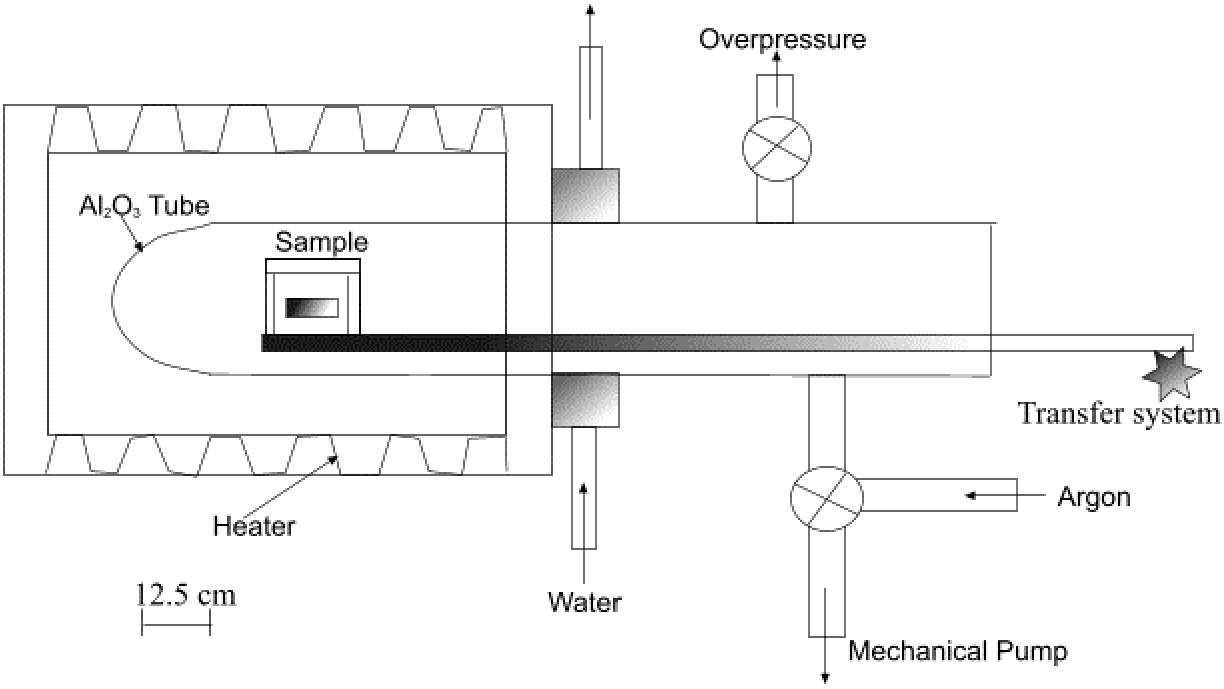

Fig. 5.2: *Schematic representation of the furnace system used for the heat treatments.*

5.3 Sample characterisation

5.3.1 X-Ray diffraction

The most important purpose of the X-ray diffraction was the detection and determination of the phases appearing after the precipitation and crystallisation processes. All X-ray diffraction investigations were carried out with a diffractometer Kristalloflex D5000 from Siemens, operating with Cobalt radiation (λ = 1.7902 Å) and using a scintillation detector coupled with an iron filter. The experiments were made under ambient atmosphere with the conventional $\theta / 2\theta$ modus with Bragg angles between 25° and 90°.

The amount of the each phase was determined under the assumption that the intensity of each peak was proportional to the volume of the precipitated phase. The characteristic XRD peaks for the precipitated phase were fitted using a Lorentzian function from which the area and the full width at half maximum were obtained. This procedure was repeated until the precipitation remained constant. The typical precipitation or crystallisation kinetics were obtained from the precipitated fraction as function of time. Furthermore, using the Scherrer equation the average size of the crystallites or the precipitates was determined. The X-ray diffraction diagram was also completely refined using a special refinement program (POWDER Cell) based on the least squares method. The aim of this program is to translate, rotate, change, add or clip atoms or molecules of the structure, in order to manipulate the resulting X-ray diffraction [Kra96]. Resulting from the comparison with experimental data, lattice parameters within the structure and the amount of the precipitated phase can be achieved.

5.3.2 Scanning electron microscopy (SEM)

All the SEM investigations were made on diboride solid solutions only. The scanning electron microscopy was used to determine the site of precipitates and to follow the growth of these precipitates. The investigations were done on a CamScan 44 with a tungsten cathode operating with an accelerating voltage ranging between one and thirty kilovolts. The connection of the sample edges and sample-holders with a small carbon fibre increased the conductivity of the sample and improves the quality of the observations and the SEM images.

A quantitative evaluation of the chemical composition of the matrix and the precipitated phase was carried out using the energy dispersive x-ray diffraction (EDX) apparatus mounted on the SEM. An acceleration voltage of about 20 kV was applied for an electron penetration depth of less than 1μm. To follow the microstructure, special zones of the samples were chosen and observed after each thermal treatment. Line scan EDX measurement was made to detect the concentrations changes directly in the vicinity of a precipitate. The apparatus used was a Cameca SX-100.

5.3.3 Transmission electron microscopy (TEM)

All the TEM investigations were made on SiC films only. The use of the transmission electron microscopy (TEM) enables the detection of the amorphous and crystallised phases, the determination of the morphology and size of the crystallites, the determination of the structure of the crystallised phase, as well as the chemical composition of the amorphous and crystallised phases using a mounted EDS apparatus.

TEM is an imaging technique in which a beam of high energy electrons is focused onto a thin specimen (less than 200 nm) causing an enlarged version to appear on a fluorescent screen. The bundling and focussing of the electron beam are done by symmetric and inhomogeneous magnet fields. The beam selection is controlled by metal screens.

The central spot or the scattered electrons are used to form images in TEM. A dark field image can then be formed using electrons scattered from the specimen and a bright field image can be obtained directly from the transmitted electrons. TEM can also be used in the diffraction modus where selected area electron diffraction (SAD) gives information on the local structure of the specimen.

A big challenge with TEM measurements is the sample preparation. The first important step in the preparation of TEM samples consists of cutting the sample into slices of about 2mm bright using a diamond saw in order to avoid the loss of material. The obtained slices are glued together with sides supporting films facing each other (Fig. 5.3). After hardening of this assembly, the obtained sandwich is embedded into cylindrical holders made of brass in order to increase the stability of the sample and placed in a drying oven at about 60 °C to accelerate the hardening. The material of the holder determines the abrasion rate during the sawing, the polishing, dimpling and also during the final ion beam thinning. The glues used are special epoxy glues with low viscosity such *as M-Bond 610* or *Araldite 2020* that yield glue layers of less than 1 µm.

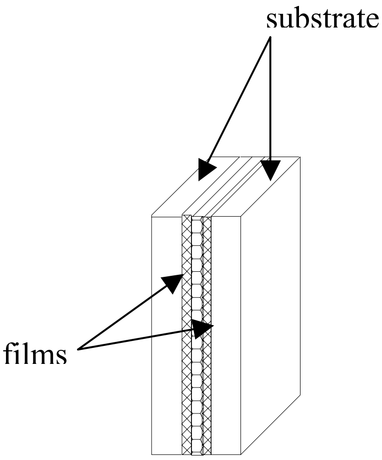

Fig. 5.3: *Films on substrates sandwiched together face to face.*

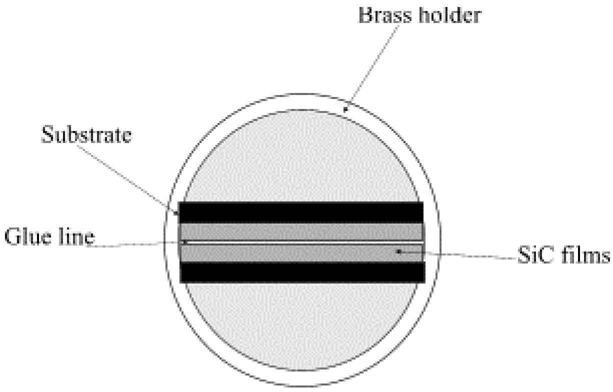

Fig. 5.4: *Cross section after gluing the films into the cylindrical brass holder.*

The next step of the preparation is the sectioning of the holder containing the sample into small discs (Fig. 5.4) of about 0.5 mm thickness, which are subsequently reduced to 200 μm by a mechanical polishing using diamond-impregnated paper. At this stage the disc can be bevelled, (Fig. 5.5) polished on one side and dimpled on the other side (Fig. 5.6) or dimpled on both side. The dimpling of our samples was made with the dimple grinder model 656 from *Gatan*. Diamond suspension of 6 μm was used at the beginning of the dimpling and the suspension of 1μm at the end in order to obtained fine polished zones.

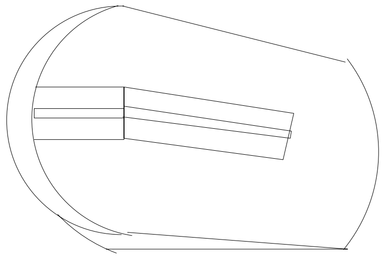

Fig. 5.5: *Bevel polishing of the sandwich.*

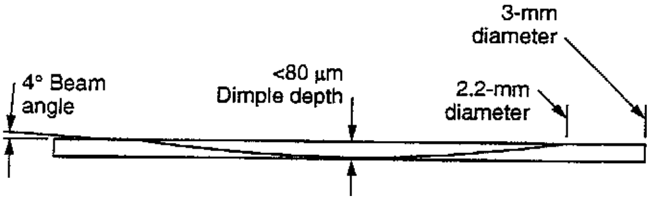

Fig. 5.6: *One side dimpling of the sandwich.*

In order to obtain samples transparent to electrons the dimpled discs were afterwards thinned by ion beam milling with the Precision Ion Polishing System (PIPS) from *Gatan* operating with variable angles (1 °to 10 °) and with voltages ranging between 1 and 10 kV. When placing the thinned discs into the PIPS device, the glue line ought to be perpendicular to the ion beam direction to prevent rapid removing of the glue, which can lead to a direct exposure of the film. To avoid this effect the PIPS device used a special sector speed control that switched off the ion beam as soon as it was parallel to the glue line. After this procedure, the transparent samples were then observed using a *HITACHI 600* TEM operating at 100 kV. Further investigations were also made on a high resolution JEOL 2010 TEM equipped with a Field Emission Gun (FEG) and working at 200 kV. More details on the preparation method can be found in [Str93], [Ame97].

6 Results and discussion

6.1 Crystallisation kinetics of amorphous SiC films

6.1.1 Films deposited on crystalline silicon substrates

The diffractogram of the as-deposited thin films does not exhibit any X-ray peak corresponding to the crystalline SiC structure, confirming the amorphous state of the material (Fig. 6.1). A TEM micrograph (Fig. 6.2) shows a completely amorphous film on silicon substrate after the deposition. The corresponding SAD (selected area diffraction) pattern exhibits diffuse haloes that characterised once more the amorphous state of the deposited film. The sharp spots, which overlap, correspond to the crystalline silicon substrate. Additional information on the chemical composition of SiC films is obtained by EDS investigations. The presence of small amounts of oxygen and argon coming from the preparation process and from the ion beam thinning could be detected. This analysis confirmed that the SiC film was composed of Si and C in stoichiometric proportions (Fig. 6.3). A thickness of the films of about 500 nm was measured.

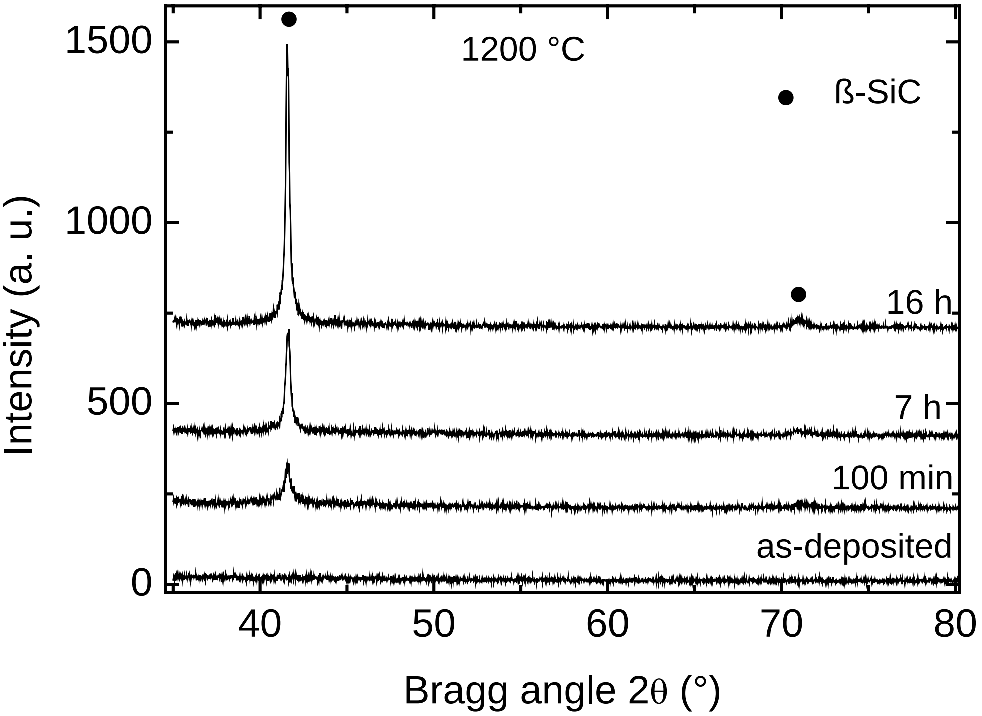

Fig. 6.1: XRD patterns of as-deposited and annealed SiC films sputtered on a silicon substrate. An increase of the (111) peak of the ß-SiC with increasing annealing time is observed.

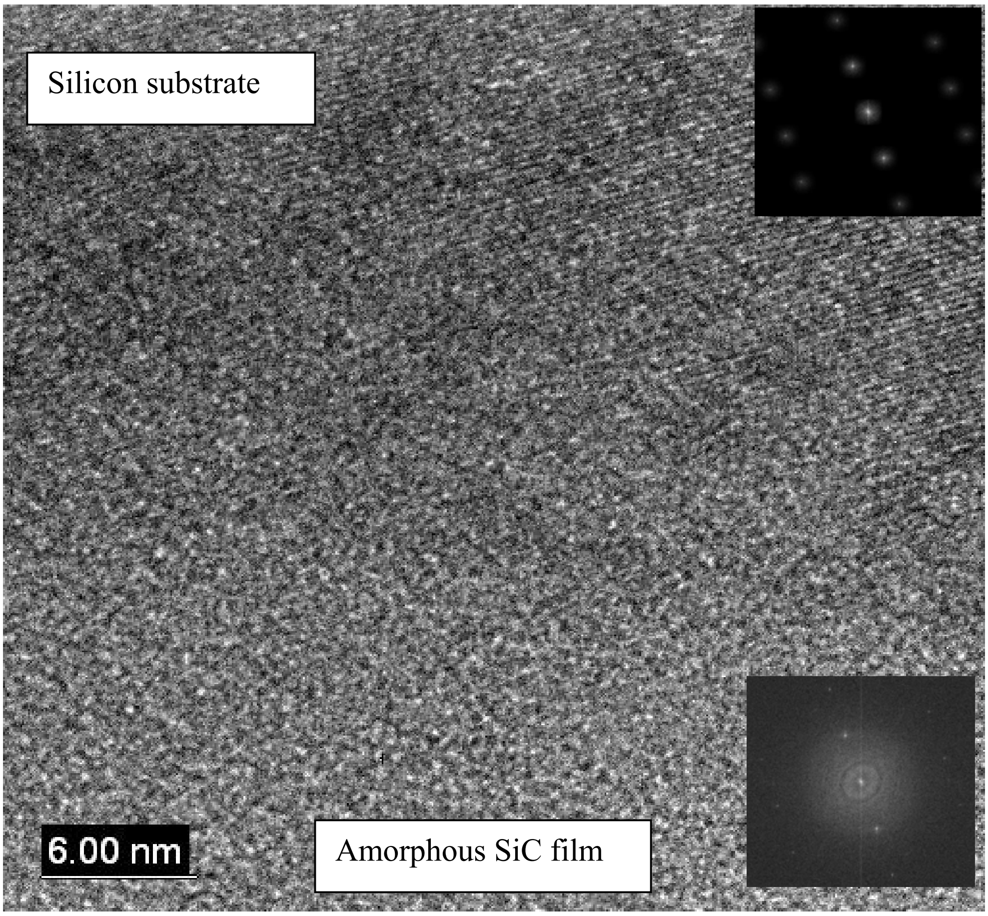

Fig. 6.2: *HRTEM micrograph: aspect of the amorphous SiC film sputtered on a silicon substrate. Electron diffraction of a selected area in the SiC film and in the silicon substrate (insets).*

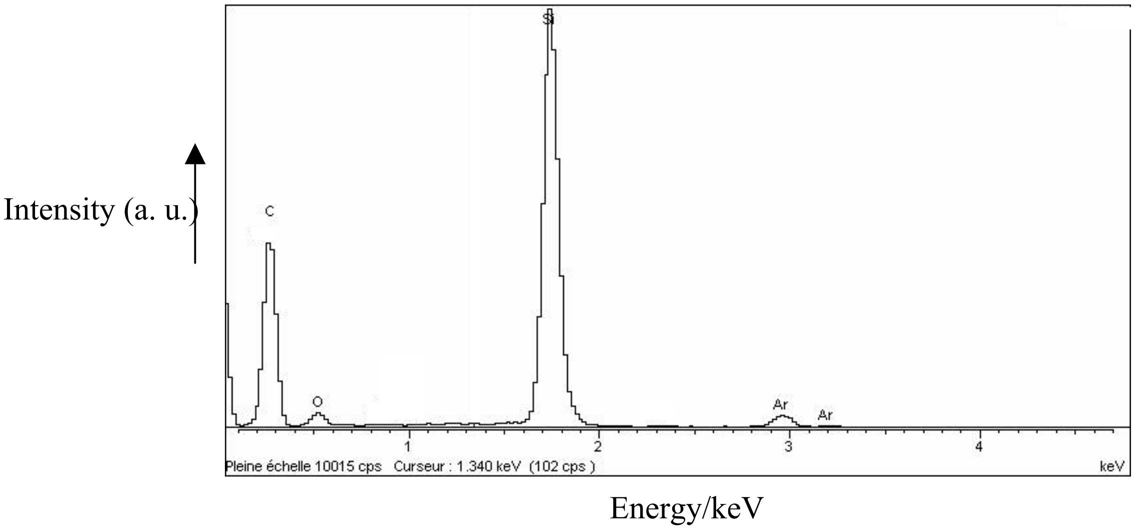

Fig. 6.3: *EDS spectrum of the amorphous SiC film deposited on the crystalline silicon substrate.*

A thermal treatment in the temperature range between 1100 °C and 1350 °C in argon atmosphere leads to the crystallisation of the films. Fig. 6.1 shows the exemplary XRD patterns of sputtered SiC on Si substrate before and after annealing at 1200 °C for different annealing times. The patterns for the crystallised phase show one strong characteristic peak at 41.6 ° and a second one located at 72 °, which can be indexed as the (111) and the (003) planes of the ß-SiC structure, respectively. For these films, the first small characteristic peak appears after 4 hours of annealing at about 1000 °C. No peaks were detected for temperatures below 1000 °C and reasonable times.

Further analysis was made with transmission electron microscopy to obtain more information about the size of the crystallites, their morphologies and their structures, and to confirm the crystallisation of the films. Fig. 6.4 shows a transmission electron micrograph of a cross-section of a sample on a silicon substrate annealed for 13 hours at 1275 °C. Small particles of around 50 nm wre observed. In the electron diffraction pattern (inset) three rings indicating the phase transition from amorphous film to the polycrystalline state can be seen. The shapes of the particles are very irregular but most of them tend to be ellipsoidal and spherical so that a three-dimensional growth of the particles can be assumed.

Indexing of the electron diffraction pattern shows that the first small ring corresponds to the (111) plane with an inter-planar spacing of d_{hkl} = 2.47 Å. The two other rings are consistent with the (220) and (311) planes having an inter-planar spacing of d_{hkl} = 1.49 Å and d_{hkl} = 1.28 Å, respectively. This indicates that the film crystallised into ß-SiC structure, which is the only SiC cubic polytype with a lattice parameter of the unit cell of $a = 4.25 \pm 0.1$ Å.

To determine quantitatively the amount of crystallised SiC formed during annealing, the following procedure was used: the amorphous films were annealed for a time t at a distinct temperature in the range between 1200 °C and 1300 °C, characterized with XRD and afterwards annealed again. The procedure was repeated until the degree of crystallisation remained constant. Fig. 6.1 illustrates the crystallisation process for the growth of the SiC-(111) X-ray peak at a Bragg angle of $2\Theta = 41.6$ ° as a function of annealing time at 1200°C.

An increase of the characteristic XRD peak with increasing time corresponding to the crystallisation of the film is observed. Under the assumption that the crystallised volume is proportional to the integrated intensity of a single X-ray peak, e.g. the (111) peak, the peak shape was fitted numerically with a Lorentzian function from which the peak area and consequently the volume of the precipitated compound were determined (Appendix 7.3, Fig. 7.13).

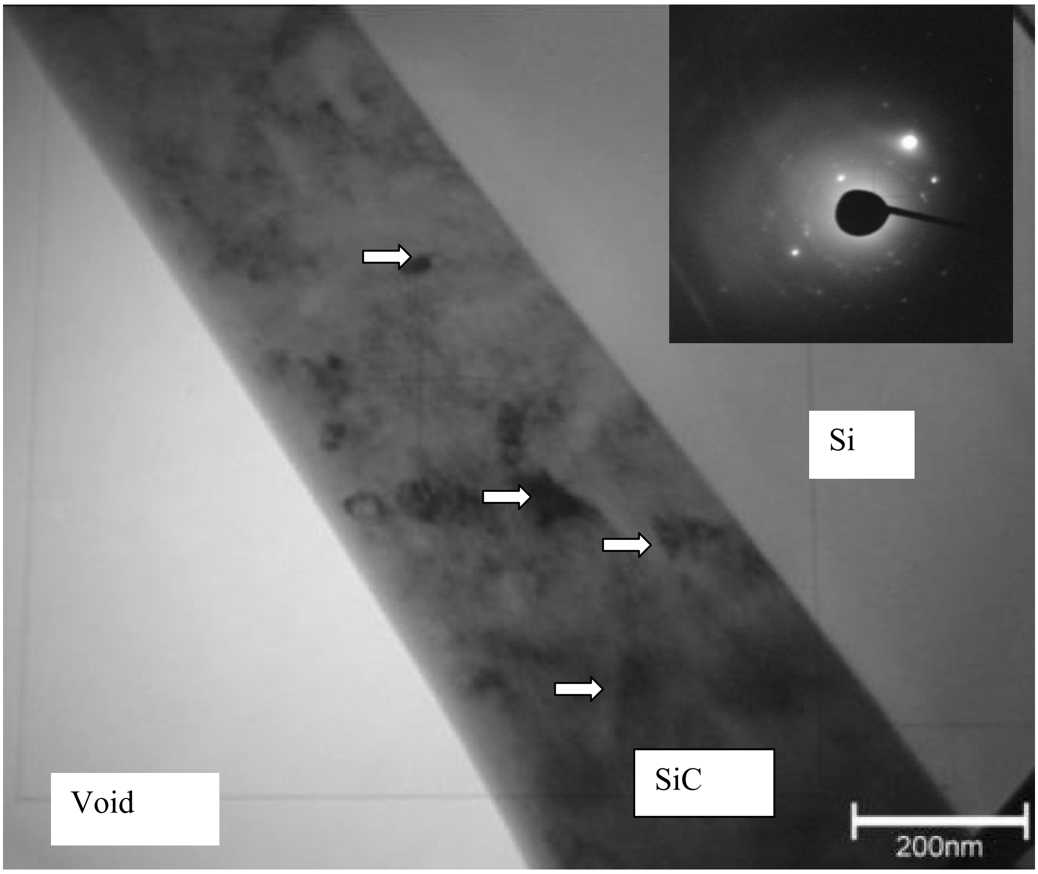

Fig. 6.4: *TEM micrograph of amorphous SiC film deposited on a silicon substrate and annealed at 1275 °C for 13 hours.*

The absolute volume of the crystallised phase V(t, T) can be determined from the measurement data. The normalized volume fraction can be calculated by converting the data according to $X(t,T) = \frac{V(t,T)}{V^{\max}(t,T)}$. $V^{\max}(t,T)$ is the corresponding value for the completely crystallized state.

Fig. 6.5 shows the typical crystallised *ß-SiC* fraction for SiC films annealed at 1250 °C. Due to its high intensity the (111) characteristic XRD peak is used for the analysis and for all samples. With increasing annealing time the evolution of the crystalline fraction follows a sigmoidal behaviour.

Numerical fitting of the (111) peak with the Lorentzian function leads to the determination of the full width at half maximum of the peak from which the average value of the crystallite size is calculated using the Scherrer formula $d = \frac{0.9\lambda}{F(2\theta)\cos\theta}$ where *d* is the average crystallite size, F is the Full Width at Half Maximum (FWHM), θ is the Bragg angle and λ is the wavelength of the radiation used. An average crystallite diameter ranging between 50 and 70 nm is found in accordance to the value obtained from the TEM micrographs. In order to evaluate the density of the crystallites the relationship between the crystallised fraction and the average radius in the case of three-dimensional growth of pre-existing nuclei (Appendix 7.3, equation (7.24a))

$$N_0 = \frac{-3\ln(1-X(t))}{4\pi r^3} \tag{6.1}$$

was used. Simultaneously, the evolution in time of the relative error $\frac{\Delta N_0}{N_0}$ was made (Appendix 8.3). From a relatively high error at the beginning of the process due to the poor accuracy in the measurement of FWHM, a minimum is achieved in the middle part of the kinetics. Afterwards, the error increases again so that a time dependence of the error as presented in Fig. 6.6 is obtained. Values of the density corresponding to a minimal error are taken into account. From the above procedure, an estimated average constant density of the nuclei of about $N_0 = (1.5 \pm 1.0) \times 10^{22}\, m^{-3}$ is determined independently of the temperature (Fig. 6.7). The size of the crystallites obtained from the TEM measurements corresponds to a density of pre-existing nuclei of about 1.5 x10^{22} m^{-3} indicating that the film is completely crystallised. This particle density is calculated according to $N_0 = \left(\frac{4\pi}{3} r^3\right)^{-1}$ using the average radius of spherical crystallites of 25 nm after complete crystallisation.

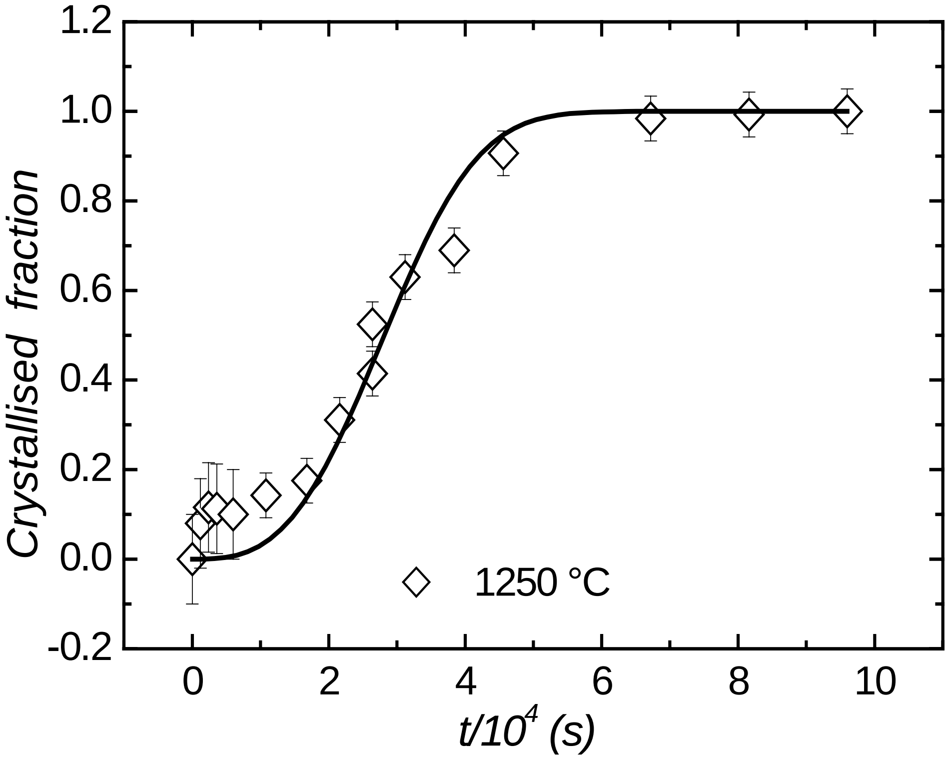

Fig. 6.5: *Evolution in time of the crystallised volume fraction of a SiC film deposited on a silicon substrate and annealed at 1250 °C. The solid line represents the fit with the JMAK equation (4.13).*

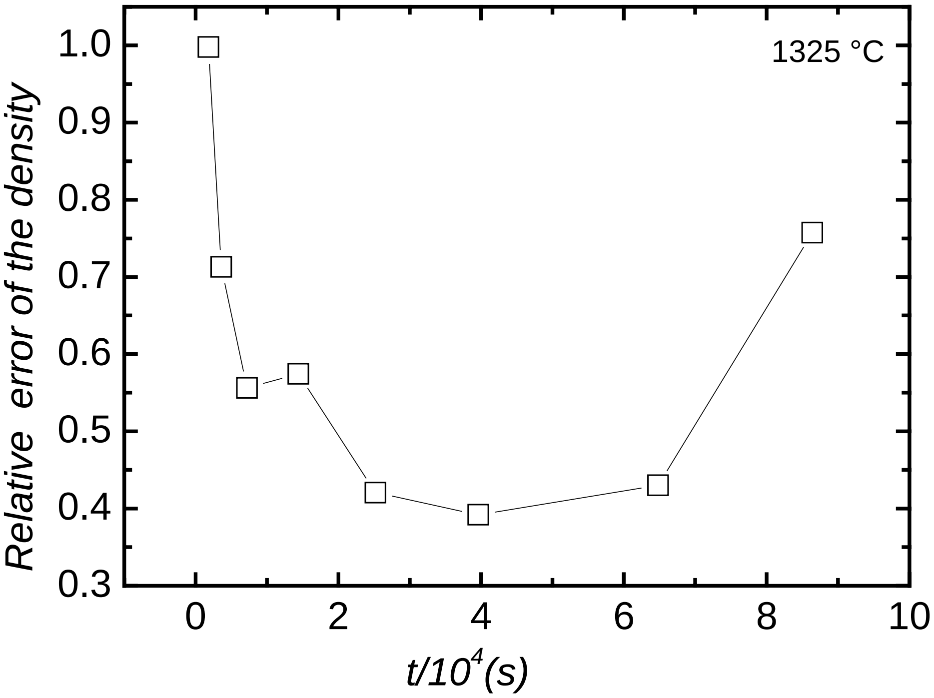

Fig. 6.6: *Amorphous SiC film deposited on a silicon substrate: relative error of the density of the pre-existing nuclei at 1325 °C.*

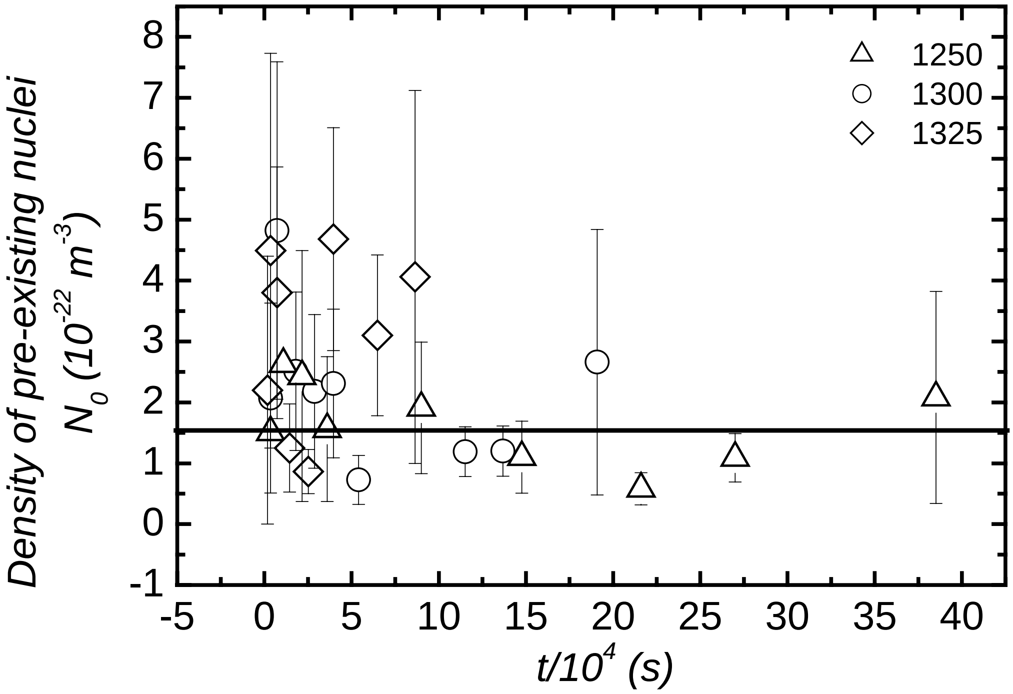

Fig. 6.7: Amorphous SiC film deposited on a silicon substrate: average estimated number density of pre-existing nuclei.

For a closer insight into the mechanisms of crystallisation, we first applied the classical JMAK theory in order to investigate the nucleation and growth of the crystallites. For homogeneous nucleation or for randomly distributed heterogeneous nucleation sites, and a constant growth velocity of the crystallites, the transformed volume fraction *X(t)* of a specimen after a time t is given by equation (4.13). Least squares fitting of the crystallised fraction to the JMAK equation leads to JMAK exponents between n = 1.6 to 2.5, but not to a value of n = 3, corresponding to three-dimensional growth. Fig. 6.5 shows an example of the classical JMAK equation describing the time dependence of the crystallised fraction. One can observe that the classical JMAK theory does not fit the earlier stages of the kinetics.

Further investigations were carried out under the assumption of a linear growth of the crystallites. The growth velocities for each temperature were estimated by plotting the crystallite sizes as a function of the annealing time and by taking the slope of the straight lines according to equation (4.13) corresponding to the case of an interface controlled growth. The typical dependence of the crystallized fraction and of the average crystallite radius on annealing time is given in Fig. 6.8 for films annealed at 1275 °C. Both quantities show a two-step behaviour. First we observe an increase of the crystallized fraction to about 30 % during the first 1×10^4 s of annealing. This increase is accompanied by a linear increase of the average crystallite size. At about $t^* = 1.4 \times 10^4$ s the growth of the crystallite size slows down and the crystallized fraction further increases with a lower rate. Both parts of the time dependence of the average crystallite radius can be fitted with straight lines, where from two rate constants of growth, U_1 and U_2, can be determined. The main increase of the crystallized fraction is associated with the lower growth rate U_2. However, due to the small variation of the average radius with increasing annealing time and the corresponding error bars, the rate constant rate U_2 can only be treated as a lower limit here. The first step of the crystallization is detectable qualitatively with our experimental methods (data points corresponding to an annealing time up to 1.4×10^4 s in Fig. 6.8). However, a quantitative analysis of the crystallized fraction is not straightforward. We assume that prior to the growth process detected by XRD, an additional growth process (or nucleation and growth processes) takes place in the early stages of crystallization. This leads to an overall two-stages process of crystallisation. The first process leads to the fast formation of crystallites in the order of 22 nm (e.g. within the first 1.4×10^4 s in case of the data of Fig. 6. 8). However, this process is connected only with the formation of a limited amount of crystalline phase (about 30 %). During the second process, which is connected with a slower growth rate, the rest of the amorphous material crystallizes.

Following these assumptions, the JMAK equation has to be modified in order to achieve a correct description of the data. For JMAK exponent of n = 3 and using $r = U(t - t^*) + r^*$ the equation $X(t) = 1 - \exp\left(-(4\pi/3) N_0 r^3\right)$ can be transformed to

$$X(t) = 1 - \exp\left(-\frac{4\pi}{3} N_0 \left(r^* + U(t - t^*)\right)^3\right) \tag{6.2}$$

where N_0 is the density of pre-existing crystallites, U is the rate constant of crystallite growth, t^* is the annealing time corresponding to the experimental data point where the two processes overlap, and the corresponding average radius r^* is defined as $r^* = r(t^*)$.

Fitting the second part of the kinetics with equation (6.2) using the density of pre-existing nuclei determined above, value of U_2 and r* are obtained (Table 6.1). An average value of r* ≈ 15 nm is obtained independent of the temperature. This value is small compared to a value of $r^* \approx 22$ nm as obtained from the direct measurement. The reasons of this difference will be discussed in paragraph (6.1.4).

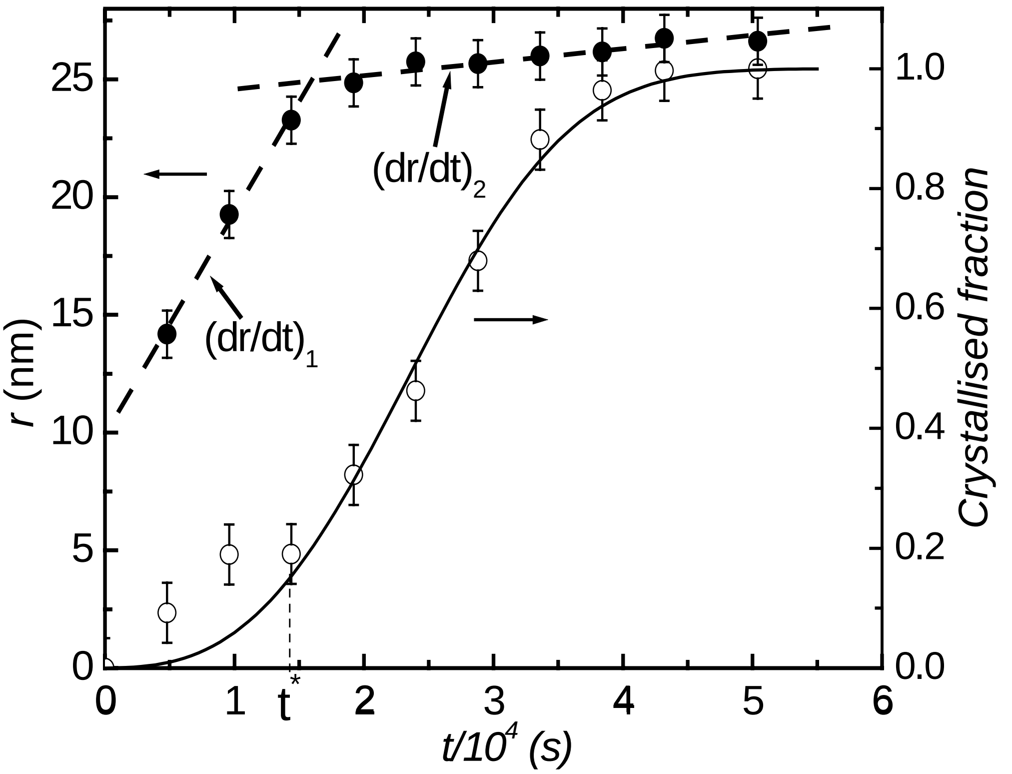

Fig. 6.8: *Normalized fraction of crystallized ß-SiC and average crystallite radius as a function of annealing time for a film deposited on a silicon substrate at 1275 °C. The solid line corresponds to a least-squares fit of the experimental data to equation (6.2) for t > t,* and the dotted straight lines indicate a two-step growth of crystallites.*

Table 6.1: *Rate constants of crystallite growth as obtained from the modified JMAK model according to equation (6.2) and directly from the annealing time dependence of the average crystallite radius for the films deposited on silicon substrates at different temperatures. The quantity* U_1 *describes the process in the early stages of crystallization and the quantity* U_2 *the slower process where most of the transformed volume is formed (see text). Also given is* t^**, the annealing time corresponding to the experimental data point, where the two processes overlap, and the corresponding average radius* r^**.*

Annealing temperature (°C)	Modified JMAK model		Directly			t^* (s)
	U_2 (10^{-13} m s^{-1})	r^* (nm)	U_1 (10^{-13} m s^{-1})	U_2 (10^{-13} m s^{-1})	r^* (nm)	
1200	1.9 ± 0.6	13 ± 1	-	0. 4	22 ± 1	17400
1250	6 ± 2	15 ± 1	7 ± 2	0.8	23 ± 1	16800
1275	9 ± 3	14 ± 1	8 ± 3	1	22 ± 1	14400
1300	12 ± 4	16 ± 1	12 ± 4	3	22 ± 1	7200
1350	40 ± 15	14 ± 1	-	-	23 ± 1	4800

6.1.2 Crystallisation of the films on glassy carbon substrates

The thermal annealing has been done at temperatures between 1500 °C and 1600 °C. Fig. 6.9 shows the XRD patterns of the films as deposited and annealed at 1600 °C for 4 hours. The broad peak at 50.8 ° belongs to the glassy carbon substrates. The as-deposited SiC film exhibits no peaks confirming the amorphous state of the film. The crystallisation temperatures of these films are higher than those on silicon substrate. The first small fraction of crystalline phase is detected at 1350 °C after 2 hours of annealing. In order to confirm this observation, two different samples with silicon and carbon substrates, respectively were annealed simultaneously at the same temperature (1350 °C) and for the same time. It comes out that the film deposited on a carbon substrate shows a broad peak proving that the process is only in the embryonic stage, whereas the crystallisation process of the film on a silicon substrate is already advanced as shown in Fig. 6.10. This suggests that a carbon substrate increases the thermal stability of the film at temperature above 1400 °C.

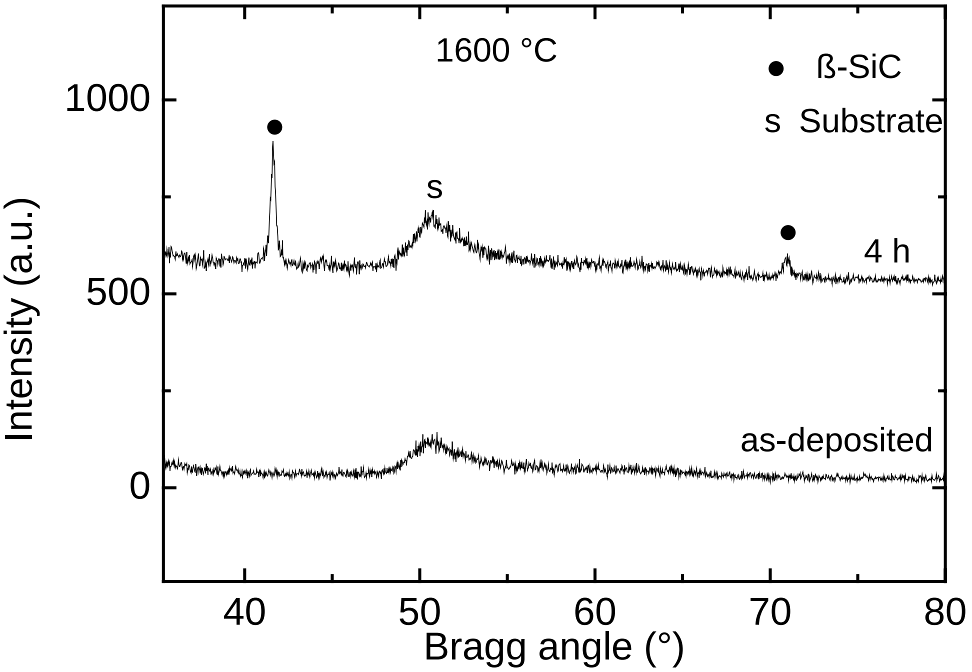

Fig. 6.9: *XRD patterns of as-deposited and annealed amorphous SiC film on a glassy carbon substrate. The sample was annealed at 1600 °C for 4 hours.*

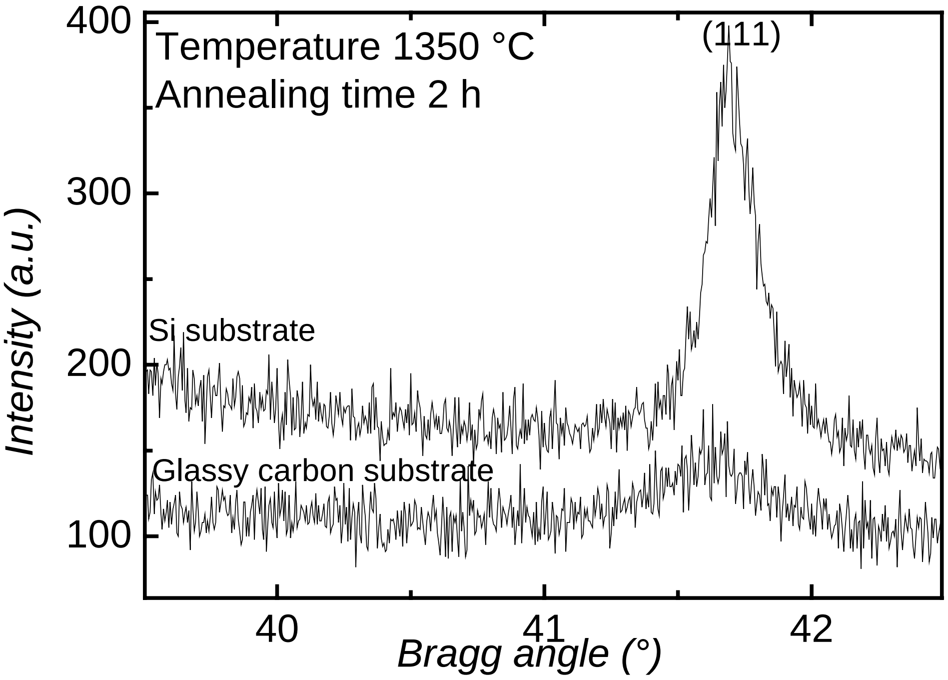

Fig. 6.10: *Degree of crystallisation of an amorphous SiC film deposited on silicon and carbon substrates, respectively.*

The cross-sectional transmission electron micrograph in Fig. 6.11 shows a film deposited on a carbon substrate, annealed at 1550 °C for 5 hours. It can be seen from the dark field image (Fig. 6.12) that some individual crystallites are quite large and very irregular in shape but most particles seem to follow a three-dimensional growth with ellipsoidal or spherical shape (with a maximum aspect ratio of about 1 : 3). An average diameter between 30 - 70 nm can be identified. Bright field images from the HRTEM showed a crystalline grain within which the atoms are periodically arranged (Fig. 6.13). The SAD (inset Fig. 6.12) indicates that the electron diffraction pattern has several rings. It should be emphasized that all the diffraction rings except the first inside the diffraction spot, are composed of many diffraction spots, which further supports the statement that the crystallites are polycrystalline. Several authors have made similar observations while investigating silicon carbide film or bulk matrial synthesized in different ways [Yu00], [Cai01]. As in the case of the films sputtered on a silicon substrate, the diffraction pattern confirms that the films deposited on a glassy carbon substrate crystallise in the ß-SiC structure.

With increasing annealing time, the amount of the crystalline phase increases as shown in Fig. 6.14 for an illustration of the growth of the (111) peak. Fig. 6.15 shows evolution in time of the crystallised fraction for a sample annealed at 1550 °C. The saturation of the signal can be observed after 2 hours of annealing, which corresponds to the full crystallisation of the amorphous film. This observation indicates that the glassy carbon substrate increases the stability of the SiC films.

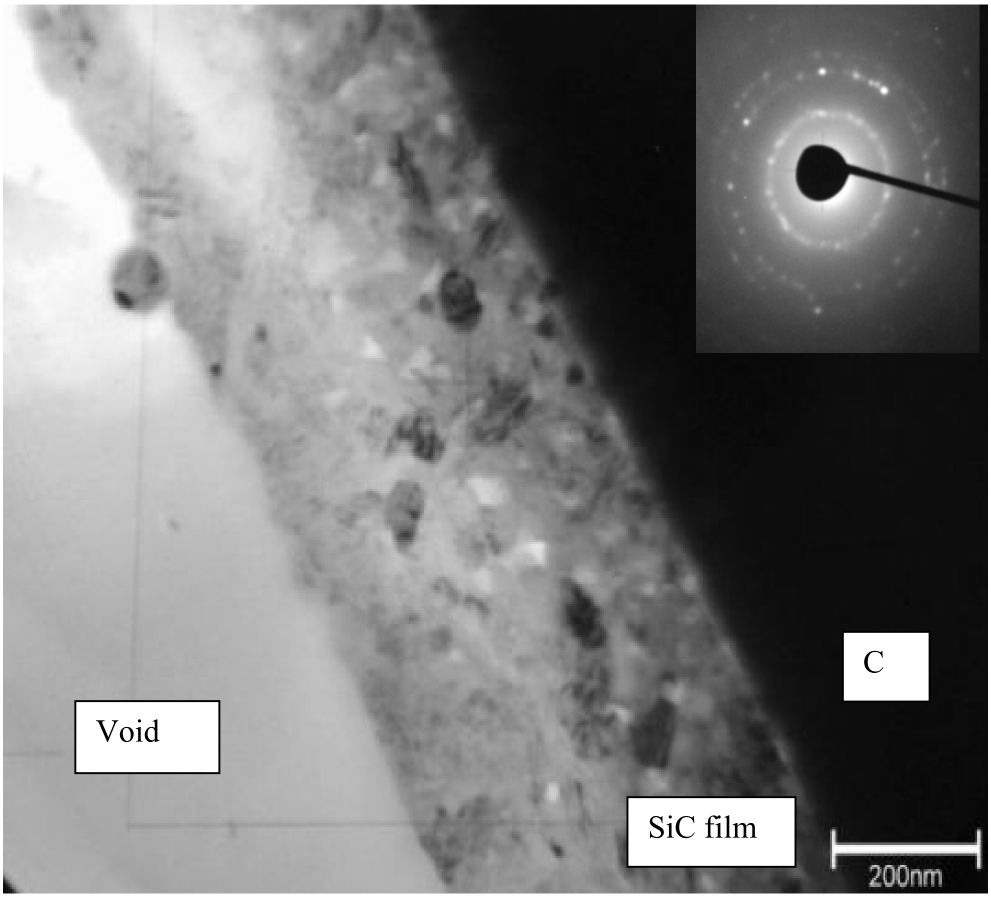

Fig. 6.11: *TEM micrograph: bright field image of an amorphous SiC film deposited on a glassy carbon substrate and annealed at 1550 °C for 6 hours. The contrast (black and white) in the film corresponds to crystallites with different orientations. Inset corresponds to the SAD of the crystallised SiC film. Each ring corresponds to a diffraction plane.*

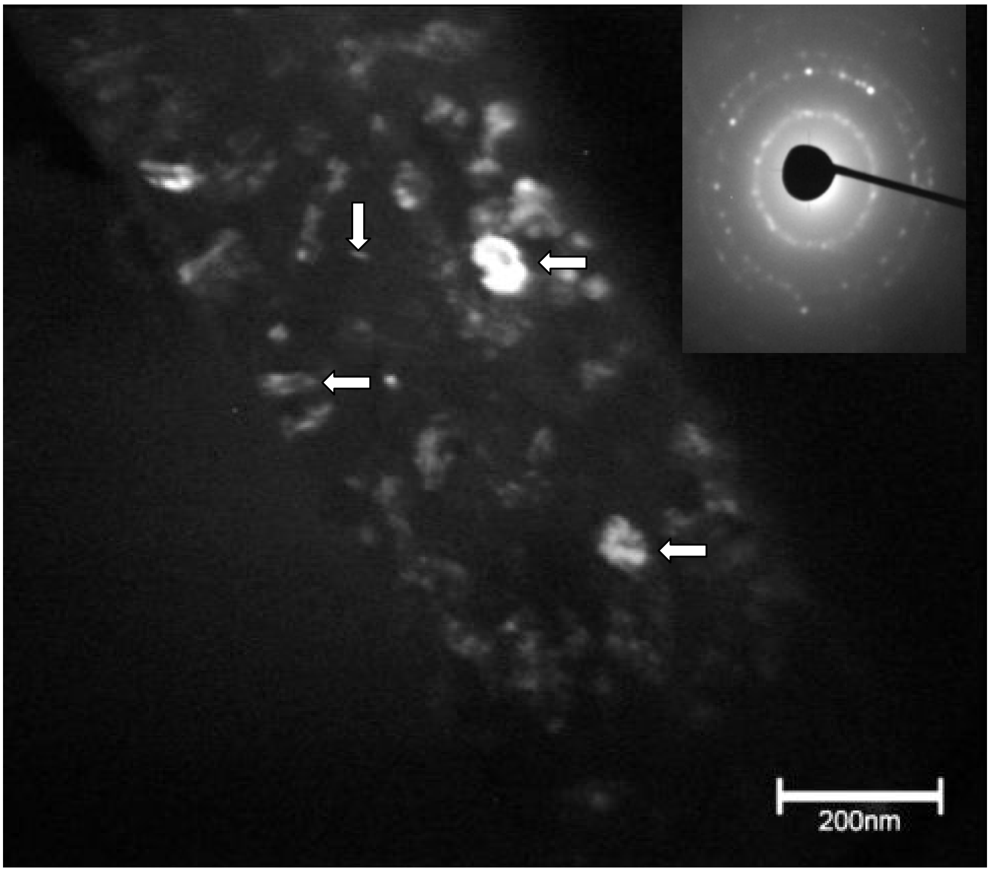

Fig. 6.12: *TEM micrograph: dark field image of an amorphous SiC film deposited on a glassy carbon substrate and annealed at 1550 °C for 6 hours. The arrows indicate the crystallites within the film.*

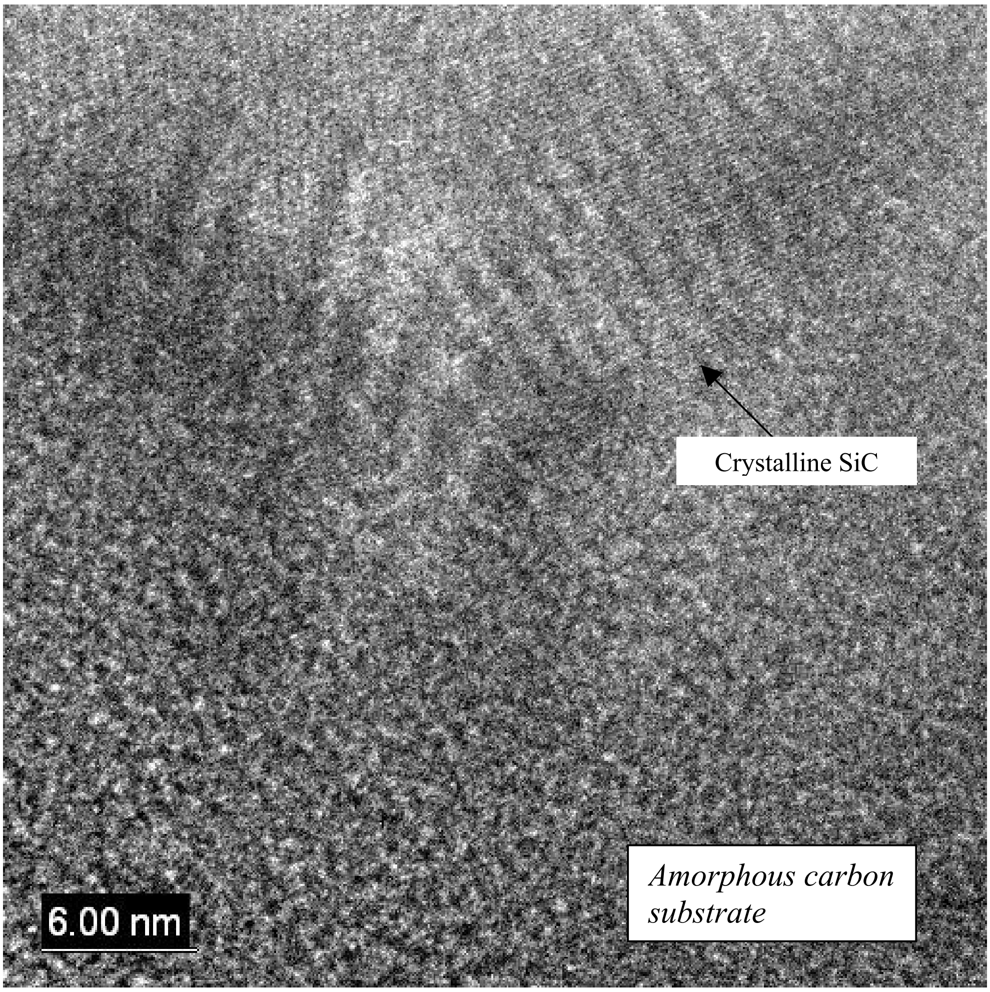

Fig. 6.13: *HRTEM micrograph of the crystallised SiC film: isolated crystallite on an amorphous carbon substrate. Crystal planes with ordered atoms can be observed.*

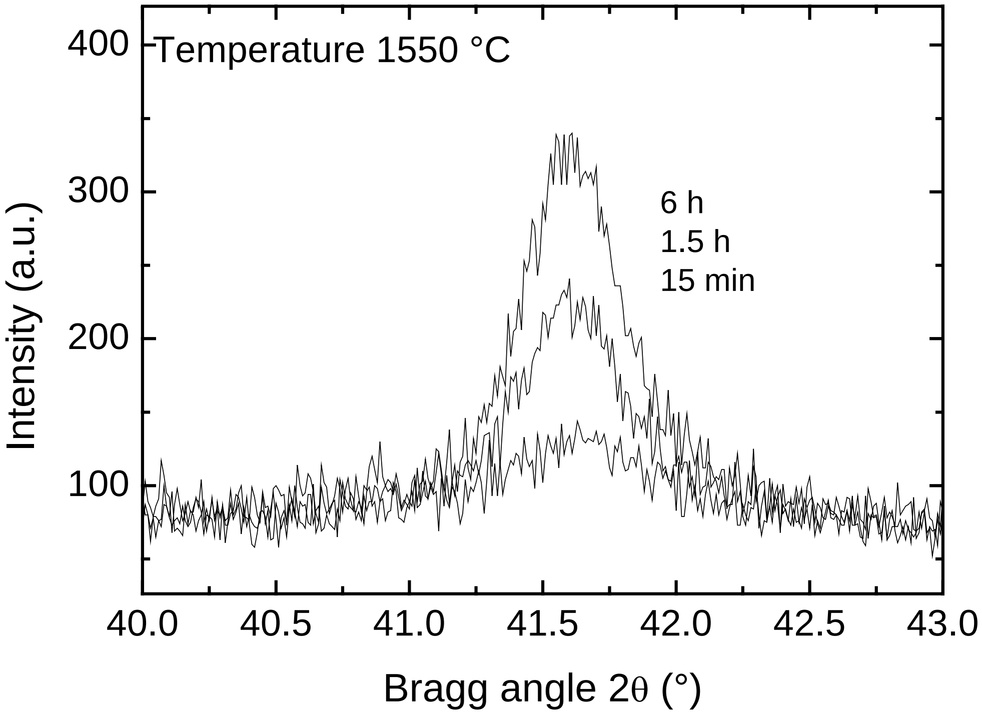

Fig. 6.14: *Amorphous SiC film deposited on a glassy carbon substrate: growth of the (111)-reflex of the ß-SiC structure with increasing time.*

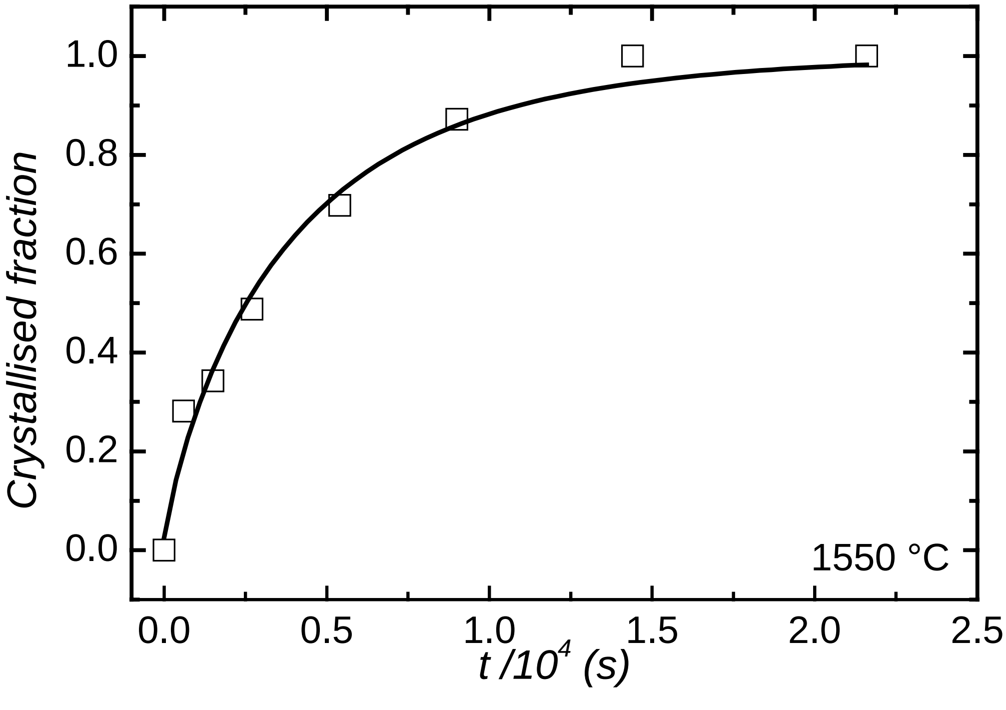

Fig. 6.15: *Crystallised fraction of the amorphous SiC film sputtered on a glassy carbon substrate fitted with the classical JMAK equation.*

The best fit of the crystallised fraction with equation (4.13) leads to a growth exponent of about n = 0.9 ± 0.2 indicating a one dimensional growth with pre-existing nuclei which is in contradiction to the morphologies of the crystallites observed by TEM measurements. This behaviour is obtained for all data sets in the temperature range investigated with n ranging from 0.7 to 1.2. These findings suggest that crystallisation of the amorphous films deposited on glassy carbon substrates proceeds in a different way. Fig. 6.16 shows exemplarily the time evolution of the average crystallite radius r at 1550 °C for a maximum annealing time of 5 hours. In the early stages of the growth process, the experimental data follow a straight line, in accordance with an interface controlled growth behaviour. In later stages of the process deviations are present which are due to the impingement of the growing crystallites. This linear growth is observed in the same time interval where the crystallised fraction increases significantly. A least squares fitting of the experimentally determined average crystallite radius to a straight line results in the determination of the rate constant of crystallite growth, U, which is given in Table. 6.2 for different temperatures. An average crystallite radius of about 11 nm which is determined by extrapolating the data in Fig. 6.16 to $t = 0$ is surprisingly high, indicating that this value cannot be associated with the critical radius of nucleus formation, $R_{c,}$ which should be in the order of 0.5 – 2 nm (see [Spi98] for the case of silicon). Consequently, this value has to be interpreted in a different way. We assume that prior to the growth process detected by XRD, and addition growth process (or nucleation and growth process) takes place in the early stages of the crystallisation on a time scale, which cannot be resolved with the present experimental equipment. Therefore t^* in considered here as the annealing time where the first experimental data point is measured. Using equation (6.2) an excellent description of the time dependence of the crystallised fraction is possible, under the consideration of a three dimensional growth (Fig. 6.16). Consequently, the value of $n \approx 1$ of the JMAK exponent, which is determined with the conventional JMAK theory leads to an erroneous interpretation of the experimental data as a one dimensional growth process. For the fitting procedure a constant value of $N_0 = 9.0 \times 10^{22}$ m^{-3} is used for the density of the crystallites, independent of temperature. This particle density is calculated using an average radius of spherical crystallites of r = 14 nm as obtained by XRD measurements for a complete crystallization of the amorphous film. Using this value, fitting of the experimental data to equation (6.2) results in the determination of U and r^*, which are nearly uncorrelated quantities for the present case. The results are given in Table 6. 2. It is obvious that the values of r^* determined here are identical to the values obtained directly from the full width at half maximum of the Bragg peak using the Scherrer equation at t^*, showing the consistency of our fitting procedure. A detailed analysis of the rate constants of growth will be carried out in section. 6.1.4.

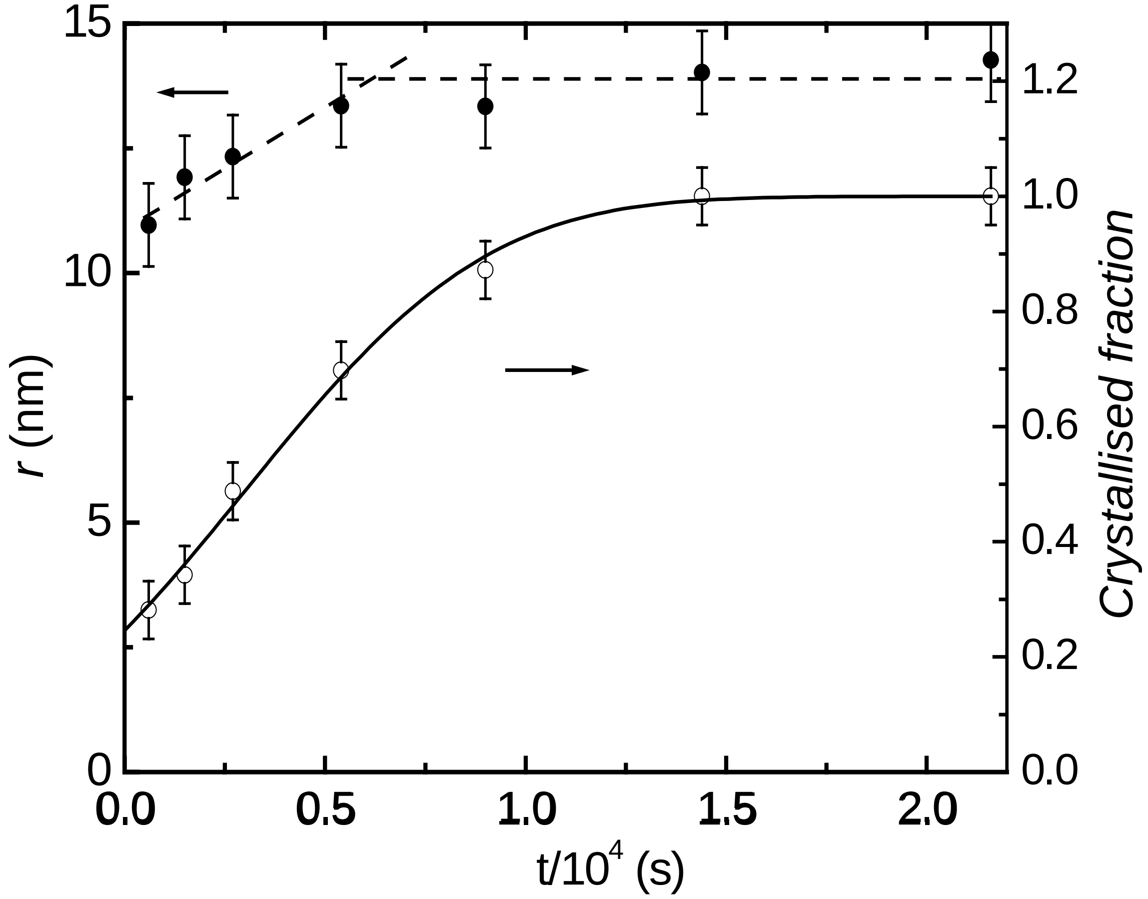

Fig. 6.16: Normalized fraction of crystallized ß-SiC and average crystallite radius as a function of annealing time for a film deposited on a glassy carbon substrate at 1550 °C. The solid line corresponds to a least-squares fit of the experimental data to equation (6.), and the dotted straight line indicates an interface-controlled growth of crystallites. t^* *is considered as the annealing time where the first experimental data point is measured. For further details see paragraph 6.1.2.*

Table 6.2: *Rate constants of crystallite growth, U, as obtained from the modified JMAK model according to equation (6.2), and directly from the annealing time dependence of the average crystallite radius for the films deposited on a glassy carbon substrates at different temperatures. Also given is* t^**, the annealing time corresponding to the first experimental data point and the corresponding average radius* r^**. For further details see paragraph 6.1.2.*

Annealing temperature (°C)	Modified JMAK model		Directly		t^* (s)
	U (10^{-13} m s^{-1})	r^* (nm)	U (10^{-13} m s^{-1})	r^* (nm)	
1500	3.8 ± 1.0	10 ± 1	2.0 ± 0.9	7 ± 1	5400
1525	11 ± 2	9 ± 1	2.7 ± 0.8	10 ± 1	600
1550	13 ± 4	9 ± 1	4.6 ± 1.5	11 ± 1	600
1575	52 ± 16	11 ± 1	18 ± 6	11 ± 1	300
1600	84 ± 25	11 ± 1	-	12 ± 1	150

6.1.3 Crystallisation of $Si_{0.33}C_{0.67}$ deposited on crystalline silicon substrates

This part of the work is concerned with the crystallisation behaviour of amorphous material of nominal composition “$Si_{0.33}C_{0.67}$” deposited on a crystalline silicon substrate. The thermal treatment as well as the procedure of the determination of the amount of the crystallised phase was done in the same manner as in the previous cases.

The diffraction patterns of the as-deposited films exhibited characteristic peaks corresponding to the silicon substrate. After thermal annealing at 1250 °C, new Bragg peaks were detected. These Bragg peaks correspond to the crystalline β-SiC structure (Fig. 6.17). The amorphous “$Si_{0.33}C_{0.67}$” films were also stable in the same temperature range as for the amorphous SiC films deposited on crystalline silicon. The direct determination of the size of the crystallites using the Scherrer equation leads to average values ranging between 50 nm and 60 nm providing the same density of pre-existing nuclei as for amorphous SiC films deposited on silicon substrates.

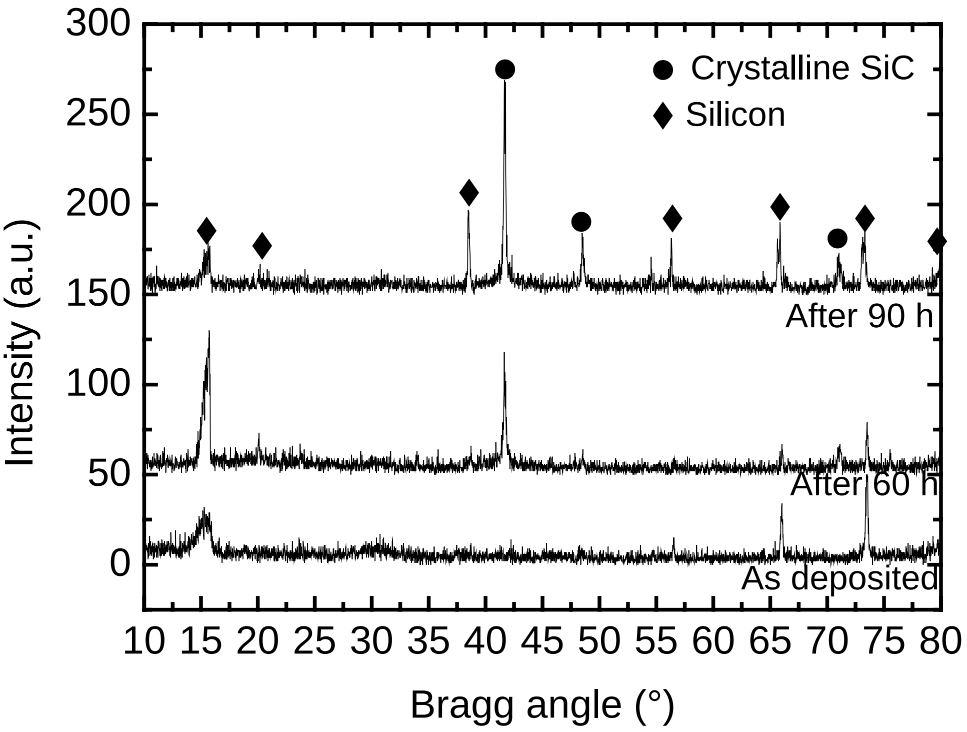

Fig. 6.17: *XRD patterns of as-deposited and of annealed* $Si_{0.33}C_{0.67}$ *films. The formation of the crystalline SiC phase after annealing at 1250 °C for 60 hours can be observed.*

Similarly to amorphous films deposited on a silicon substrate, the crystallised fraction increases rapidly at the beginning of the process followed by a plateau. Afterwards, a second increase with a slower growth rate is observed until the end of the crystallisation. Therefore, the time dependent crystallisation kinetics can be divided into two pronounced stages (Fig. 6.18). A possible explanation of this multiple-step behaviour can be the phase separation from the amorphous $Si_{0.33}C_{0.67}$ into amorphous SiC and carbon due to the annealing at the beginning of the crystallisation. Thus, amorphous domains of SiC in a carbon-rich matrix are formed. This first stage leads also to a fast formation of crystallites in the order of 15 nm. However, this process is connected only with the formation of a limited amount of crystalline phase (about 30 %). The crystallisation of the rest of the amorphous SiC with a slower growth rate corresponds to the second stage with sigmoidal time dependent crystallisation kinetics. Therefore, we can postulate that at least two consecutive mechanisms are taking place in the $Si_{0.33}C_{0.67}$ film. Assuming a three-dimensional growth of pre-existing nuclei an equation similar to equation (6.2) in the case of a diffusion-controlled process can be derived:

$$X(T,t) = 1 - \exp\left(-\frac{4}{3}\pi N_0 \left(r^* + \sqrt{2D}\left(\sqrt{t} - \sqrt{t^*}\right)\right)^3 \right) \tag{6.3}$$

where D is the diffusion coefficient of the rate determining species

A least squares fit of the experimental kinetics to equation (6.3) yields the diffusion coefficients as well as the radius of the particles observed at the beginning of the second stage of the process. In Fig. 6.18 the time dependence of the crystallisation kinetics fitted with equation (6.3) as well the radius of the crystallites are given. It is difficult to define a rate constant in the first stage since the processes (nucleation and/or growth) connected in this part of the kinetics cannot be separated. In the first stage the radius of the crystallites is relatively constant. Afterwards an increase corresponding to the growth process is observed until the end of the crystallisation. The size of the crystallites was plotted as a function of annealing time from which the diffusion coefficient was calculated (Fig. 6.19). The first stage being a mixing of phase separation, nucleation and growth, only crystallite sizes corresponding to the effective growth of the crystallites (second stage of the kinetics) were taken into account. As the crystallisation process is assumed to be controlled by diffusion the relation $r \approx \sqrt{2Dt}$ is used to fit the time dependent crystallite size. The obtained diffusion coefficients are given in Table 6. 3.

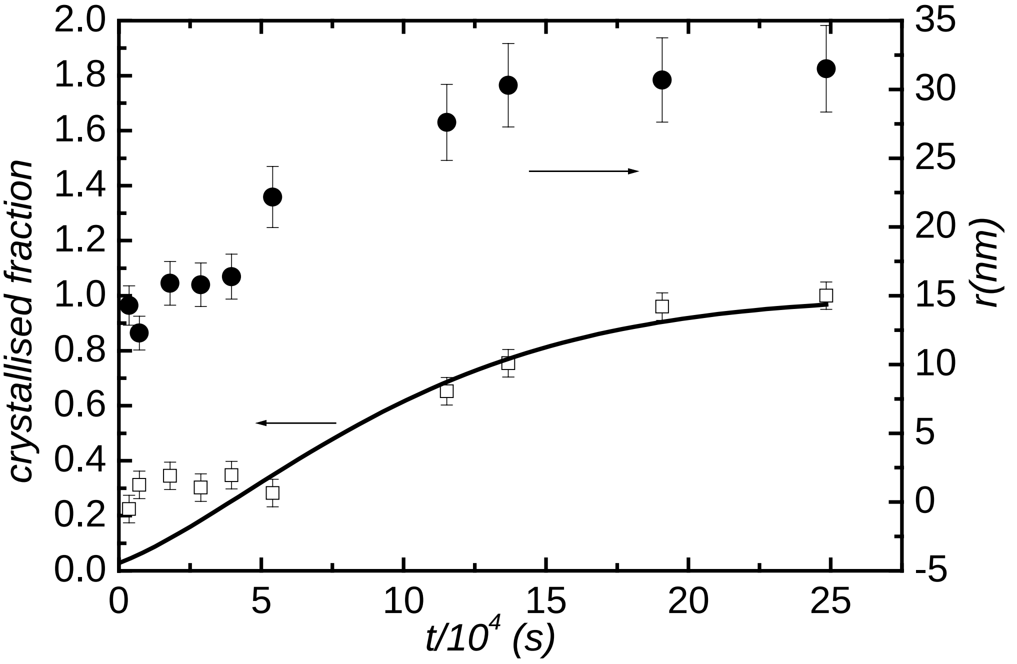

Fig. 6.18: *Two-step crystallisation kinetics of $Si_{0.33}C_{0.67}$ film deposited on a silicon substrate and annealed at 1300 °C. The solid line represents the least-squares fit to equation (6.3). The radius of crystallites is also given.*

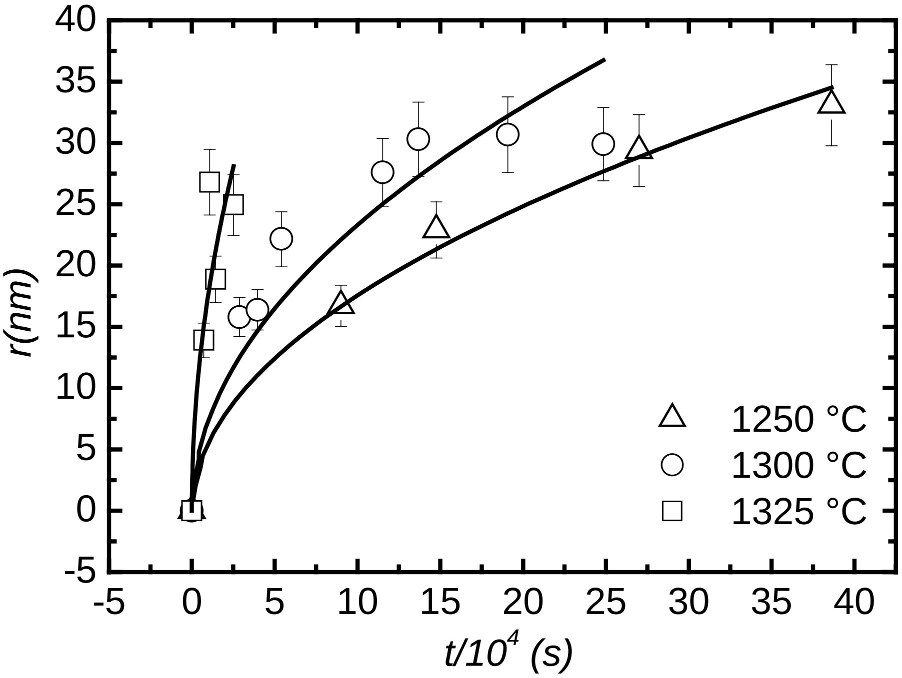

Fig. 6.19: *Amorphous "$Si_{0.33}C_{0.67}$" films deposited on a silicon substrate: (assumed) parabolic time dependence of the crystallites size at different temperatures.*

Table 6.3: *Diffusion coefficients corresponding to the second stage of kinetics as obtained from the modified JMAK model according to equation (6.3) and directly from the Scherrer equation for $Si_{0.33}C_{0.67}$ films deposited on a silicon substrate. Also given is t^*, the annealing time corresponding to the experimental data point, where the two processes overlap, and the corresponding average radius r^*.*

Annealing temperature (°C)	Modified JMAK model (equation 6.3)		Directly from the Scherrer equation		t* (s)
	D (10^{-21} m^2 s^{-1})	r* (nm)	D (10^{-21} m^2 s-1)	r* (nm)	
1250	0.9 ± 0.2	13.9 ± 3	1.6 ± 0.08	16.9 ± 1	3.6 x 10^4
1300	2.0 ± 0.4	15.9 ± 2.5	2.7 ± 0.35	15.8 ± 1	2.88 x 10^4
1325	5.1 ± 0.6	16.9 ± 2	9.4 ± 0.28	18.9 ± 1	1.44 x 10^4

6.1.4 Activation enthalpies and growth model

The growth rates obtained in sections (6.1.1) and (6.1.2) for the late stages of the transformation where most of the amorphous volume has crystallised have been plotted as a function of reciprocal temperature in Fig. 6.20.

Concerning the amorphous films deposited on glassy carbon and silicon substrates, growth rates calculated using equation (6.2) and those determined directly with the Scherrer equation have to be distinguished. The growth rates derived from the modified JMAK equation are higher by a factor of five or ten respectively, than the directly measured values for SiC films deposited on silicon or glassy carbon substrates, respectively. The reason for this is still unclear at the moment, but a possible reason might be microscopic strain that evolves during the crystallization process. Such strain will lead to an incorrect determination of the average grain radius from the full width at half maximum of the Bragg peaks according to the Scherrer equation, $d = 2R = \frac{0.9\lambda}{F(2\theta)\cos\theta}$. In order to calculate an average grain radius in the presence of microscopic strain (ε), it is more correct to apply the Williamson-Hall equation [Klu74]

$$\frac{F(2\theta)\cos\theta}{\lambda} = \frac{1}{2R} + \varepsilon\frac{4\sin\theta}{\lambda} \tag{6.4}$$

where 2θ is the Bragg angle and $\lambda = 0.1789$ nm is the wave length of the Co tube radiation. However , such and analysis is not possible in the present case due to a too small number of Bragg peak available for a quantitative analysis. If the Scherrer equation is applied in the presence of strain, the calculated average grain radius is underestimated. Let us assume a scenario, where at the beginning of the growth process no micro-strain is present, but a certain value ε_e at the end of the growth process. Consequently, the grain radius at the beginning of the growth process of 10 nm (see Fig. 6.16) is determined correctly, however, at the end of the process a crystallite radius of $R^{\mathrm{corr.}} = 17$ nm would be present instead of $R^{\mathrm{incorr.}} = 14$ nm (see Fig. 6.16) as calculated from equation (6.4) by

$$\frac{1}{R^{corr.}} = \frac{1}{R^{incorr.}} - \varepsilon_e\frac{8\sin\theta}{\lambda} \tag{6.5}$$

for a Bragg peak at $2\theta = 41.6\,°$ and a microscopic strain of only $\varepsilon_e = 8 \times 10^{-4}$. This would result in a higher growth rate, which would be identical to the value derived from the modified JMAK equation. The evolution of the micro-strain during the crystallization can be explained by the two different mass densities of amorphous (2.75 g cm^{-3}) and crystalline SiC (3.21g cm^{-3}) [Hee97].

According to the classical theory of interface controlled nucleation and growth, for processes with site saturation the temperature dependence of the rate constants of growth follow the

Arrhenius behaviour identical to equation (4.11) with a pre-exponential factor U_0. ΔH_g is the activation enthalpy that is needed to transfer an atom across the interface between the amorphous and the crystalline phases and its subsequent incorporation into the crystal lattice. For the experimental data analysed with equation (6.2) a high activation enthalpy of $\Delta H_g = (8.9 \pm 0.9)$ eV is determined for the films on glassy carbon substrates, while for the films on a silicon substrate a much lower activation enthalpy of $\Delta H_g = (4.1 \pm 0.7)$ eV is obtained. The data directly obtained from the growth of the crystallites are also shown in Fig. 6.20, with an activation enthalpy of $\Delta H_g = (8.0 \pm 2.0)$ eV and $\Delta H_g = (3.9 \pm 0.8)$ eV, respectively, which coincide with the values obtained from kinetic analysis (equation 6.2) within the estimated margins of error. The activation enthalpies are listed together with the pre-exponential factors, U_0, in Table. 6.4. The slower crystallization behaviour of the films on glassy carbon substrate can be described by a significantly larger activation enthalpy and a smaller pre-exponential factor.

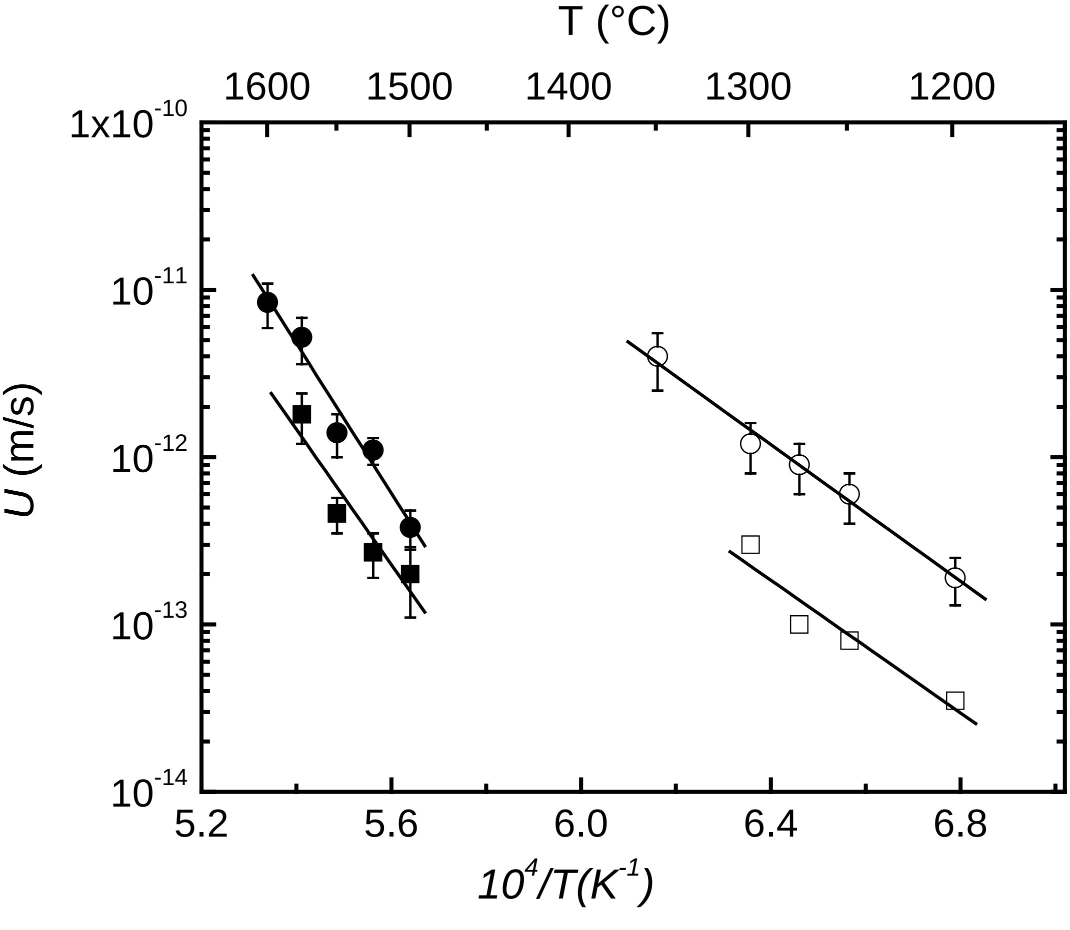

Fig. 6.20: *Rate constants of crystallite growth, U, as a function of reciprocal temperature for SiC on Si substrates (open symbols) and SiC on glassy carbon substrates (full symbols). The values are obtained from a least squares fit of the modified JMAK model according to equation (6.2) (circles) and directly from the average crystallite radius (squares). The values of the latter data set are lower limits.*

Regarding the films on silicon substrates, one important observation is that the obtained activation enthalpy is in good agreement with the values measured by other authors [Cal01], [Sho87]. The activation enthalpy obtained here corresponds only to the growth process since the crystallisation kinetics referred to the growth from pre-existing nuclei. This result indicates that the growth plays the dominant role in the crystallisation process of amorphous SiC.

Tentatively, these activation enthalpies can be interpreted as the activation enthalpies for the self-diffusion of Si or C in the crystalline or amorphous state, i.e. the jump of atoms through the interface between the crystalline phase and the amorphous matrix. The values of theactivation enthalpies of self-diffusion of Si and C in crystalline bulk SiC are $\Delta H_{SD} = 7.22\ eV$ and $\Delta H_{SD} = 7.41\ eV$ respectively [Hon80], [Hon81]. These values are in acceptable agreement with $\Delta H_g = 8.9$ eV for SiC deposited on glassy carbon, indicating that here an intrinsic value is measured. For interface controlled growth, the pre-exponential factor of the rate constant in equation (4.11) can be approximated by $U_0 = b\nu_0 \exp\left(\frac{\Delta S^I}{k_B}\right) = \frac{D_0}{a}$ where $b \approx 0.3$ nm is the distance the interface moves per atomic rearrangement, ν_0 is an attempt frequency, which corresponds approximately to the Debye frequency ν_D, D_0 is the pre-exponential factor of the self-diffusivity and $\Delta S^I = \Delta S^D$ is the entropy change for the transfer process across the amorphous/crystalline interface, which is approximately the entropy of self-diffusion. From the above relation values of $\Delta S^I \approx (21 \pm 5)\ k_B$ for films on glassy carbon substrates and $\Delta S^I \approx -(6 \pm 3)\ k_B$ for films on Si substrates were calculated from the experimental data. The first value seems to be relatively large, if it is compared to the entropy of self-diffusion of $\Delta S^D \approx 0 - 5\ k_B$ commonly found in metals [Phi91]. However, it has to be kept in mind that the entropy of self-diffusion in SiC is also in the order of 20 k_B, as calculated from the pre-exponential factor of $D_0 \approx 10^2$ m^2/s [Hon80], so that this value is quite reasonable within estimated errors.

In contrast, for SiC films on Si substrates a large negative value of ΔS^D is obtained. To explain this, a more detailed look on the self-diffusion mechanism in SiC is necessary. Under the quite reasonable assumption of a point defect mediated self-diffusion mechanism, the incorporation of an atom from the amorphous phase into the crystallite is defect mediated. The activation enthalpy of self-diffusion is commonly expressed by $\Delta H^D = \Delta H^f + \Delta H^m$, with the latter quantities being the enthalpies of point defect formation and of atomic migration, respectively. The entropy of diffusion $\Delta S^D = \Delta S^f + \Delta S^m$ is also composed of a formation and a migration trem. The considerably lower activation enthalpy of SiC on Si substrates can now be explained under the assumption that a considerable, temperature independent mole fraction of non-equilibrium point defects, c_d, is present in SiC at the temperatures under investigation. These point defects may accelerate the transfer of an atom across the amorphous/crystalline interface. Due to the supersaturation of the point defects at the phase boundary, the activation enthalpy of crystallization is now essentially determined by the migration enthalpy of the point defects $\Delta H^c \approx \Delta H^\mathrm{m}$. Assuming $\Delta H^\mathrm{m} \approx \Delta H^\mathrm{f} \approx 0.5\ \Delta H^\mathrm{D}$ as a crude approximation, and $\Delta H^\mathrm{D} = 8.9$ eV for the films on glassy carbon substrates, a value of $\Delta H^\mathrm{D} \approx 4.5$ eV is calculated for the films on Si substrates in accordance with the experimentally derived value. For the pre-exponential factor we get now $U_0 = b\,\nu_0 c_d \exp\left(\frac{\Delta S^m}{k_b}\right)$. A possible explanation for the presence of superabundant point defects in SiC might be found in the fact that the Si substrate is a point defect source. The temperature where our experiments are carried out is only 100 - 200 °C below the melting point of silicon at 1412 °C. At this temperature appreciably more point defects (vacancies or interstitials) are present in Si than SiC with a melting point of 2830 °C [Sca60], which try to equilibrate due to a net point defect flux into the SiC layer. According to Ref. [Tan85] the mole fraction of vacancies and interstitials in silicon is about 2 x 10^{-6} close to the melting point. Using the above relation and ΔS^m(Si substrate) $\approx \Delta S^\mathrm{f}$ (Si substrate) $\approx$ 0.5 ΔS^I(glassy carbon substrate) a value of $c_\mathrm{d} \approx 10^{-7}$ can be assessed for the mole fraction of superabundant point defects in SiC, which is quite reasonable. In contrast, glassy carbon is stable up to 3000 °C in inert atmosphere and the point defect concentration has to be relatively low at the temperatures of investigation. However, more detailed work on that interesting topic is necessary to verify the mechanism suggested here.

In principle, a further possibility to explain the differences in the crystallization behaviour between a SiC film deposited on silicon or glassy carbon substrates might be found in an inward diffusion of Si or C atoms from the substrate into the partially crystallized film, where the atoms can segregate at the newly formed grain boundaries and influence the transfer of atoms. To achieve this scenario, the Si or C atoms of the substrate have to diffuse across the whole amorphous SiC layer (0.5 µm) within about 1 hour of annealing at about 1200 °C, which needs a diffusivity in amorphous SiC of at least $D^\mathrm{a} \approx 10^{-17}$ m^2/s. The extrapolated Si and C diffusivities in crystalline SiC at 1200 °C are about $D^\mathrm{c} = 10^{-26}$ m^2/s [Hon80], [Hon81]. According to investigations made in our research group on self-diffusion in covalently bound materials [Sch04], the self-diffusivities of Si_3N_4 are quite similar in the amorphous and in the crystalline state. Assuming that in SiC the same is true, the difference of nine orders of magnitude makes the suggested scenario extremely unlikely.

The influence of point defects on the crystallization behaviour is also reflected in the first crystallization step which takes place before the main transformation and may lead to an erroneous interpretation in the framework of the conventional JMAK formalism. Here, it can be speculated that a supersaturation of point defects or excess free volume is present in the amorphous films due to the preparation with magnetron sputtering. These non-equilibrium point defects are equilibrated during the very first stages of annealing. During this time crystallite formation is accelerated.

Table 6.4: *Activation enthalpies of crystallization, ΔH_g, and pre-exponential factors, U_0, for SiC films deposited on a glassy carbon and a silicon substrate, respectively.*

Substrate	Modified JMAK model		Directly	
	ΔH_g (eV)	$\ln(U_0 /\mathrm{m\ s^{-1}})$	ΔH_g (eV)	$\ln(U_0 /\mathrm{m\ s^{-1}})$
Glassy carbon	8.9 ± 0.9	30 ± 6	8.0 ± 2.0	23 ± 13
Silicon	4.0 ± 0.7	2.6 ± 1.8	3.9 ± 0.8	-0.11 ± 6

Fig. 6.21 shows the plots of the experimentally determined diffusion coefficients for the overall crystallisation process of amorphous $Si_{0.33}C_{0.67}$ films deposited on crystalline silicon substrate as a function of (1/T). Also plotted in the same figure are the diffusion coefficients obtained by the least squares fit to equation (6.3). It can be seen that the values are in the same order of magnitude proving the consistency of our method.

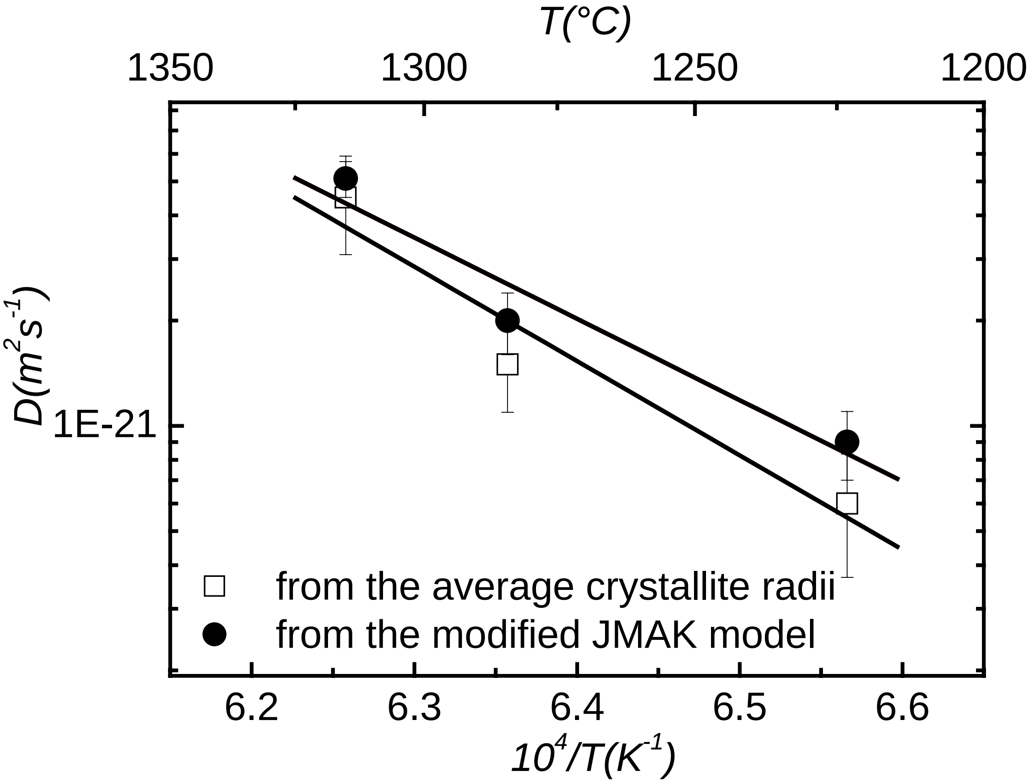

Fig. 6.21: *Amorphous* $Si_{0.33}C_{0.67}$ *films deposited on a silicon substrate: Arrhenius plots of the diffusion coefficients obtained from the average crystallite radius (squares) and the modified JMAK model according to equation (6.3) (full circles).*

The aim of the investigation of the crystallisation kinetics of $Si_{0.33}C_{0.67}$ films deposited on silicon substrate was the study of the influence of a carbon-rich matrix on the crystallisation. This result could be determinant to understand the reason of the high activation enthalpy in the case of glassy carbon substrate. However an activation enthalpy of 4.6 ± 0.3 eV was obtained. This activation enthalpy is similar within the estimate margin of error to that of the growth process in the crystallisation of SiC films deposited on silicon substrates. This implies that despite of the difference in the growth process (different JMAK exponents), the same energetic crystallisation process appears in the two systems. It must be concluded that most probably the nature of the substrate is the principal cause of the difference in the activation enthalpies.

In order to compare the rate of the kinetics for each system, rate constants were calculated using the formulas $k = \left(\frac{4}{3}\pi N_0\right)^{\frac{1}{3}} U$ for amorphous films deposited on silicon and glassy carbon substrates (interface-controlled crystallisation process) and $k = \left(\frac{4}{3}\pi N_0\right)^{\frac{2}{3}} D$ for the amorphous $Si_{0.33}C_{0.67}$ films deposited on a silicon substrate (diffusion-controlled crystallisation process). These values are given in Table 6.5. It comes out that the kinetics is slower for the crystallisation of $Si_{0.33}C_{0.67}$ occurring in a carbon-rich matrix.

Table 6.5: *Rate constants obtained from equation (6.2) and equation (6.3) for SiC films deposited on silicon and glassy carbon substrates and for amorphous* $Si_{0.33}C_{0.67}$ *films deposited on a silicon substrate.*

Annealing temperature (°C)	Rate constants k (10^{-6} s^{-1})		
	Amorphous SiC deposited on silicon substrate	Amorphous SiC deposited on glassy carbon substrate	Amorphous $Si_{0.33}C_{0.67}$ deposited on silicon substrate
1200	7.55 ± 2.4	-	-
1250	23.8 ± 8.0	-	1.9 ± 0.5
1275	35.7 ± 10.0	-	-
1300	47.7 ± 16.0	-	3.9 ± 0.6
1325	-	-	9.8 ± 1.0
1350	160 ± 60	-	-
1500	-	27.5 ± 7.0	-
1525	-	79.0 ± 14.0	-
1550	-	94.0 ± 30.0	-
1575	-	375.0 ± 100.0	-
1600	-	600.0 ± 200.0	-

6.2 Precipitation of transition metal diboride-based materials

6.2.1 Precipitated phases

The nominal compositions of the samples investigated in this part can be found in Table 5.1. After annealing at temperatures between 1400 °C and 1700 °C the transition metal diboride solid solutions show a secondary phase with W_2B_5 structure, which precipitates with a platelet-like morphology. These microstructures depend on the preparation, the chemical composition and the thermal treatment. XRD diagrams of the samples belonging to the group B show after the homogenisation XRD peaks characteristic of the phase (Ti, W, Cr)B_2 of AlB_2-type, which correspond closely to the characteristic diffraction peaks of the TiB_2 structure (Fig. 6.22, Fig. 6.23). These observations are confirmed by the SEM image which presents a homogeneous TiB_2-rich matrix (grey), the dark regions being pores (Fig. 6.24). It must be noted that for some samples traces of ß-WB precipitates have been detected.

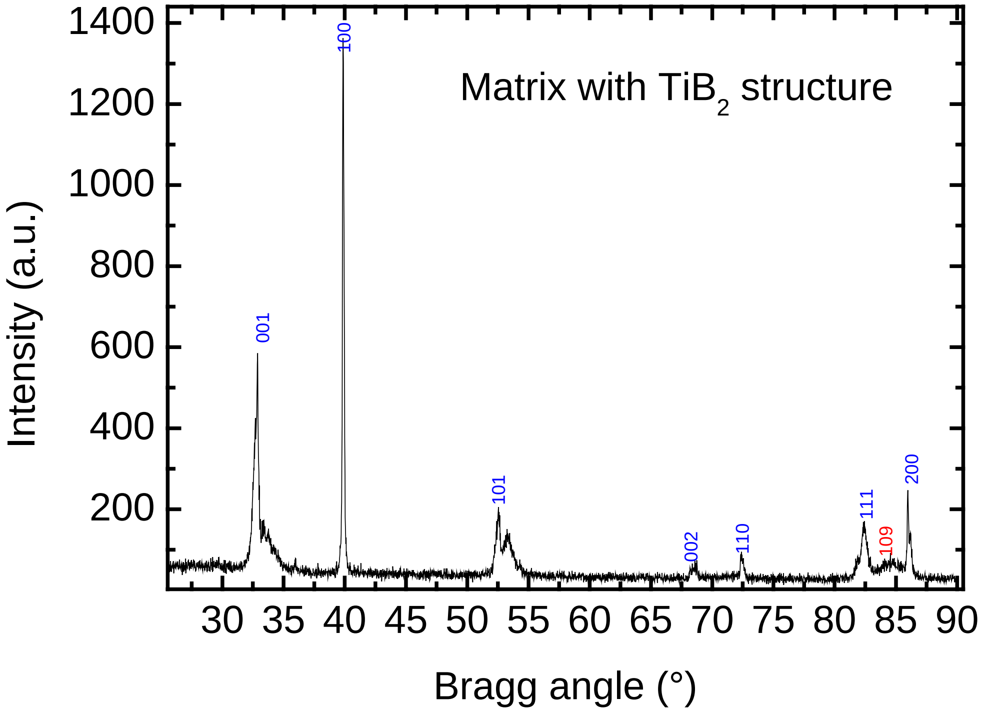

Fig. 6.22: XRD patterns of the as-homogenised sample B451. Only Bragg peaks corresponding to the TiB_2 structure are observed.

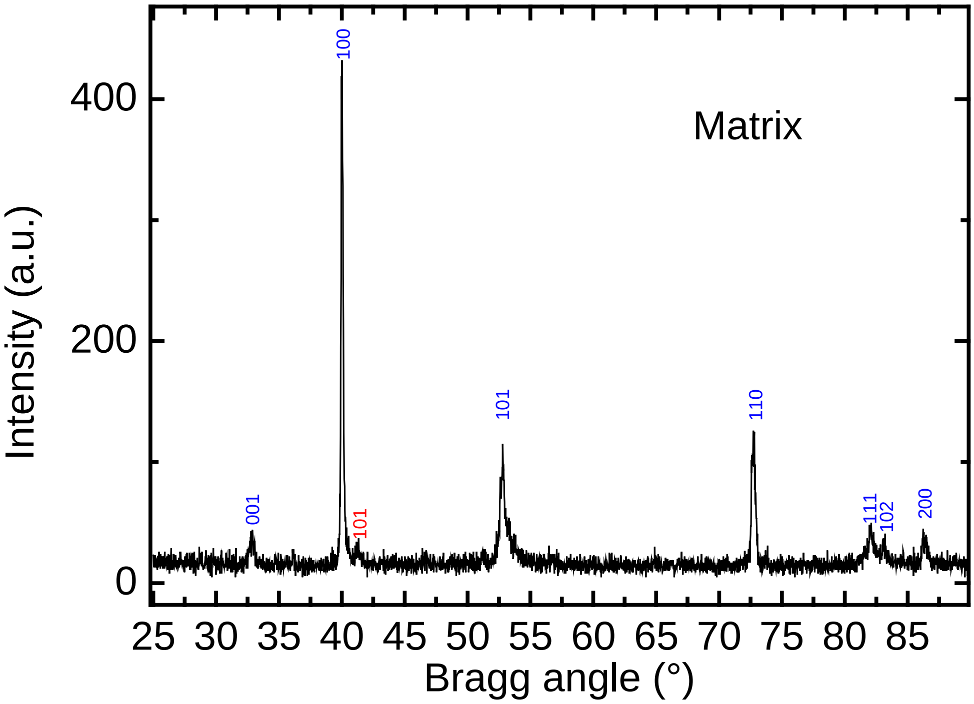

Fig. 6.23: *XRD patterns of the as-homogenised sample B352. Only Bragg peaks corresponding to the* TiB_2 *structure are detected.*

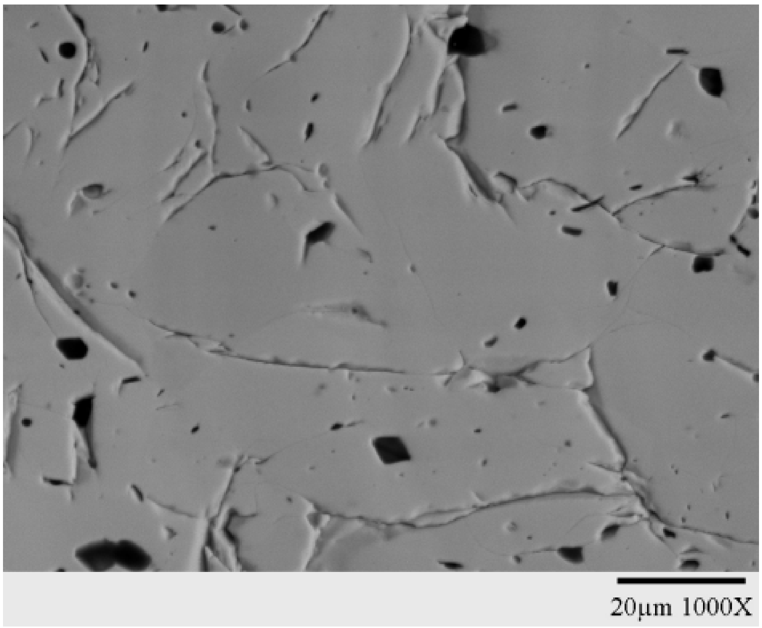

Fig. 6.24: *SEM micrograph of the as-homogenised sample B451. Dark regions are pores within the* TiB_2*-rich matrix (grey).*

For all investigated samples and independently of the preparation method the precipitated phase with W_2B_5 structure was detected. After annealing the XRD diffraction diagram exhibited new characteristic peaks that correspond closely to the W_2B_5 structure (Fig. 6.25). The peaks with significant intensities are consistent with the (00l) planes with the strongest (004) reflection locates at 2θ = 29.92 °. This line is used for monitoring the precipitation process as a function of annealing time as explained in 5.3.1. These observations indicate the presence of a texture during the precipitation process. It can be also concluded that the particles with W_2B_5 structure precipitated and grew parallel to the basal plane of the TiB_2 crystal. The SEM image (Fig. 6.26) shows the precipitated phase with W_2B_5 structure (white) with platelet-shape and elongated forms within the host TiB_2 matrix (grey). The dark regions represent pores within the matrix. The comparison of the backscattering images of milled and not-milled samples leads to the conclusion that, although the precipitated particles are identical with respect to their shapes, samples which were not milled present a low density of precipitates and also regions without precipitates (Fig. 6.26 and Fig. 6.27). The kinetics of this type of precipitation constitutes the central objective of our investigations.

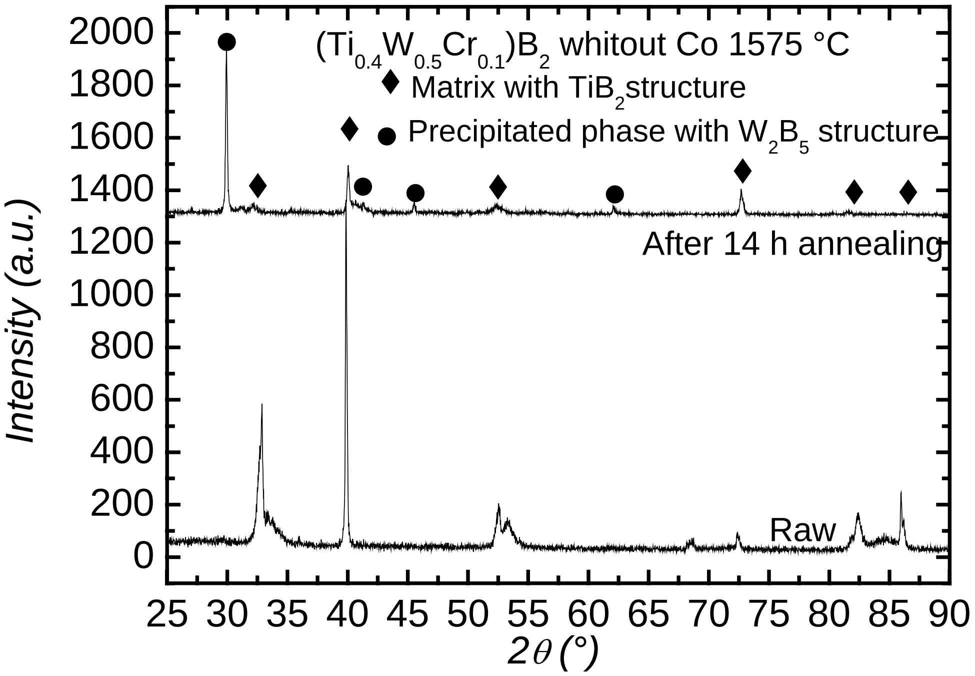

Fig. 6.25: *XRD patterns of the sample B451 after 14 hours annealing at 1575 °C. New peaks corresponding to the precipitated phase with W_2B_5 structure are detected.*

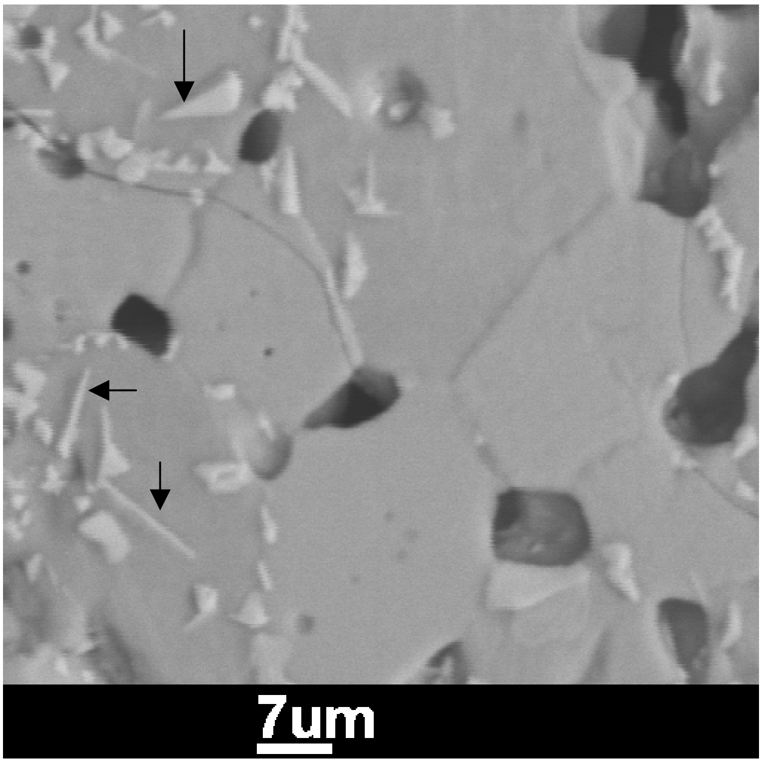

Fig. 6.26: *SEM image of B451 after complete precipitation. Arrows indicate elongated precipitates (white) within the* TiB_2*-rich matrix (grew). Dark regions are pores.*

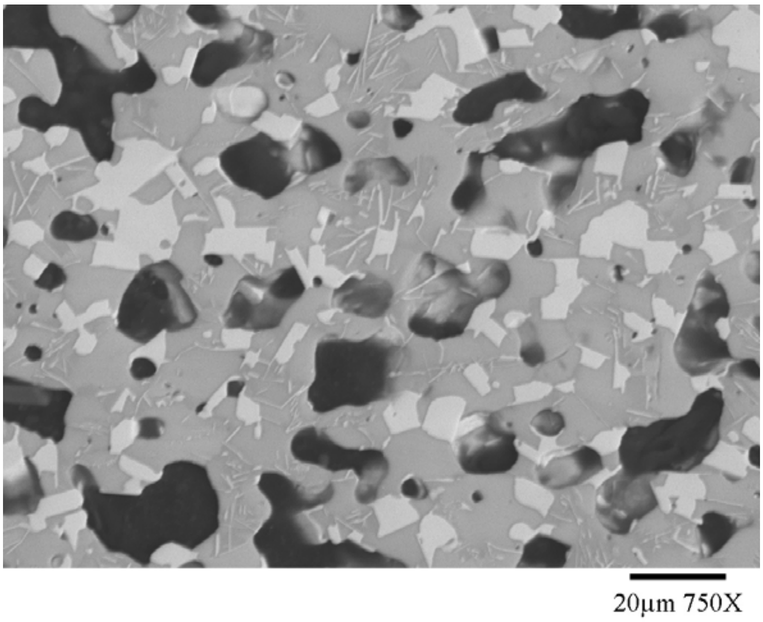

Fig. 6.27: *SEM image of A352 annealed at 1450 °C for 22 hours after complete precipitation. High densities of elongated and platelet-like precipitates are observed.*

6.2.2 Nucleation at grain boundaries

Fig. 6.28 shows the initial stage of the precipitation process of the sample B451 after annealing. The grain boundaries and small precipitated particles can be recognised simultaneously. It must be noted that some precipitates are formed directly in the bulk of the grains. The same situation is observed with A352 samples (Fig. 6.29). These observations suggest that the nucleation of the precipitates in the diboride-based materials can be heterogeneous. Moreover it can be concluded that the grain boundaries play an important role for the nucleation of the particles during the precipitation from the diboride solid solutions. Analysis on the $(Ti,W)B_2$ system reported that boron atoms are preferentially transferred from a titanium environment to a tungsten neighbourhood during thermal treatment [Mit98]. This transfer is enabled by the high mobility of boron and leads to a reaction between boron and tungsten, which forms WB at grain boundaries. The ß-WB can only be stabilised within a distinguished quasi-ternary composition range. If the ß-WB is not stabilised the following process can occur: free boron can react with WB to form W_2B_5. This reaction is well known from the literature [Bre55] and provides a fine microstructure of W_2B_5 in the case of the quasi-ternary TiB_2-CrB_2-WB_2 system.

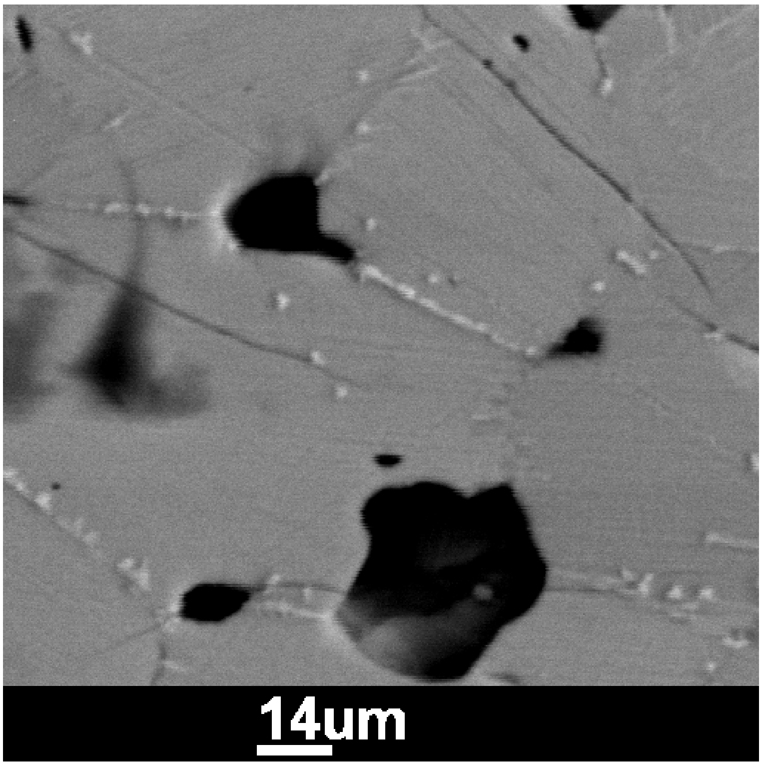

Fig. 6.28: *Precipitation at grain boundaries in the sample B451 annealed at 1500 °C for 1 hour.*

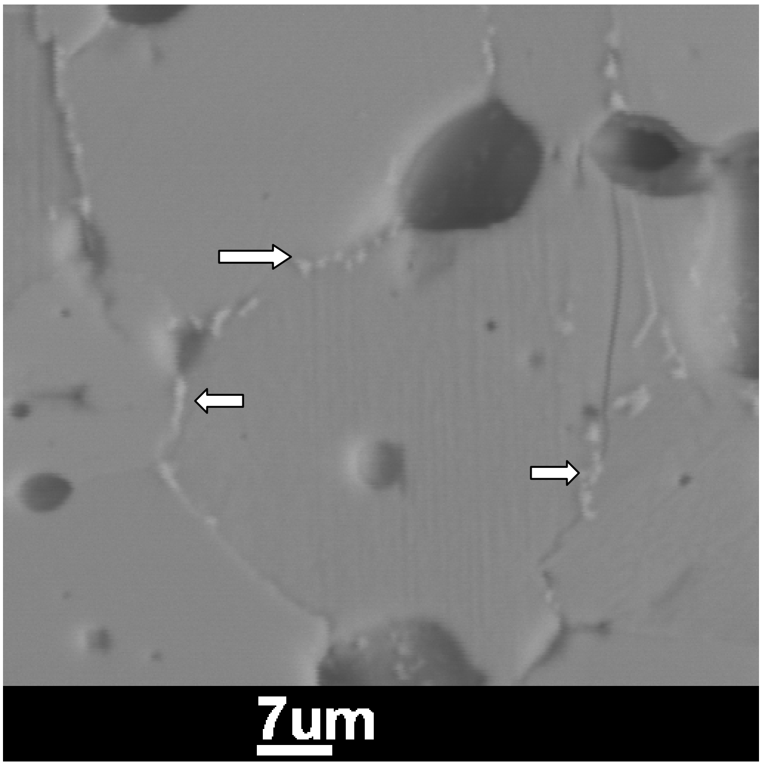

Fig. 6.29: *Precipitation at grain boundaries (arrows) in the sample B352 annealed at 1475 °C for 7 hours.*

6.2.3 Variation of the concentration of the matrix

EDX measurements (Table 6.6, Table 6.7 and Table 6.8) reveal that samples B352 and B451 (not milled) exhibit tungsten rich-precipitates with a chemical composition of $(W_{0.8}Ti_{0.1}Cr_{0.1})B_2$. The concentration of the matrix remained approximately constant throughout the thermal treatment. For the samples A352 (milled) the precipitated phase presents a composition of $(W_{0.92}Ti_{0.03}Cr_{0.05})B_2$. The matrix concentration remains also unchanged at $(Ti_{0.3}W_{0.5}Cr_{0.2})B_2$. A small amount of Co coming from the preparation of the samples A352 was also detected. On the SEM image of a sample containing Co (Fig. 6.30) a high density of precipitates in contrast to the sample without Co (Fig. 6.31) was observed. Therefore, the high density can be considered as a consequence of the presence of Co in the matrix, which acts as a favoured site for heterogeneous nucleation.

The line scan EDX measurements Fig. 6.32 of a single particle in the sample B352 exhibits clearly the variation in the chemical composition due to the presence of the precipitated particle. However, from these observations, a soft impingement, in the phase separation process cannot be assumed, due to the large distance between precipitates and the constancy of the matrix concentration.

Table 6.6: *EDX analyses of the sample A352 annealed at 1450 °C for 22 hours.*

Time	Sample A352 (1450°C)							
	Matrix (concentration in at. %)				Precipitate (concentration in at. %)			
	W	Ti	Cr	Co	W	Ti	Cr	Co
22h	49.28	29.33	20.59	0.97	96.46	0	1.98	1.57
					95.42	0.22	3.88	0.47
					82,59	9.84	6.9	0.67

Table 6.7: *EDX analysis of the sample B352 annealed at 1575 °C for different annealing times.*

Time	Sample B352 (1575 °C)							
	Matrix (concentration in at. %)				Precipitate (concentration in at. %)			
	W	Ti	Cr	Co	W	Ti	Cr	Co
1h	55.52	29.3	15.52	-	61.73	25.77	12.50	-
2h	48.78	33.79	17.43	-	74.29	15.62	10.09	-
5h	50.4	32.37	17.23	-	78.52	12.02	9.45	-
14h	52.77	30.55	16.68	-	-	-	-	-

Table 6.8: *EDX analysis of the sample B352 annealed at 1500 °C for different annealing times.*

Time	Sample B352 (1500°C)							
	Matrix (concentration in at%)				Precipitate (concentration in at%)			
	W	Ti	Cr	Co	W	Ti	Cr	Co
1h	53.31	28.98	17.71	-	95.71	0	4.29	-
2h	49.8	31.3	18.89	-	-	-	-	-
4h	51.97	29.01	19.03	-	77.33	12.37	10.3	-
7h	50.56	31.92	17.72	-	76.06	14.04	9.88	-
11h	53.56	28.64	17.8	-	78.93	12.34	8.73	-
16h	59.42	25.80	14.79	-	73.69	16.5	9.821	-

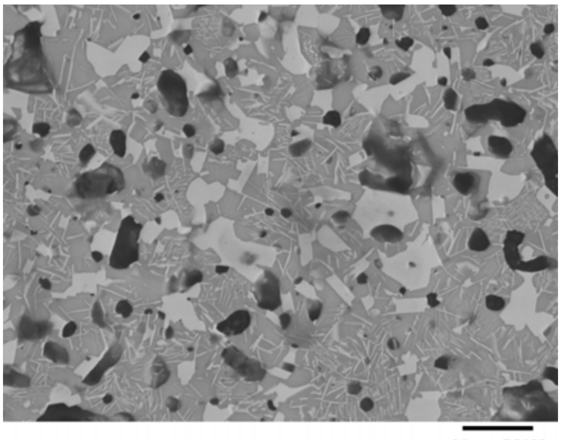

Fig. 6.30: *SEM image of a fully precipitated sample A352 (containing cobalt). Higher density of precipitates.*

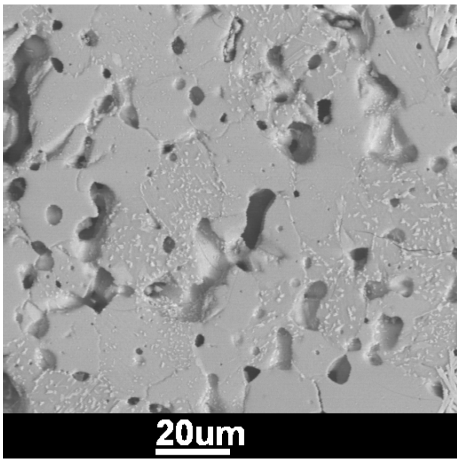

Fig. 6.31: *SEM image of a fully precipitated sample B352 (without cobalt). lower density of precipitates.*

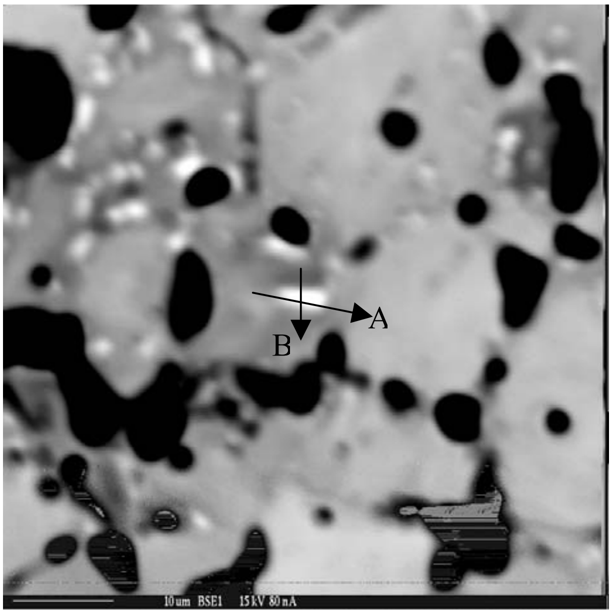

Fig. 6.32: *Line scan EDX of a precipitate*

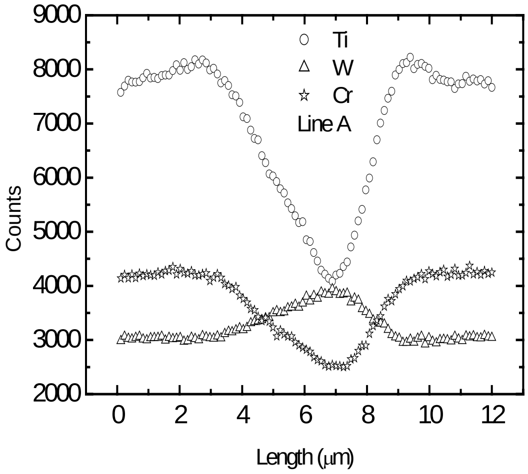

Fig. 6.32a: *Variation of the concentration along the direction A.*

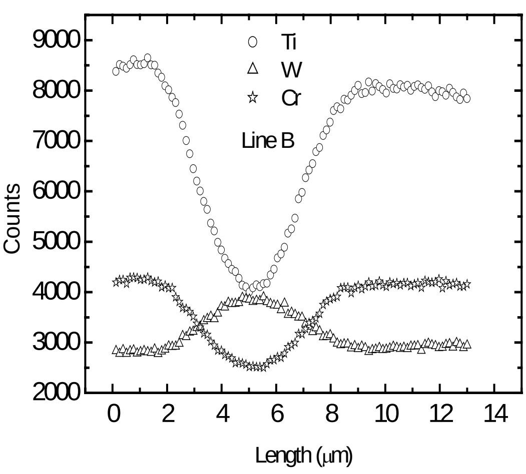

Fig. 6.32b: *Variation of the concentration along the direction B.*

6.2.4 Lattice parameters

In order to determine the lattices parameters of the matrix as well as those of the precipitated phase, the computer software Pcw was used. With this method the complete XRD diagram can be refined and some important information such as lattice parameters of the precipitated phase can be directly achieved.

The refinement procedure can be summarised as follows:

- Phases chosen are (Ti, W, Cr)B_2 with AlB_2 structure and (W, Ti, Cr)B_2 with W_2B_5 structure.
- Initial conditions are determined by introducing the initial and the final chemical composition of the matrix and the precipitates. The values obtained from the EDX measurements were used.
- As a fit function, the pseudo-Voigt function (combination of two Lorentz functions [Kra96]) is chosen.
- The (001) planes is taken as preferred orientation for the precipitated phase.

The lattices parameters calculated with the present method are given in Table 6.9 and Table 6.10. A small decrease of a_{TiB2} and an increase of c_{TiB2} from the raw materials to the precipitated samples due to the appearance of the new phase is observed. But the determined parameters after thermal annealing prove that there are neither changes in the structure of the matrix nor of the precipitated phase during the crystallisation process. The calculated values are in agreement with those available in the literature [Mit98].

Table 6.9: *Lattice constants of the matrix and the precipitated phase of the sample B352 after complete precipitation. Also given are the lattices constants of the as-homogenised matrix.*

Temperature (°C)		1400	1500	1550	As-homgenised sample
Matrix	a (Å)	3.0079 ± 0.005	3.0110 ± 0.005	3.0123 ± 0.005	3.0204± 0.005
	c (Å)	3.2133 ± 0.005	3.2093 ± 0.005	3.2087 ± 0.005	3.1606 ± 0.005
Precipitate phase	a (Å)	2.9793 ± 0.005	3.9814 ± 0.005	2.9819 ± 0.005	-
	c (Å)	13.8464 ± 0.005	13.8580 ± 0.005	13.8639 ± 0.005	-

Table 6.10: *Lattice constants in the matrix and precipitated phase of the sample B451 after complete precipitation. Also given are the lattices constants of the as-homogenised matrix.*

Temperature (°C)		1500	1550	1575	As-homogenised sample
Matrix	a (Å)	3.0158 ± 0.005	3.0174 ± 0.005	3.019 ± 0.005	3.033 ± 0.005
	c (Å)	3.2142 ± 0.005	3.21867 ± 0.005	3.2126 ± 0.005	3.1782 ± 0.005
Precipitated phase	a (Å)	2.9840 ± 0.005	2.9828 ± 0.005	2.985 ± 0.005	-
	c (Å)	13.8540 ± 0.005	13.8708 ± 0.005	13.865 ± 0.005	-

6.2.5 Surface precipitation

Nucleation can occur homogeneously or heterogeneously. Homogeneous nucleation is random nucleation without preferential sites in a homogeneous material. Heterogeneous nucleation occurs at preferred sites, such as surfaces, grain boundaries, second-phase particles, etc. Normally, heterogeneous nucleation is dominant, because there are always defects and impurities present in materials. Nucleation and crystal growth can occur within the bulk or at the surface, referred to as bulk crystallization and surface crystallization, respectively. Experiments were done to check whether surface nucleation is present for the diborides. The following procedure was used: a sample of each group (A352 and B352) was thermally annealed to full precipitation and then observed with SEM. These samples were carefully polished. In a step-by-step process some micrometers of the sample surface were removed using diamond paste. Then the surface was again observed, etc. This process resulted to a progressive decrease of the number of precipitated particles in the near-surface layer of the sample B352. After the removal of about 10 µm, practically no more precipitates could be detected, and the matrix was identical to that of an unannealed sample (Fig. 6.33). This behaviour is confirmed by the XRD pattern of the initial and the polished sample, where the decrease of the intensity of W_2B_5 diffractions is clearly observed (Fig.6.34). In contrast, for the sample A352 a different tendency is observed. In fact, the density of the particles remained more or less unchanged during the removal of the near-surface layer so that almost no difference between the initial and the polished sample is detected (Fig 6.35). A comparison of the XRD diagrams confirms these observations (Fig. 6.36).

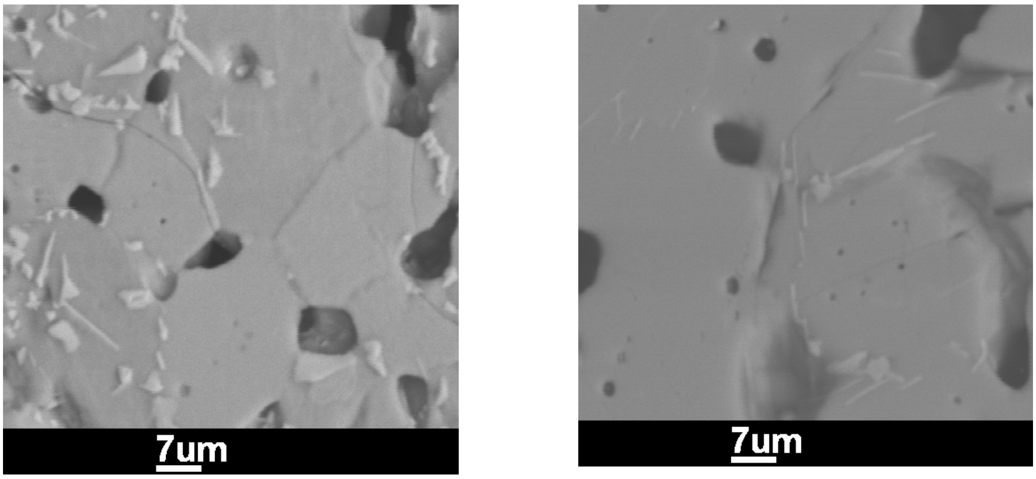

Fig. 6.33: *SEM micrographs of the sample B352 annealed at 1575 °C for 14 hours before (left) and after (right) the polishing. A complete disappearance of the precipitates can be seen.*

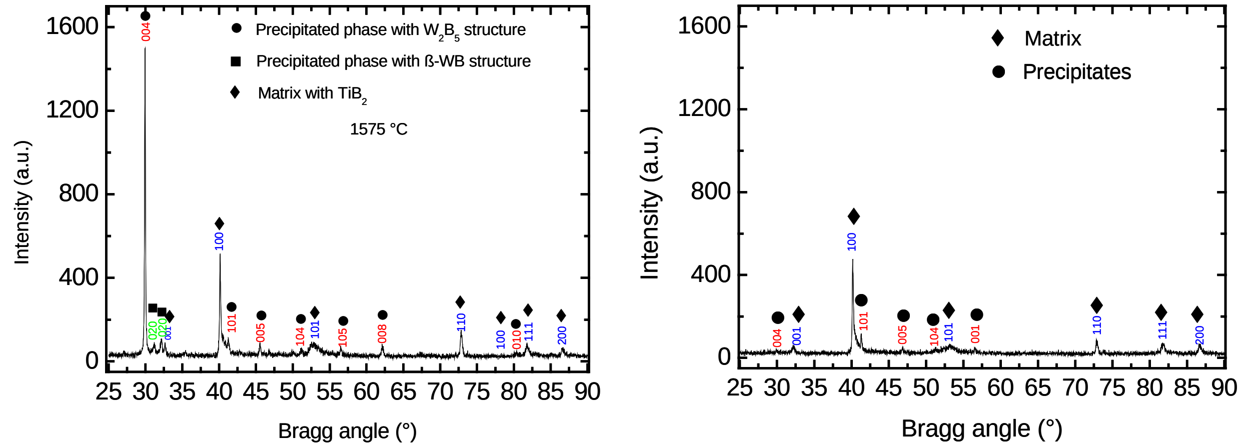

Fig. 6.34: *XRD diffraction patterns of the sample B352 annealed at 1575 °C for 14 hours before (left) and after (right) the removal of the near-surface layer.*

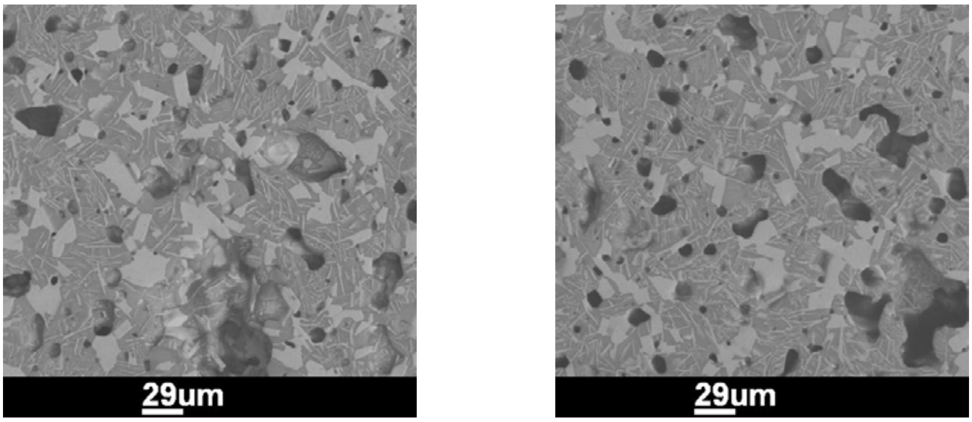

Fig. 6.35: *SEM micrographs of the sample A352 annealed at 1450 °C for 22 hours before (left) and after (right) the removal of near-surface layer. The precipitated matrix remains unchanged.*

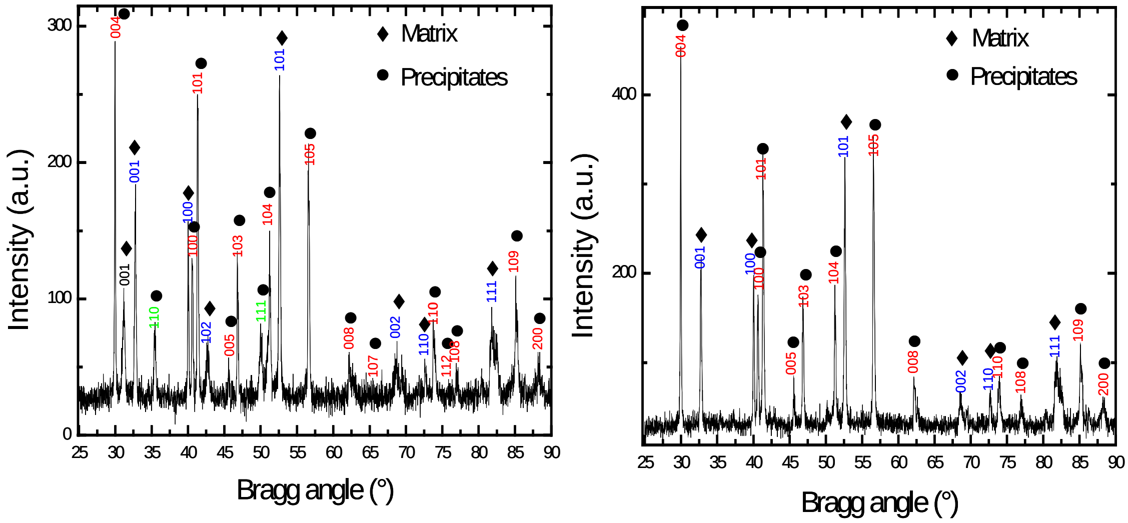

Fig. 6.36: *XRD diffraction of the sample A352 annealed at 1450 °C for 22 hours before (left) and after (right) the removal of the near-surface layer.*

6.2.6 Size of the precipitates

An important feature of the microstructure is the size of the precipitated particles because it can be determinant for the dimensionality of the growth. The diameter of most precipitated particles ranged between 1 μm and 15 μm with a constant thickness of 1 μm. The SEM micrographs show that the formation of platelet-like precipitates with a high aspect ratio begins in the earlier stage of the process at grain boundaries followed by a continuous growth in the volume (Fig. 6.37). Besides the particles formed at the grain boundaries, less than 10 % of particles emerge simultaneously from the bulk. The observed platelet-shape precipitates indicate clearly a two-dimensional growth.

For a better understanding of the precipitation mechanisms, diffusion coefficients were also calculated from the measurements of the particle size as a function of annealing time in the high-density regions using an image analysis software (ANALYSIS 5.0). The particle size is measured in the direction of the growth as shown in Fig. 6.37 at different times. Examples at different temperatures are shown in Fig. 6.50, where d^2 is plotted against annealing time. Diffusion controlled growth is expected in the present ceramics, because long range rearrangement process of atoms in the matrix are necessary in order to form W_2B_5 precipitates. The obtained time-dependent particle sizes (Fig. 6.50) are fitted by equation 6.10 from which the diffusion coefficients are achieved (Table 6.11). The diffusion coefficients obtained here are higher by about two orders of magnitude than the tracer diffusivities of ^{49}Ti in a similar system [Sch03]. We attribute this difference to the fact that crystallite growth is governed by inter-diffusion of the constituents and not by tracer diffusion of a single element. Moreover the measurements using the tracers were made in a completely precipitated matrix and the inter-diffusion was not taken into account.

Table 6.11: *Diffusion coefficients of samples B352 and B451 at different temperatures as obtained from the time dependence of the radius of the precipitate.*

Temperature (°C)	$(Ti_{0.3}W_{0.5}Cr_{0.2})B_2$	$(Ti_{0.4}W_{0.5}Cr_{0.1})B_2$
	D_V (m^2s^{-1})	D_V (m^2s^{-1})
1475	$(2.4 \pm 1.2) \times 10^{-15}$	-
1500	$(3.8 \pm 1.4) \times 10^{-15}$	$(1.2 \pm 0.8) \times 10^{-15}$
1525		
1575	$(9.0 \pm 2.5) \times 10^{-15}$	$(7.4 \pm 3.7) \times 10^{-15}$
1650	$(2.0 \pm 0.7) \times 10^{-14}$	$(1.0 \pm 0.5) \times 10^{-14}$

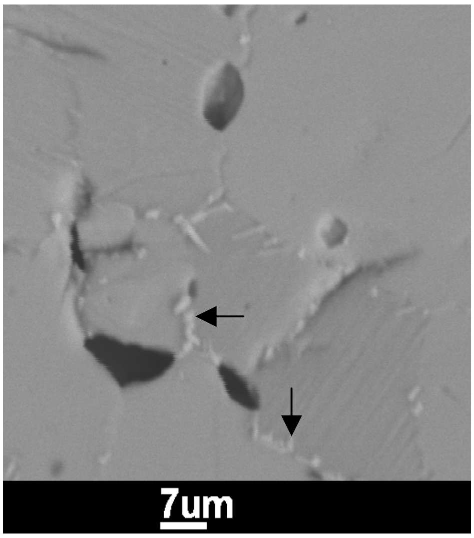

Fig. 6.37a: *Sample B451 annealed at 1575 °C for 1 hour: nucleation at grain boundaries.*

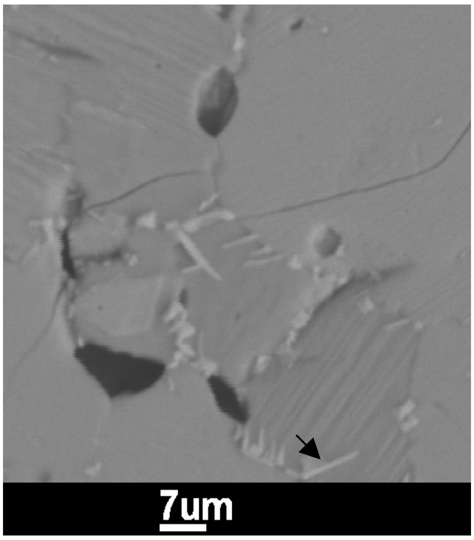

Fig. 6.37b: *Sample B451 annealed at 1575 °C for 4 hours: growth in the volume.*

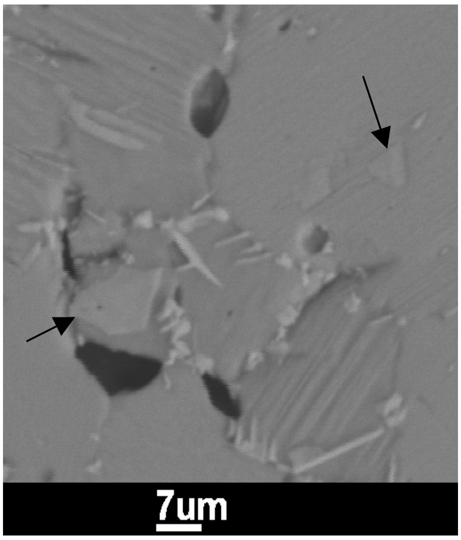

Fig. 6.37c: *Sample B451 annealed at 1575 °C for 9 hours: growth in the volume*

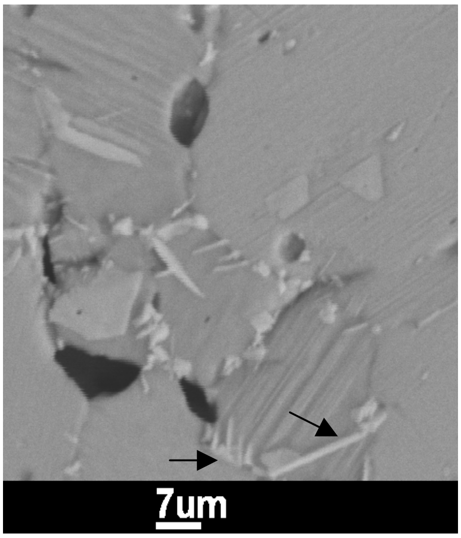

Fig. 6.37d: *Sample B451 annealed at 1575 °C for 14 hours: growth and impingement of all nucleated particles.*

6.3 Numerical simulation

The precipitation parameters were determined using the classical JMAK theory followed by a modified model, which takes into account the contribution of grain boundaries.

6.3.1 Modelling of two-dimensional heterogeneous precipitation

The description of the precipitation process is based on the classical JMAK theory with the extension to heterogeneous nucleation in planar regions first derived by Cahn [Cah56], [Cah57]. The classical JMAK theory was proved to be identical with the Boolean model developed in the framework of stochastic geometry [Sto95]. In terms of this model, the transformed volume fraction is given by $X(t) = \exp[-a(t)V(t)]$, where *a(t)* is the integral of the nucleation rate over the time and *V(t)* is the mean volume of all particles existing at time *t* including those which formally overlapped. The entire volume fraction of precipitated regions can be considered as the ensemble of transformed regions created by all processes, which are active. In terms of the Boolean model, the corresponding volume fraction is given by $X(t) = \exp[-a_1(t)V_1(t) + a_2(t)V_2(t) + ...]$, where $i = 1, 2, 3,....$ denote the processes 1, 2, 3,….. This expression is used in the present approach.

As observed from the SEM micrographs, the nucleation of crystalline precipitates may occur in principle in the grain volume and at grain boundaries. In order to ensure that heterogeneous nucleation takes place it is important to have $\rho_B I_B >> I_V$, where ρ_B is the boundary density, I_B and I_V are the nucleation rate in the grain boundaries and in the volume, respectively. In other words, as soon as this condition does not hold, the volume contribution is dominant and the precipitation process can be directly described with sufficient accuracy by the classical JMAK theory.

It has been shown before that nucleation of the particles takes place mainly at grain boundaries. It is now important to discuss the influence of these grain boundaries on the growth of the nucleated particles. Generally, diffusion in grain boundaries is faster than diffusion in the volume. The available amount of atoms in grain boundaries depends on the distance between two nucleated particles at the grain boundary. If this distance is large enough, the quantity of atoms contributing to the growth is also large and the diffusion at the grain boundary will be determinant. But due to the increase of the radius of the nuclei this distance is reduced leading to a decrease of the available reservoir in the grain boundary. Consequently the grain boundary diffusion is stopped if transfer of atoms from the adjacent grains to the grain boundaries is negligible. The SEM observations show that the distance between two nucleated particles at the earlier stage of the precipitation is less than one micrometer (Fig. 6.37). Let us consider a volume element of a grain boundary between four neighbouring nucleated precipitates, corresponding to the volume drained by the growing particle (Fig. 6.38). Assuming that the width of the grain boundaries is about 1 Å, the catchment volume can be calculated to be 10^{-22} m^3. Considering the sample B352, the molar mass of the matrix is $M_M = 46.1$ gmol^{-1} Taking a density of 5.7x 10^6 gm^{-3} [Mit98], the number of atoms per unit volume contained in the material can be determined to be 7.4 x 10^{28} m^{-3} therefore, the number of atoms contained in the catchment volume is 7.4 x 10^6. However the matrix has 0.5 at. % of WB_2, which corresponds to 3.6 x 10^6 atoms. After complete precipitation, the molar mass of WB_2 contained in the precipitate is $M_P = 68.5$ gmol^{-1} corresponding to a number of atoms per unit volume of 5.0 x 10^{28} m^{-3} and leading to a volume of 7.25 x 10^{-23} m^3. Assuming that this precipitate has a spherical shape at the earlier stage of the process, a particle radius of about 26 nm is calculated. This radius is negligible compared to the whole average size of the particle after full precipitation. This result suggests that, if there is a contribution of the grain boundaries, this contribution is limited to the earlier stage of the growth process after nucleation. Therefore, the amount of atoms contained in this reservoir and diffusing through the boundary is not sufficient to sustain the whole growth process. A particle radius of 26 nm is much too small to be observed with SEM and consequently also not accounted for during further analysis.

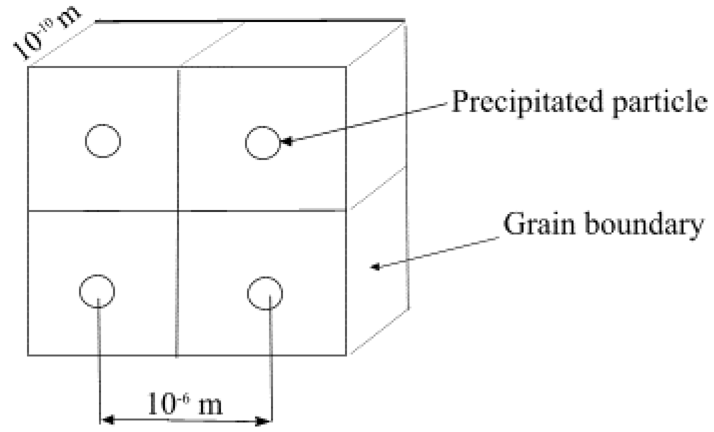

Fig. 6.38: *Illustration of the formation of the precipitates at a grain boundary plane in the earlier stage of the precipitation process. Each cube corresponds to a catchment volume in the grain boundary.*

As a result from these considerations, it can be concluded that diffusion in grain boundaries does not significantly contribute to the observed growth process. For the nucleated particles to grow to larger radii transport through the grain volume is necessary, which becomes the rate limiting process.

In order to model this process in a simpler way, a transition from the rectangular to the polar coordinate system has to be made so that a cylinder of radius *R(t)* with a constant thickness of *h* is used (Fig. 6.39). To conserve the two-dimensional growth the assumption R(t) >> h is made.

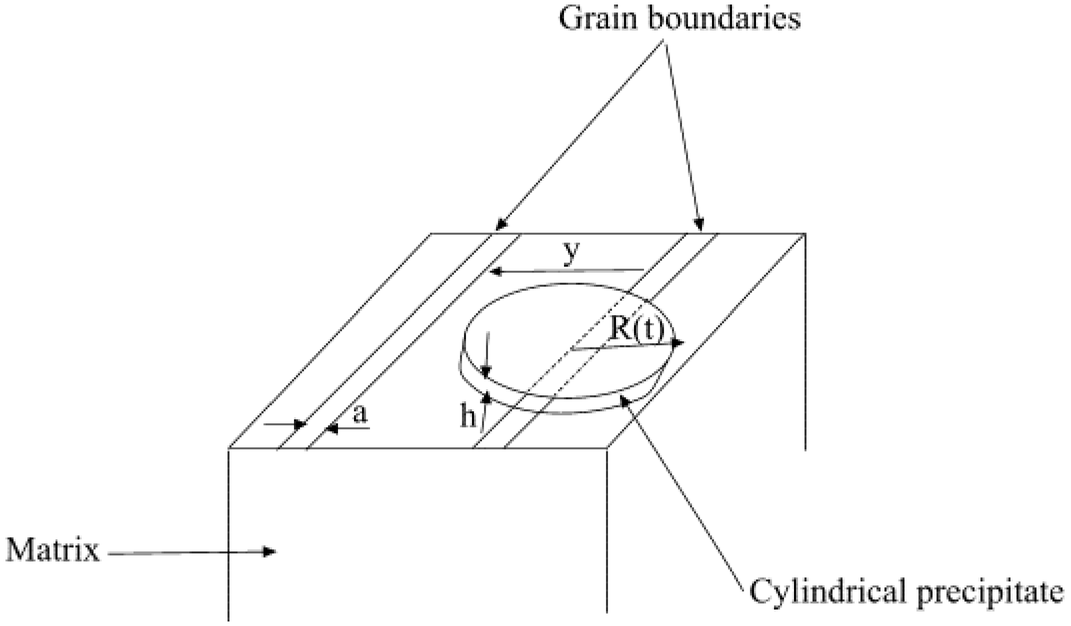

Fig. 6.39: *Schematic representation of a precipitate nucleated at the grain boundary and growing within the bulk. a, y, R(t), h are the width of the grain boundary, the distance between two parallel boundaries, the time dependent radius of the precipitate and the thickness of the precipitate, respectively. During the precipitation process, the thickness remains constant while only the radius increases.*

Considering a disc-like precipitate of radius R(t) growing because of bulk diffusion and under the assumption that the growth is essentially radial ($J_V = J_V(R)$), the total stationary flux of atoms to this precipitate from the bulk can be given by

$$J_V(R) = -D_V \frac{C_s - C_m}{R}, \tag{6.6}$$

where D_V is the diffusion coefficient of the slowest diffusing atoms in the volume and C_m and C_s are the mean atom concentrations of the diffusing element in the matrix and at the precipitate-matrix interface, respectively.

The integral flux to the cylindrical precipitate with constant thickness is defined by

$$J(R) = 2\pi h R J_V \tag{6.7}$$

The law of mass conservation, i.e. the balance between the flux of atoms from the bulk into the precipitate and the flux of atoms from the precipitate into the volume per unit time, gives the path equation of the growing precipitate due to diffusion.

$$J(R) = (C_P - C_s)\, 2\pi h R \frac{dR}{dt} \tag{6.8}$$

where C_p is the concentration of the equilibrium components in the precipitate (illustrated in Fig. 6.40). Combining equations (6.7)-(6.8) the expression for the precipitate growth is given by [Pra98]

$$\frac{dR}{dt} = \left(\frac{D_V}{R}\right)\frac{C_m - C_s}{C_P - C_s} \tag{6.9}$$

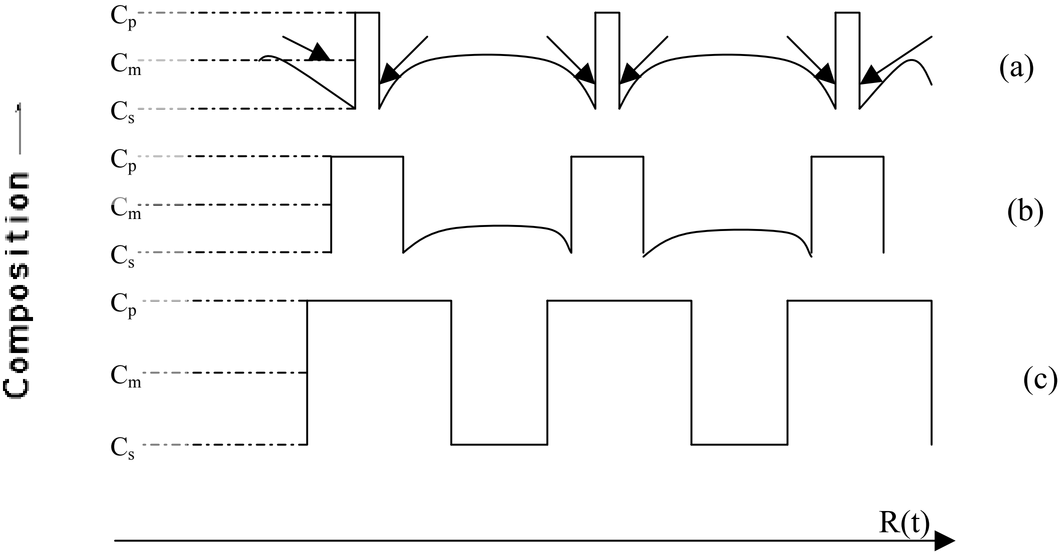

Fig. 6.40: *Sketch of the evolution of the concentration of the between the precipitate and the matrix as the transformation proceeds. (a) Transient growth process. (b) Diffusion controlled growth under steady state condition. (c) End of the transformation [Pra98].*

As initial condition for equation (6.9), we assume that the initial size of the precipitate in grain boundaries is approximately zero ($R(\tau) = 0$), where τ is the incubation time of nucleation. The solution of equation (6.9) leads to the following expression for the time dependence of the radius of the precipitate nucleated at the moment τ

$$R^2(t,\tau) = \alpha(t - \tau) \tag{6.10}$$

with

$$\alpha = \frac{2D_V(C_m - C_s)}{C_P - C_s} \tag{6.11}$$

The ratio $\gamma = \frac{C_m - C_s}{C_p - C_s}$ is considered as the average value of the precipitated fraction at the end of the process [Pra98] and has an approximate value of 0.3 obtained from XRD measurements. Equation (6.10) becomes

$$R^2(t,\tau) = 2\gamma D_V (t-\tau) \tag{6.12}$$

that is used in paragraph (6.2.6) to fit the experimental time dependence of the size of the growing particles.

The EDX measurements show that the concentration in the matrix remains approximately unchanged before and after the thermal annealing. The chemical composition of the precipitate is $(W_{0.8}Ti_{0.15}Cr_{0.05})B_2$ (Table 6.7 and Table 6.8). This leads to values of C_s equal to 5 at. %, 52 at. % and to 42 at. % for tungsten, titanium and chromium, respectively. The difference C_m-C_s is positive for tungsten and negative for titanium and chromium. The precipitate growth process can be visualised in the following way: tungsten atoms diffuse along the gradient of the chemical potential from the matrix to the precipitate, where they are incorporated and those of titanium and chromium diffuse away from the precipitate to the matrix.

This part of the modelling consists of the determination of the precipitated fraction in the grain boundary as well as in the volume. The expression of the transformed volume fraction can be given using the JMAK approach and by taking into account the contribution of the grain boundary. Considering the density of boundaries $\rho_B \sim 2/L_B$, (L_B being the average grain size) and the width of the grain boundary layer a, the total amount of the precipitated volume fraction can be given according to equation (6.3) as follows,

$$X(t) = 1 - \exp\left[-(1 - a\rho_B)Y_V(t) - \rho_B Y_B(t)\right], \tag{6.13}$$

where $Y_V(t)$ and $Y_B(t)$ are the extended volume fractions for precipitates nucleated in the bulk and at the grain boundary areas, respectively [Bak02].

The next step consists of finding the appropriated expressions for $Y_V(t)$ and $Y_B(t)$. The contribution of the nucleation and the growth in the volume, $Y_V(t)$, is given in terms of equation (4.13).

Concerning the grain boundary contribution, the concept of Cahn for the derivation of rate laws for transformations in which new phases nucleate at grain boundaries is used [Cah56]. Consider a cylindrical particle which nucleates at the moment τ on a plane boundary with a radius of $R(t,\tau)$ at time t. Consider a plane that is parallel to the given boundary and situated at a distance y from it. This plane intersects the nuclei with a radius $R(t, \tau) > y$. For the sake of simplicity, we suppose that the particles are perpendicular in the radial direction to the boundaries planes. Thus the obtained intersection area can be given by $2h\left(R^2(t,\tau)-y^2\right)^{\frac{1}{2}}$ and the total intersection area of all nuclei is obtained by integrating over τ [Bak02]:

$$Y_B^e(y,t) = 2N_{0B}h\left(R^2(t,0)-y^2\right)^{\frac{1}{2}} + 2h\int\limits_0^{t_m(y)} I_B(\tau)\left(R^2(t,\tau)-y^2\right)^{\frac{1}{2}} d\tau \qquad (6.14)$$

where N_{0B} is the density of embedded nuclei at t = 0, I_B is the nucleation rate in the boundary and $t_m(y)$ is defined by the equation

$$R(t,\, t_m) = y \qquad (6.15)$$

The set of all intersections represents a two dimensional Boolean model, i.e. the intersections are randomly distributed. Therefore the total contribution of the grain boundary can be given by

$$Y_B(y,t) = 1 - \exp\left[-Y_B^e(y,t)\right] \qquad (6.16)$$

The total contribution of the boundaries to the crystallized volume fraction is defined by the integration of equation (6.16) over all y [Bak02]:

$$Y_B(t) = 2\int\limits_0^{\infty} \left\{1 - \exp\left[-Y_B^e(y,t)\right]\right\} dy. \qquad (6.17)$$

To calculate the integral in equation (6.14) the variable τ is replaced in the following way. At fixed t, equation (6.10) describes a single–valued dependence of R(t, τ) on τ. Taking the partial differential of R(t, τ) on the left hand side of equation (6.10) and of τ on the right hand side of this equation, one can easily change the variable of integration τ → R'(t, τ) in equation (6.14) by

$$d\tau = -\frac{1}{\gamma D_V} R' dR' \qquad (6.18)$$

Now equation (6.17) can be rewritten as

$$Y_B(t) = 2\int_0^{R(t,0)} \left\{1 - \exp\left[-\pi Z\left(R(t,0), y\right)\right]\right\} dy \qquad (6.19)$$

where R(t, 0) is the maximum radius in the system at time t and the function Z(R,y) has the form:

$$Z(R,y) = 2N_{0B}h\left(R^2 - y^2\right)^{\frac{1}{2}} + \frac{2h}{\gamma D_V}\int\limits_R^y I_B\left(R'^2 - y^2\right)^{\frac{1}{2}} R' dR' \qquad (6.20)$$

6.3.1.1 Nucleation rate at grain boundaries

Fig 6.41a and Fig.6.41b show samples B352 and B451, respectively, after full precipitation at different temperatures. It can be seen that for both samples, most of the particles are formed at the grain boundaries and that almost no particles are formed within the grain interior after complete precipitation. These SEM experiments prove, that the platelet-like precipitates nucleate preferably at grain boundaries and grow into the interior of the matrix grain. Therefore, it can be concluded that the contribution of the volume to the precipitation process is negligible

Following the assumption of Kolmogorov on nucleation, the total number of the nuclei formed in the grain boundary with a constant nucleation rate I_B can be determined using the relation $N = V_0 I_B(T)\int_0^\infty (1 - X(T,t))dt$. This equation means that the nuclei are formed in the untransformed area only. For each value of the precipitation fraction, the integration is made at each annealing time. In order to obtain the total number of nuclei, integration over the whole annealing time has been made. It comes out that for 50 % precipitation almost 80 % of the precipitates are already nucleated (Fig. 6.42). As a good approximation, the nucleation rate at grain boundaries can therefore be considered as constant during the process.

Assuming that the nucleation rate does not depend on time, the integral in equation (6.20) can be expressed directly and the function Z(R,y) is given by

$$Z(R,y) = 2N_{0B}h\left(R^2 - y^2\right)^{\frac{1}{2}} + \frac{2hI_B}{3\gamma D_V}\left(R^2 - y^2\right)^{\frac{3}{2}} \qquad (6.21)$$

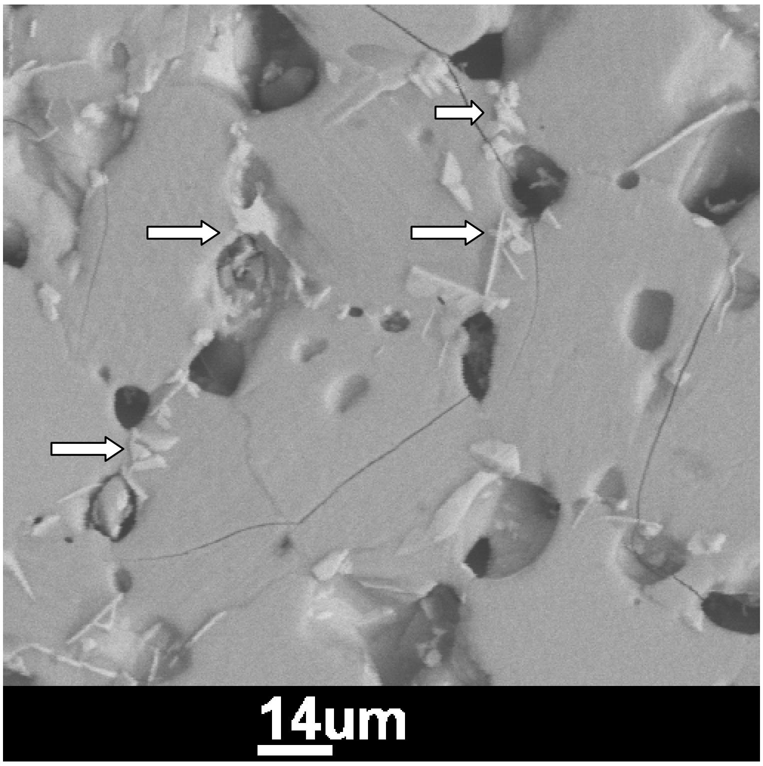

Fig. 6.41a: *SEM image of sample B352 annealed at 1700 °C for 4 hours. Particles nucleated at grain boundaries are indicated by an arrow. Dark regions are pores within the matrix.*

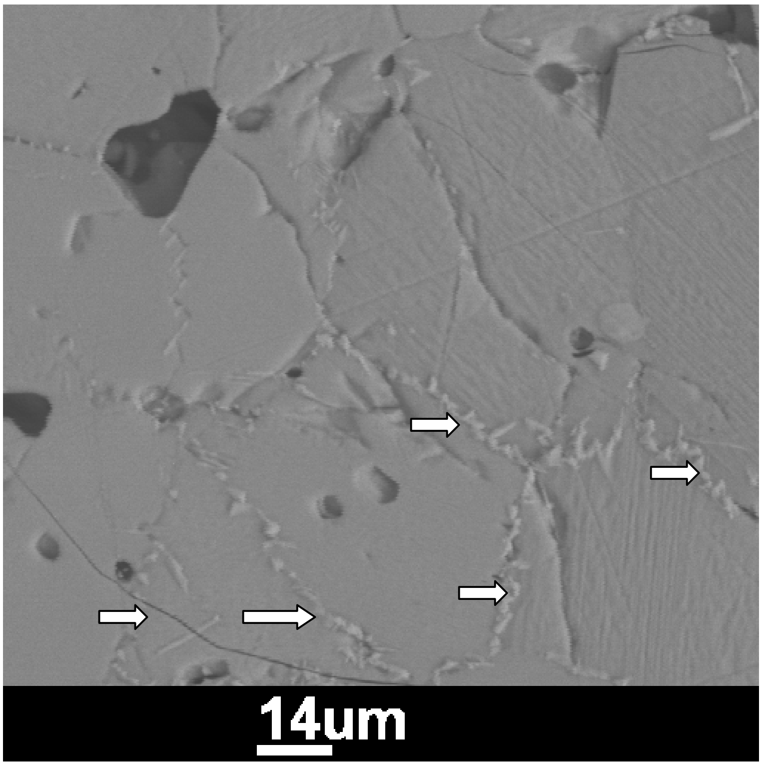

Fig. 6.41b: *SEM image of sample B451 annealed at 1500 °C for 20 hours. Particles nucleated at grain boundaries are indicated by an arrow. Dark regions are pores within the matrix.*

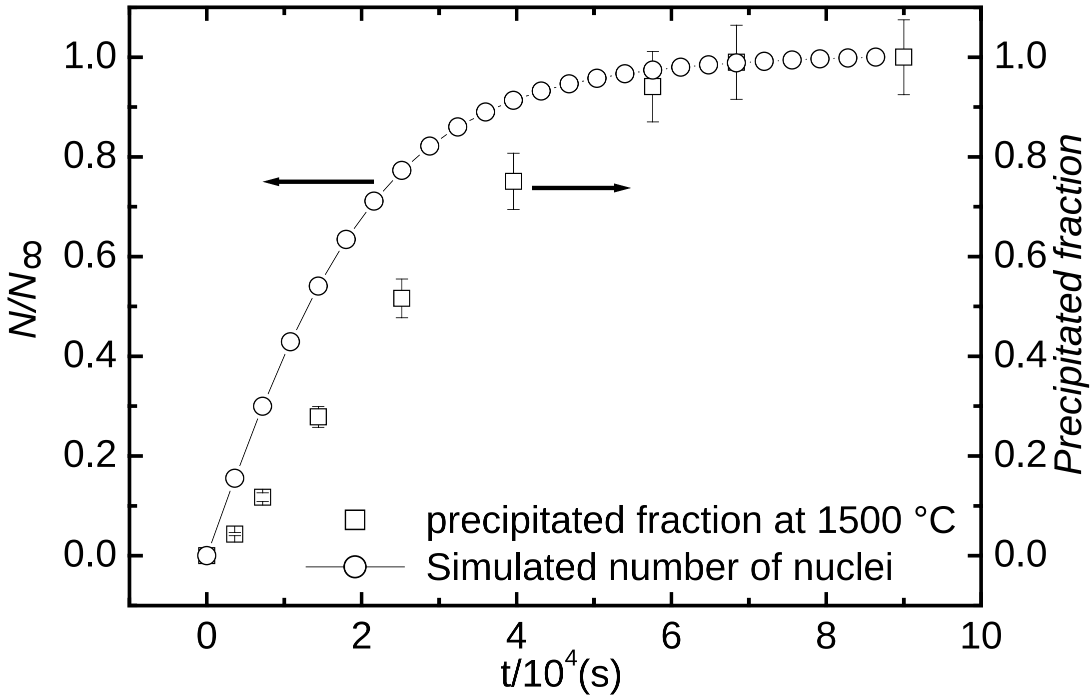

Fig. 6.42: *Simulated number of nuclei at constant nucleation rate in the grain boundary of the sample B451 annealed at 1500 °C. For comparison the precipitation kinetics of the same sample is plotted*

6.3.1.2 Simulation of the precipitation kinetics

At each time t, the radius R(t) of a growing particle can be determined using equation (6.10). This radius is then introduced as the limit of the integral in the equation (6.19), which enables the determination of the precipitated fraction. The obtained precipitated fraction is introduced in equation (6.13) in order to calculate the total amount of the transformed volume. This procedure is repeated for each $t_n = t_0 + nl$ (n is an integer and l is the step) until the end of the process. Note that for the simulation we consider $\rho_B I_B >> I_V$.

For a better understanding of the influence of the simulation parameters an exhaustive inventory of all parameters participating in the simulation with the corresponding observations is given Table 6.12. The boundary density can be experimentally estimated by measuring the grain sizes. The number of particles nucleating within the bulk is negligible. Therefore, the nucleation rates and consequently the density of nuclei in the volume are considered as negligible against their counterparts in the grain boundary. The width of the boundary layers is of the same order as the interatomic space and the thickness of the precipitates is about one micrometer. The volume diffusion is obtained by extrapolating the determined diffusion coefficients obtained in paragraph (6.2.6). It appears that only two parameters are determinant for the simulation, namely the nucleation rate (I_B) as well as the amount of the pre-existing nuclei (N_{0B}) in boundaries.

***Table 6.12**: Kinetic parameters involved in the grain boundary model. The condition of the use of each parameter is also given.*

	Bulk	Grain boundaries	Conditions
Nucleation rate	$I_V [m^{-3}s^{-1}]$	$I_B [m^{-2}s^{-1}]$	$I_V << \rho_B I_B$
Pre-exiting nuclei	$N_{OV} [m^{-3}]$	$N_{OB} [m^{-2}]$	$N_{OV} << N_{OB}$
Diffusion coefficients	$D_V [m^{-2}s^{-1}]$	$D_B [m^{-2}s^{-1}]$	no direct influence of D_B
Grain boundaries density		$\rho_B [m^{-1}]$	$(3.0 \pm 1)x\ 10^5\ m^{-1}$
Width of boundary layer		$a [m]$	$\pi\ x\ 10^{-10}$ m
Thickness of the particle	h	$h [m]$	10^{-6} m

However, the correlation between these two parameters has to be defined. To achieve this objective, one of the parameters was fixed whereas the other was varied and vice versa.

(i) I_B is constant, however different from zero i.e. the precipitation proceeds with constant rate of formation of new nuclei at boundaries.

It can be shown in Fig. 6.43 that for a chosen nucleation rate, the variation of the pre-existing nucleation does not affect the precipitation kinetics significantly as long as N_{0B} remains smaller than $I_B\Delta t$. The first deviation of the kinetics is observed when N_{0B} is equal to or higher than $I_B\Delta t$. Δt represents the total duration of the precipitation process. This suggests that as long as the amount of the new nuclei formed in boundary remains higher than that of the pre-existing nuclei, there is no significant influence of N_{0B} on the transformation process. Thus the new particles formed with the boundary are determinant. However, the JMAK plot can be divided into two distinct linear parts indicating changes in the dimensionality of the growth or in the nucleation mode as the crystallisation proceeds (Fig. 6.44). The local JMAK exponent in Fig. 6.45 (curve (I)) decreases monotonically from 2 in the earlier stages to about 0.5 at the end of the transformation when $I_B\Delta t > N_{0B}$. For $N_{0B} > I_B\Delta t$ (curves (II) and (III)) a strongly non-monotonic behaviour is observed. At the beginning of the transformation process it is close to 1, due to the presence of pre-existing nuclei. The non-linearity of the exponent is a direct consequence of the heterogeneous nucleation. The first limits represent the values of the JMAK exponent obtained from the classical Avrami approach for a two-dimensional diffusion controlled growth with constant nucleation rate or with site saturation (however in volume). As can be seen in Fig. 6.45 (curves (I), (II) and (III)), after some time, when the nucleation and diffusion zones of the particles are overlapped, the precipitation is slowed down (deviation from linear behaviour) and the value of the JMAK exponent falls down to n

= 0.5, which corresponds to a one-dimensional growth from pre-existing nuclei. At this stage no more new nuclei can be formed at grain boundaries due to impingement and only the already existing nuclei may grow.

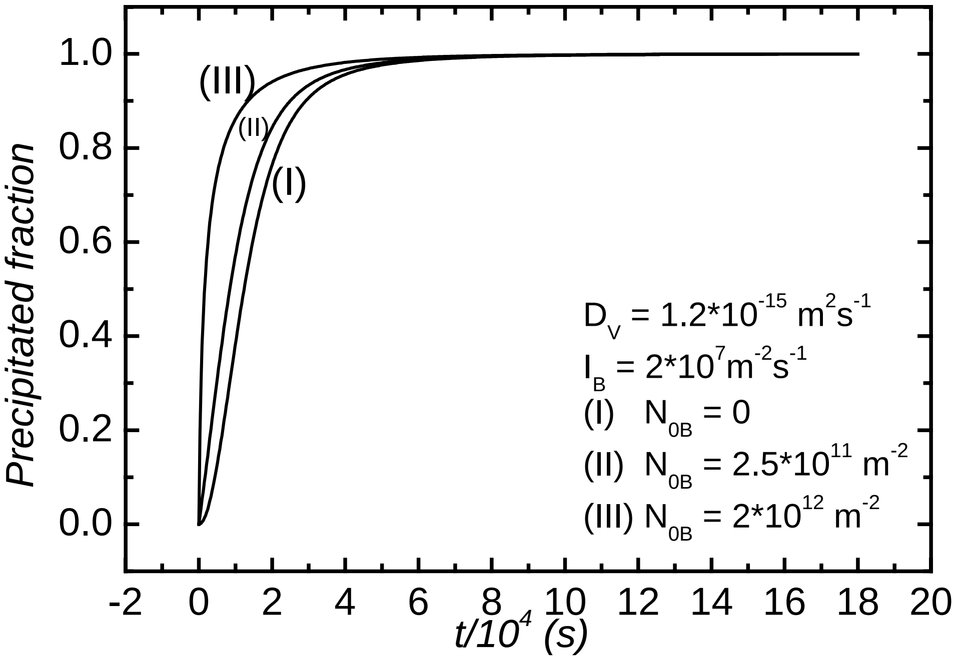

Fig. 6.43: Simulation of the precipitation kinetics at constant nucleation rate ($N_{0B} << I_B\Delta t$, $N_{0B} \rightarrow I_B\Delta t$ and $N_{0B} > I_B\Delta t$).

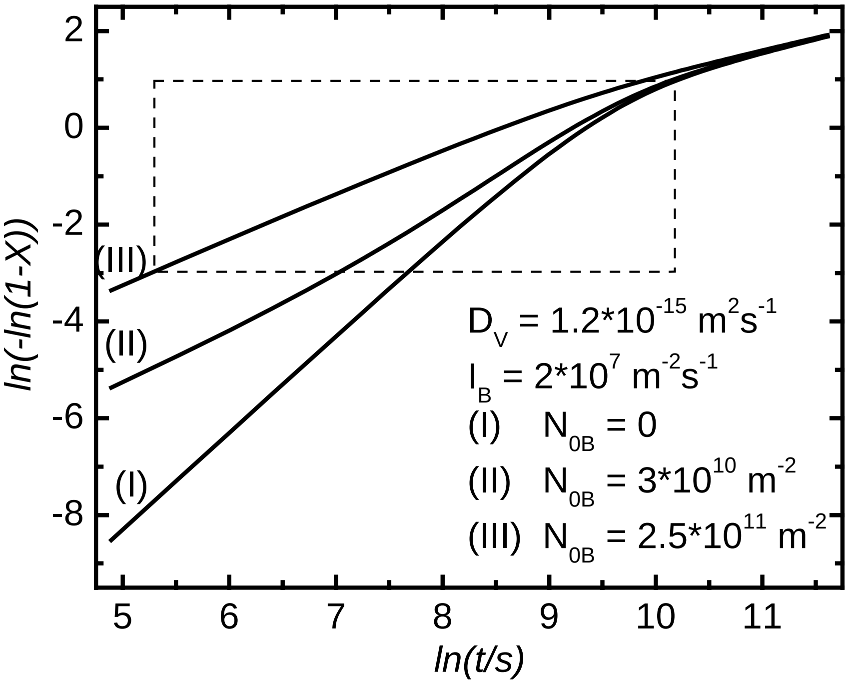

Fig. 6.44: Simulation of the JMAK plots at constant nucleation rate ($N_{0B} << I_B\Delta t$, $N_{0B}\rightarrow I_B\Delta t$, $N_{0B} > I_B\Delta t$). The dashed lines indicate the region where experimental data can be obtained.

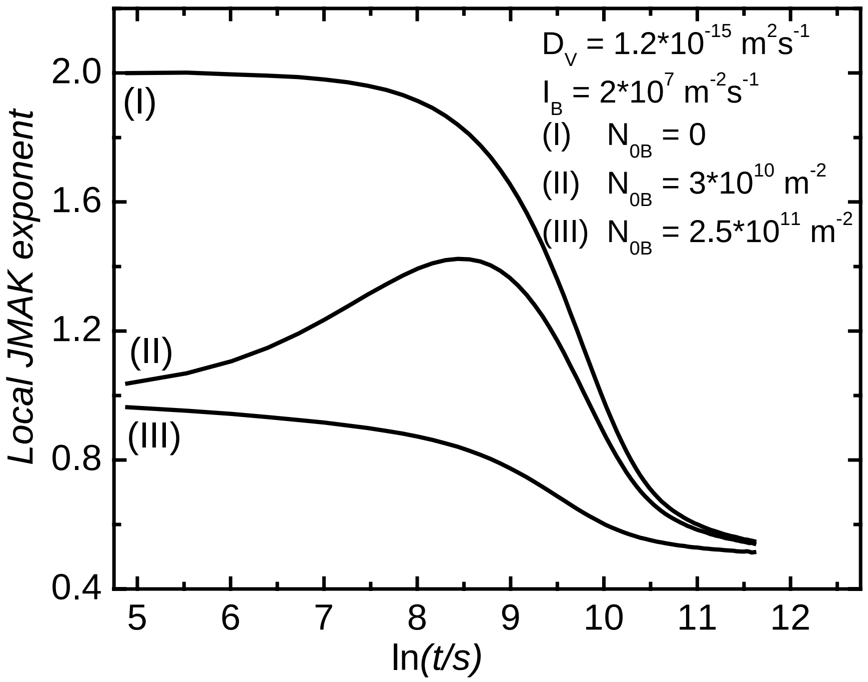

Fig. 6.45: *Simulation of the local JMAK exponent at constant nucleation rate (*$N_{0B} << I_B\Delta t$, $N_{0B} \rightarrow I_B\Delta t$, $N_{0B} > I_B\Delta t$

(ii) $I_B = 0$ i.e. there are no new nuclei formed during the precipitation process, meaning that only pre-existing nuclei are growing as the crystallisation proceeds.

In this case, the precipitation kinetics is different from that obtained in the preceding case (Fig. 6.46). In fact the case $I_B = 0$ is similar to the case of two-dimensional growth process from pre-existing nuclei obtained from the classical JMAK model. The obtained local JMAK exponent varies very slowly, being very close to $n = 1$ (Fig. 6.47) independently of the chosen values of N_{0B}. The small decrease of the JMAK exponent observed is due to the non-linearity introduced by the geometry of the intersection areas. However the straight lines of the JMAK plots indicated that there is no change in the dimensionality and the nucleation mode during the process (Fig. 6.48).

It is also interesting to realise which range of the calculated precipitation curves can be attained experimentally. It will be shown in the next paragraph that a precipitated fraction in the range 0.05 to 0.95 can be measured with adequate accuracy. Fig. 6.44 shows that in this range the calculated curves can be approximated by a roughly straight line, meaning that a change in the precipitation mode is not necessarily observed in the experiments. However, different slopes of the straight line indicates observable different precipitation modes for different values of I_B and N_{0B}.

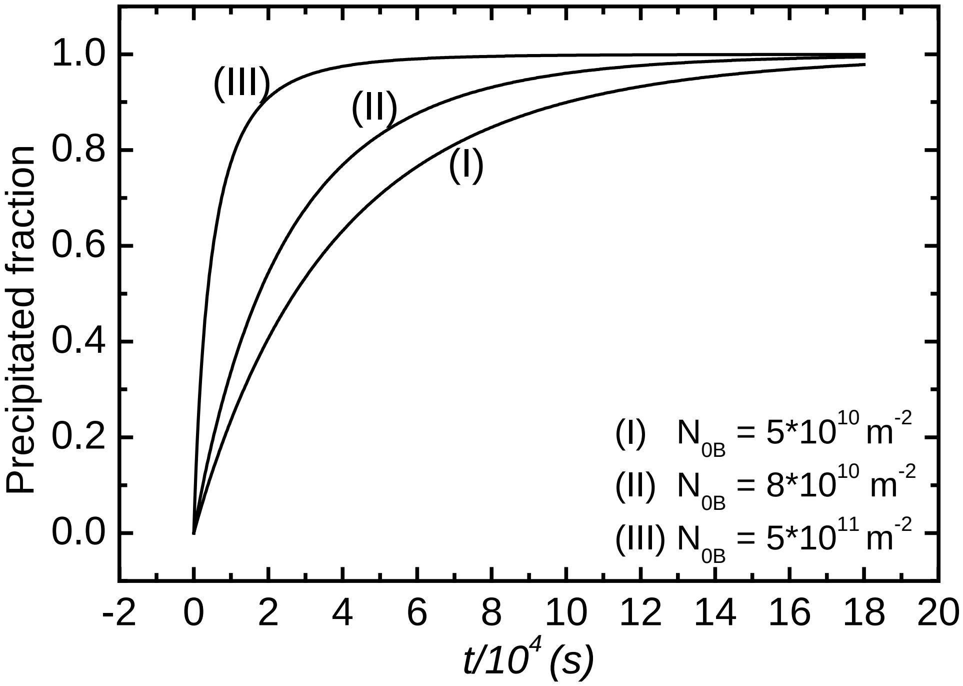

Fig. 6.46: *Simulation of the precipitation kinetics from the grain boundary model with* $I_B = 0$ *and for an effective diffusivity of* $D_V = 2.7 \times 10^{-16} . m^2 s^{-1}$

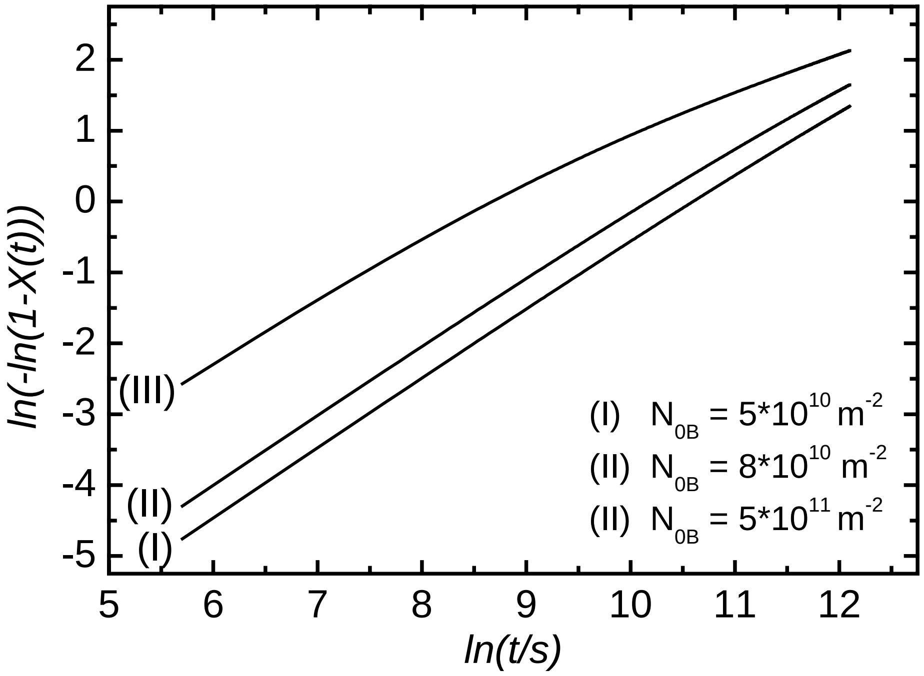

Fig. 6.47: *Simulation of the JMAK plots from the grain boundary in the case of* $I_B = 0$ *and for an .effective diffusivity of* $D_V = 2.7 \times 10^{-16}\ m^2 s^{-1}$

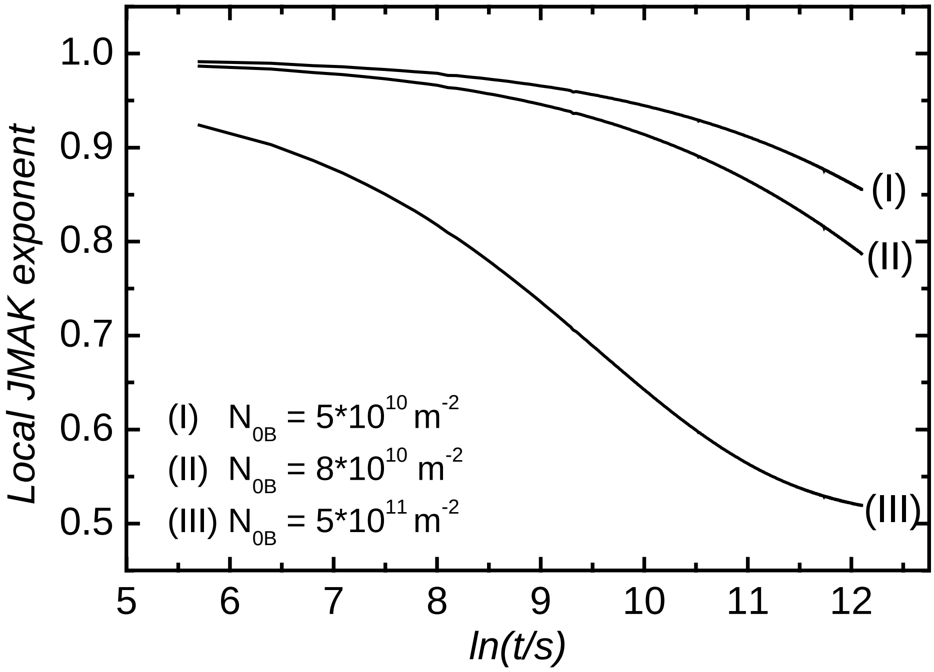

Fig. 6.48: *Simulation of the local JMAK exponent from the grain boundary model in the case of* $I_B = 0$ *and for an effective diffusivity of* $D_V = 2.7 \times 10^{-16}\ m^2s^{-1}$.

(iii) $I_B = N_{0B} = 0$, i.e. there is no contribution of grain boundaries to the nucleation process. In this case the contribution of the volume is obviously dominant. This kinetics can be described by the classical two-dimensional growth with constant nucleation rate.

The above considerations combined with SEM observations lead to the conclusion that the plate-like precipitates nucleate preferably at grain boundaries and grow into the interior of the matrix according to a two-dimensional diffusion-controlled growth process.

6.3.1.3 Comparison with the experimental kinetics

In order to check the influence of N_{0B} on the experimental kinetics, a comparison of experimental data with the grain boundary model data is done. For $N_{0B} \ll I_B\Delta t$, a value of I_B, which corresponds to the best fit of the experimental data, is obtained. However, for $N_{0B} \rightarrow I_B\Delta t$, a strong deviation of the theoretical curve is observed. Afterwards we let I_B progressively decrease down to zero in order to see whether the theoretical curve can fit the experimental data again. As can be seen in Fig. 6.49, it is impossible to recover the best fit of the experimental data neither for $N_{0B} \sim I_B\Delta t$ nor for $I_B = 0$. Therefore the condition to fulfil in order to describe the experimental data should be $N_{0B} << I_B\Delta t$ or $N_{0B} = 0$.

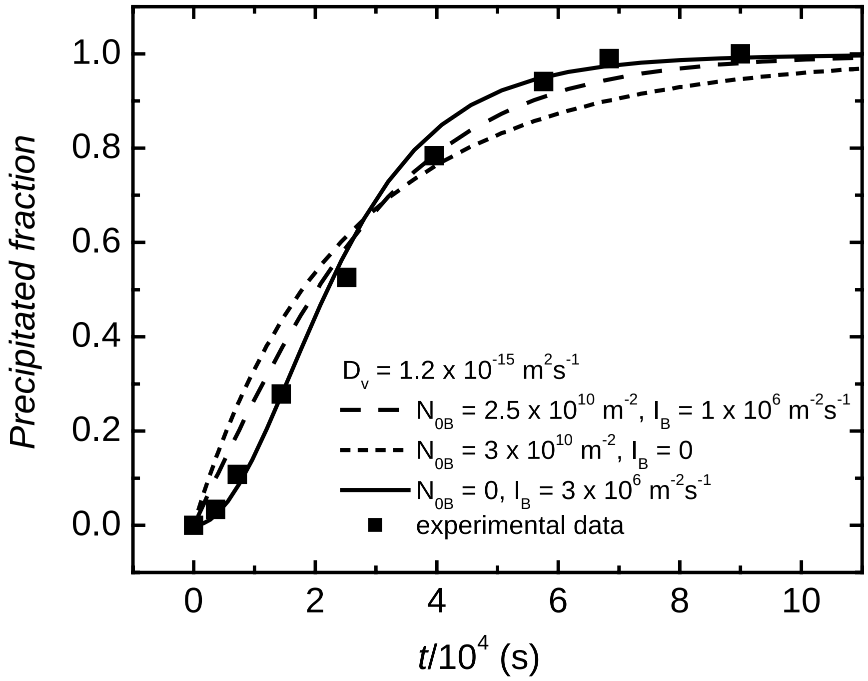

Fig. 6.49: *Comparison of the GB model with the experimental kinetics of the sample B451 annealed at 1500 °C. The best fit correspond to the case* $N_{0B} = 0$.

The GB model was used to describe the precipitation kinetics of B352 and B451. In order to make a comparative investigation of the kinetic parameters the following procedure was applied:

(i) The value of D_V is first of all determined by fitting the time-dependent precipitate size with equation (6.12) (Fig. 6.50).

(ii) The JMAK and the GB models are used to fit the experimentally precipitation data. The value of the nucleation rate is extracted under the assumption that $N_{0B} << I_B \Delta t$. A mean squares fit enables the determination of the varying parameters (Fig. 6.51, Fig. 6.52, Fig. 6.53, Fig. 6.54).

(iii) The obtained simulated kinetics from the GB model is once again fitted by the classical JMAK equation to evaluate the rate constants and to improve the accuracy of the refinement (Fig. 6.55 and Fig. 6.56). The JMAK exponent is determined in three different ways: first of all by directly fitting of the experimental data with the classical JMAK formula, secondly by fitting the simulated data with the JMAK formula and thirdly by fitting the first linear part of the JMAK plots emerging from the simulated kinetics (Fig. 6.57 and Fig. 6.58).

(iv) Each simulated kinetics is used to plot the time dependence of the local JMAK exponent which enables a better understanding of the time evolution of the growth process (Fig. 6.59 and Fig. 6.60).

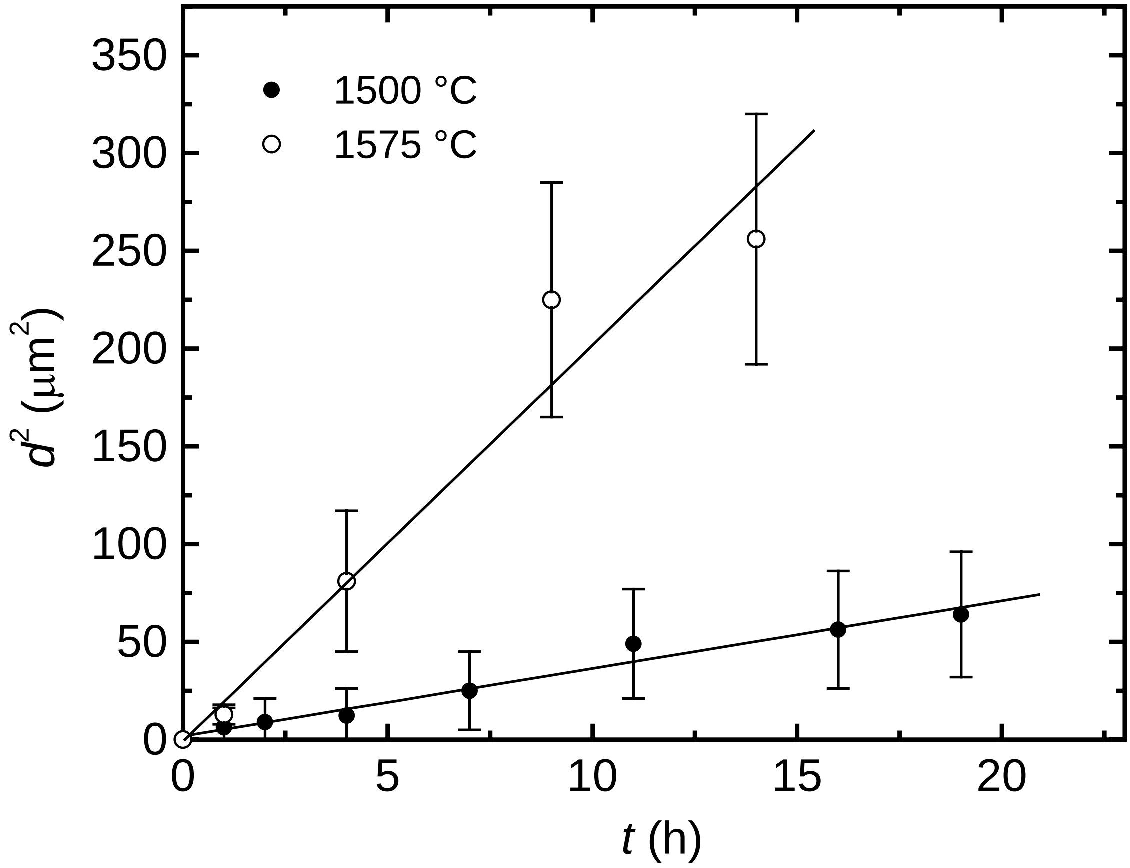

Fig. 6.50: *Precipitate sizes of the sample B451 annealed at different temperatures. Comparison with equation (6.12) (straight lines).*

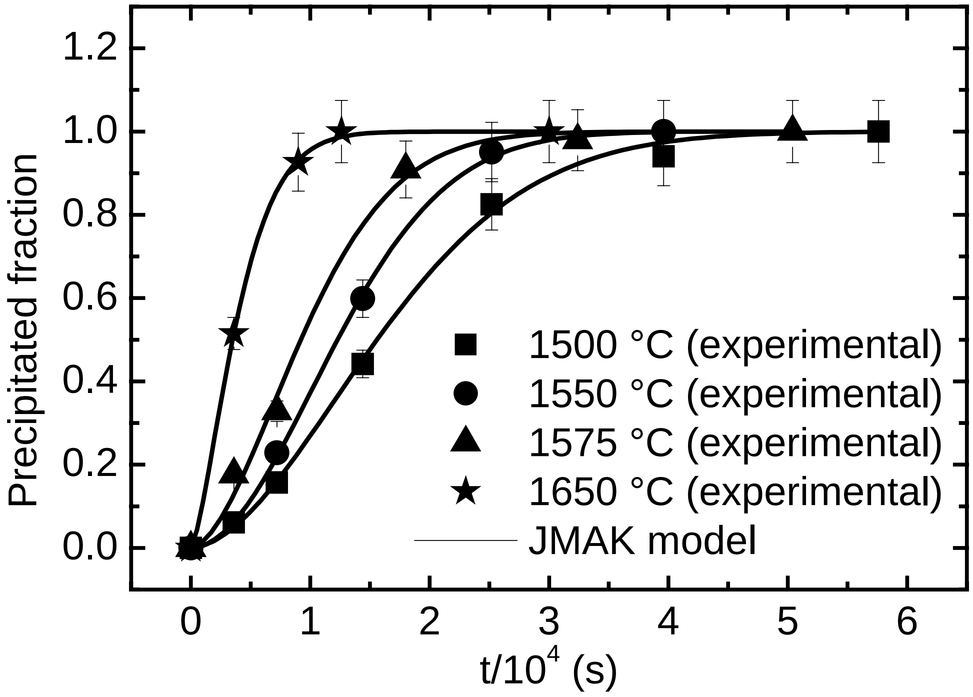

Fig. 6.51: *Time dependent precipitation kinetics of the sample B352 fitted by the classical JMAK equation.*

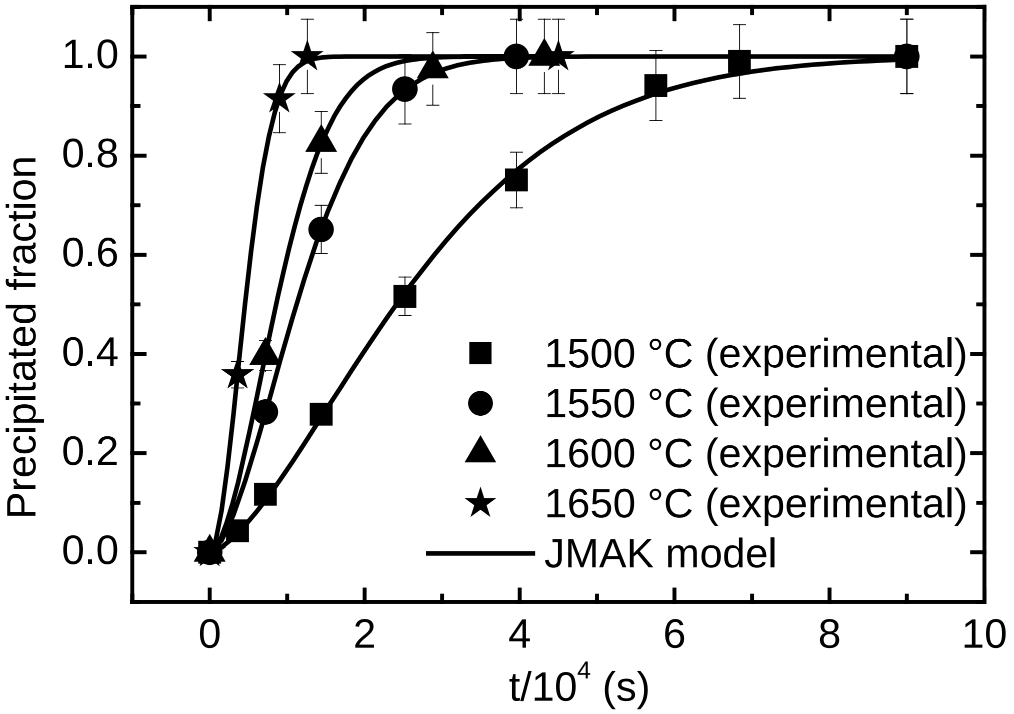

Fig. 6.52: *Time dependent precipitation kinetics of the sample B451 fitted with the classical JMAK equation.*

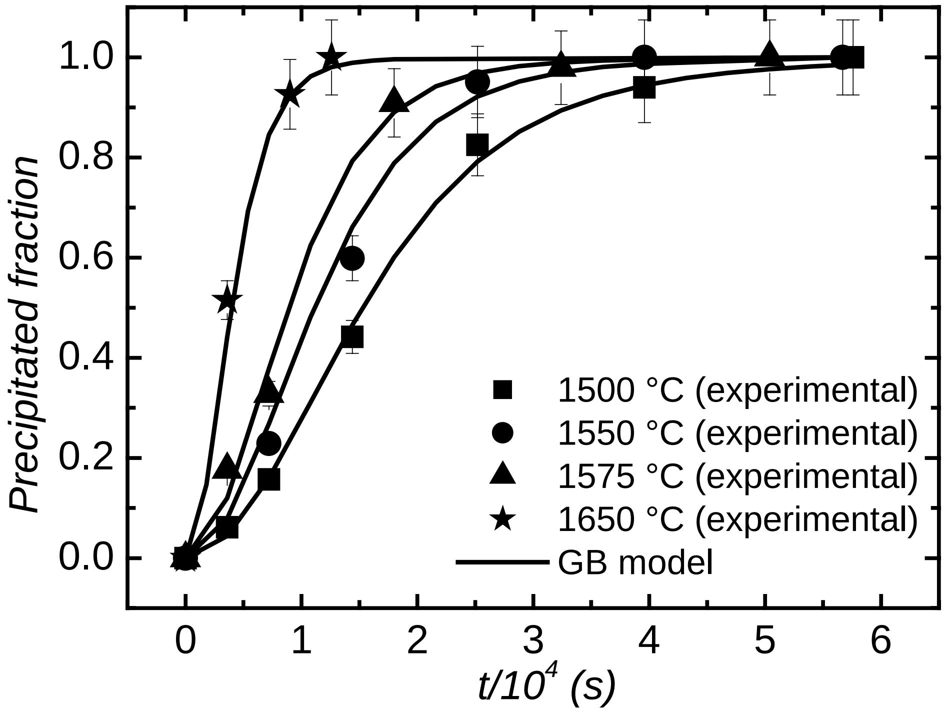

Fig. 6.53: *Time dependent precipitation kinetics of the sample B352 compared with the GB model.*

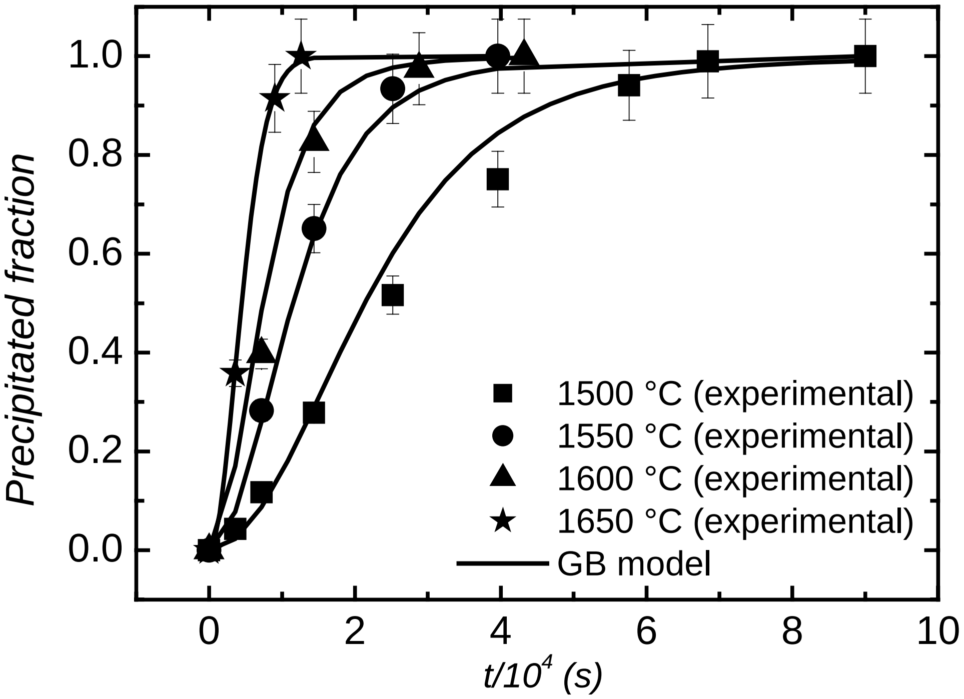

Fig. 6.54: *Time dependent precipitation kinetics of the sample B451 compared with the GB model.*

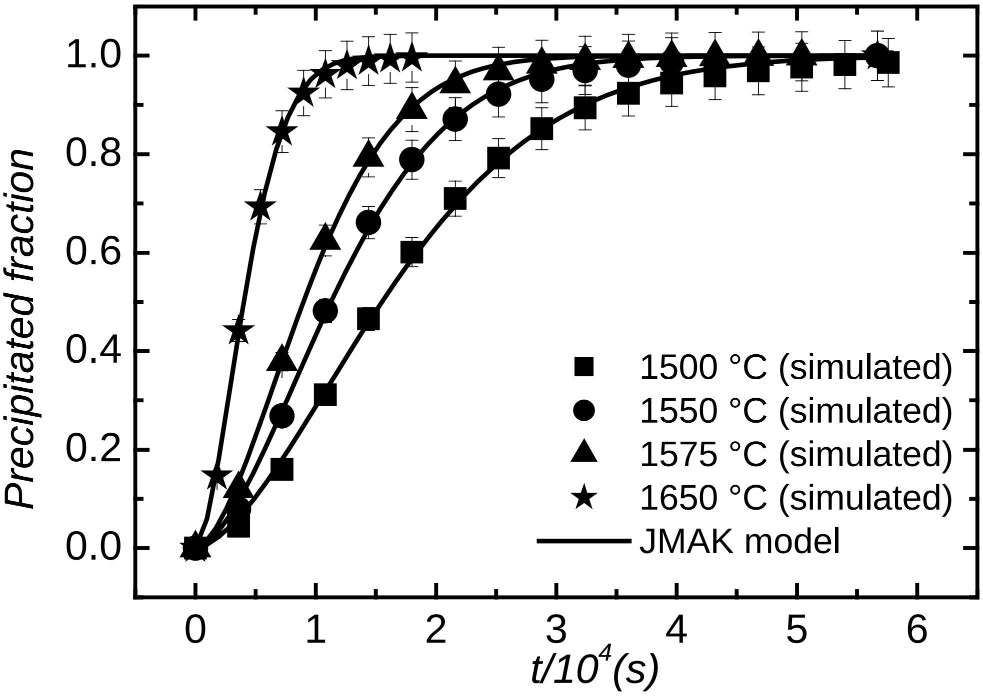

Fig. 6.55: *Time dependent precipitation kinetics of the sample B352 generated by the grain boundary model and fitted with the JMAK model.*

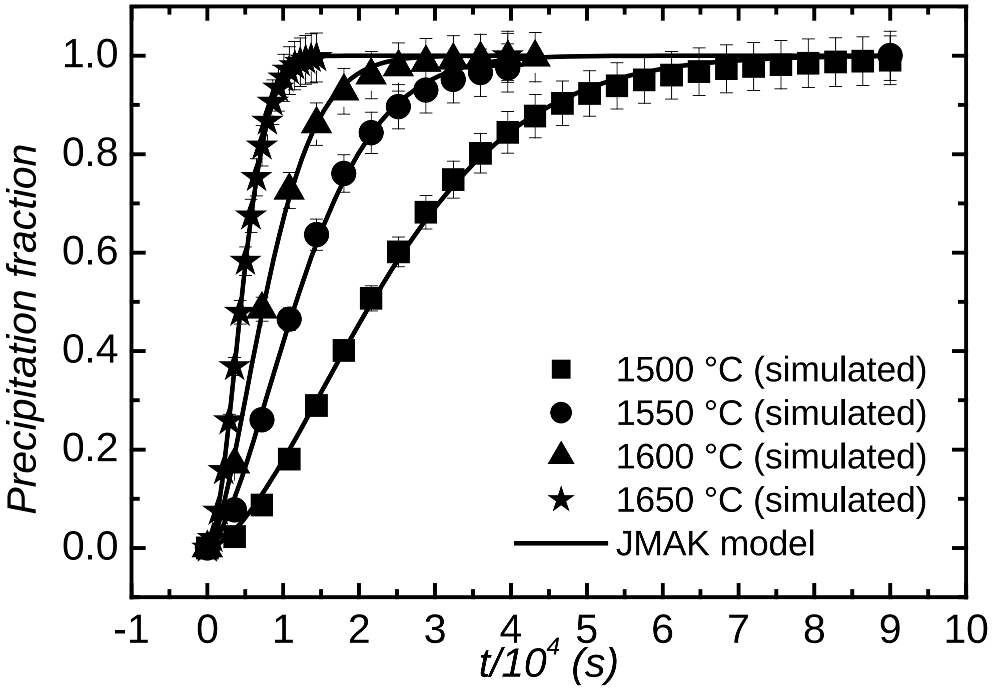

Fig. 6.56: *Time dependent precipitation kinetics of the sample B451 generated by the grain boundary model and fitted with the JMAK model.*

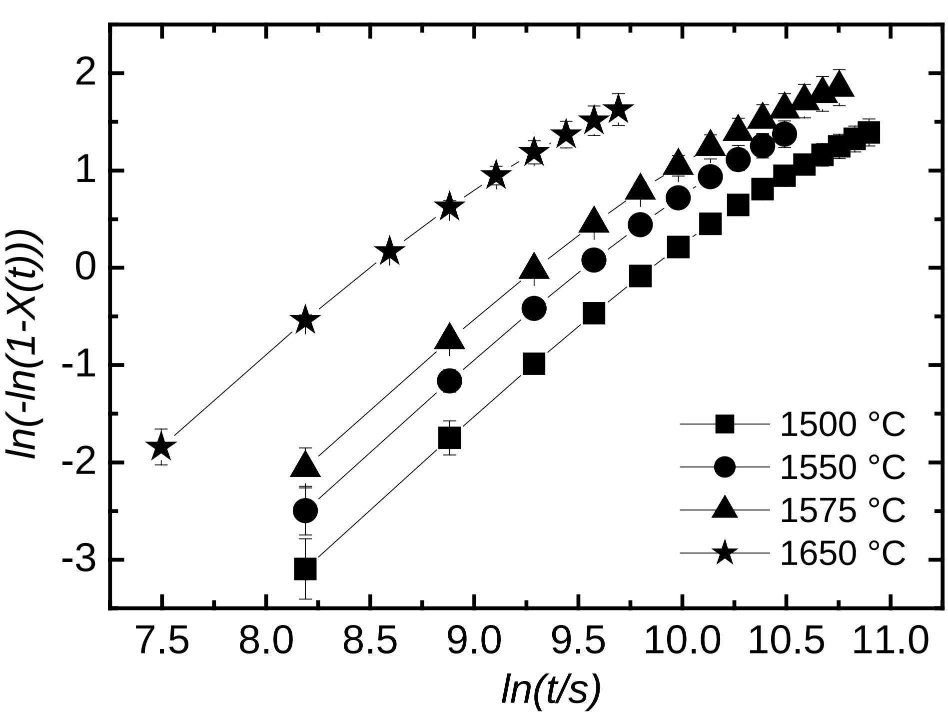

Fig. 6.57: *Simulation of the JMAK plots of the sample B352. Non-linearity due to the heterogeneous nucleation is observed at the end of the precipitation process. The effective diffusivities can be found in Table 6.11.*

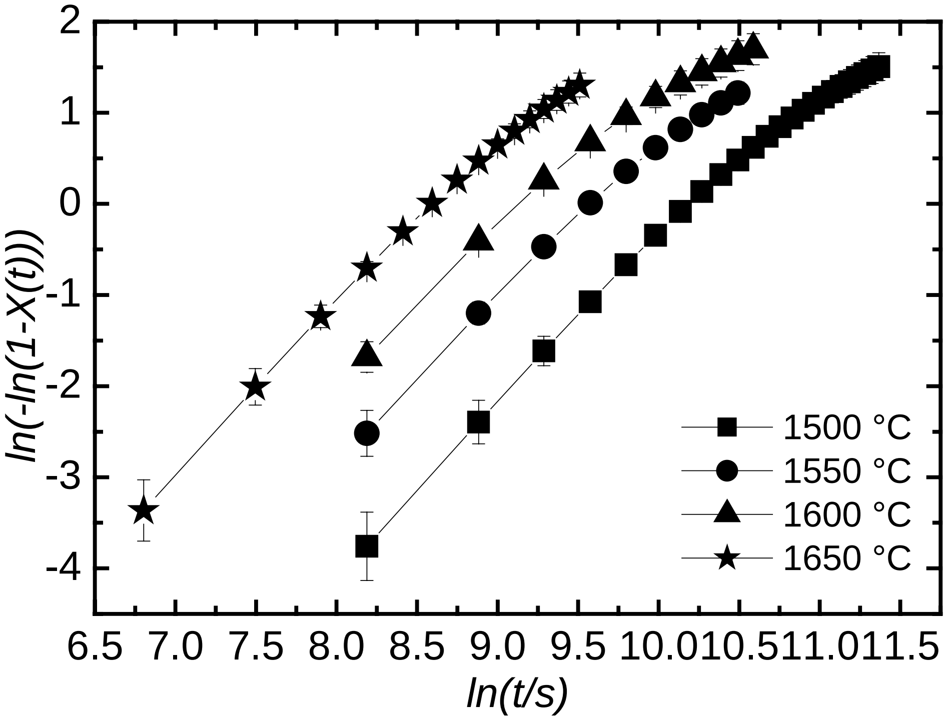

Fig. 6.58: *Simulation from GB model of the JMAK plots of the sample B451. Non-linearity due to the heterogeneous nucleation is observed at the end of the precipitation process. The effective diffusivities can be found in Table 6.11.*

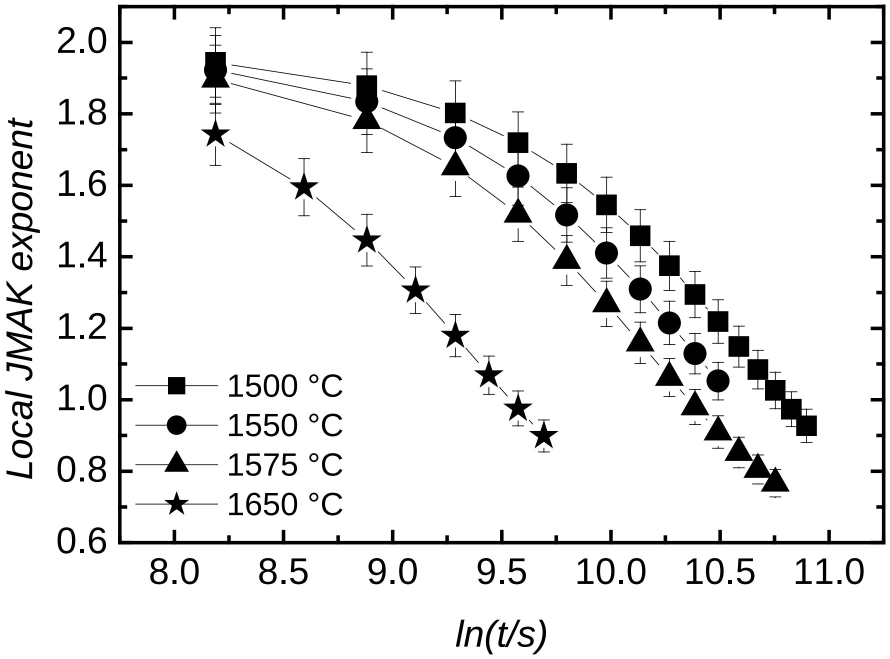

Fig. 6.59: Simulation of the time evolution of the local JMAK exponent for the sample B352. The effective diffusivities can be found in Table 6.11.

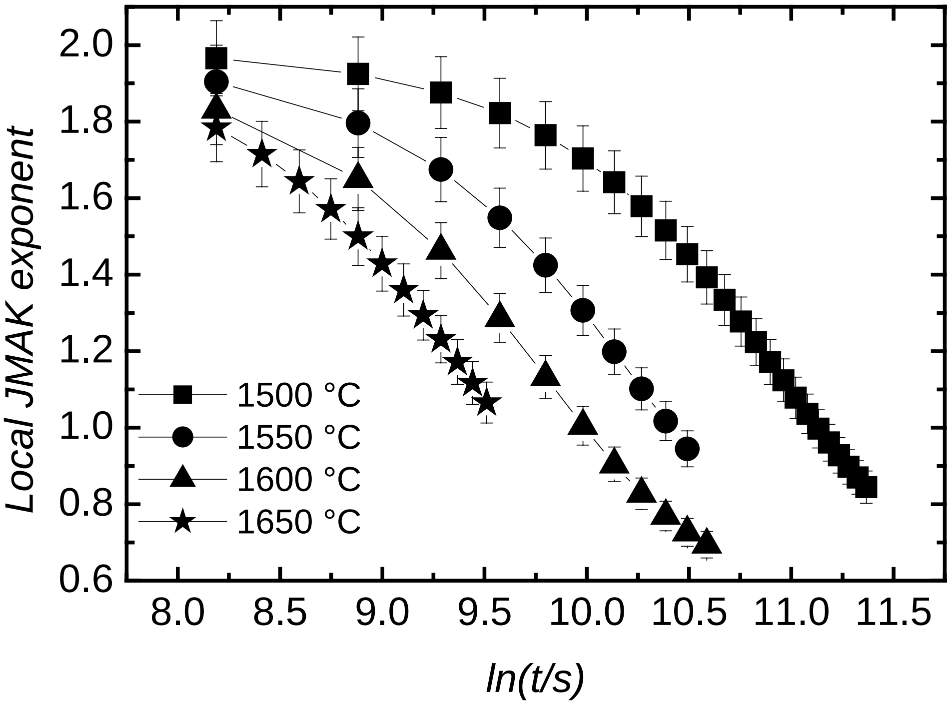

Fig. 6.60: Simulation of the time dependence of the local JMAK exponent for the sample B451.The effective diffusivities can be found in Table 6.11.

According to the classical JMAK theory, the Avrami exponent can take the value 1 or 2 for the two-dimensional growth at site saturation or pre-existing nuclei, respectively. The fit of the experimental precipitation kinetics with JMAK leads to values of the JMAK exponent between 1.4 and 1.8, which does not explain satisfactorily the dimensionality of the growth of the particles observed with SEM images. For a better understanding the simulated local JMAK exponents, obtained from the GB model, are plotted as a function of time. As shown in Fig. 6.59 and Fig. 6.60, the exponent does not remain constant but varies between extreme values corresponding to the site saturation and continuous nucleation in the JMAK formalism. The JMAK exponent is relatively constant at the beginning but falls rapidly as the precipitation process tends towards saturation. This effect can be attributed to the impingement of the already grown particles or the densely packed nucleated particles at grain boundaries, which slow down the nucleation and the growth processes. In Fig. 6.59 and Fig. 6.60, it can be seen that the exponent decreases down to 0.7. This means that in the latest stage of the precipitation the precipitates tend to grow only in one direction. The description of the precipitation process by the modified JMAK model with the introduction of the contribution of grain boundaries to the nucleation leads to the conclusion that the decrease of the JMAK exponent corresponds to the volume growth of particles heterogeneously nucleated at grain boundaries.

However, the most important parameter achieved for the GB model remains the nucleation rate at grain boundaries (I_B). All parameters obtained from this simulation are gathered in Table 6.13 and Table 6.14

Table 6.13: *Kinetic parameters of the sample B352 as obtained from the simulation with the grain boundary model (I_B) and the fit of the classical JMAK equation. The stars correspond to values of the milled sample (A352).*

Temperature (°C)	JMAK exponent	k_{JMAK} (s^{-1}) x 10^{-5}	I_B($m^{-2}s^{-1}$) x 10^{6}
1400	1.50 ± 0.1	2 ± 0.06	4 ± 0.5
*1450	1.0 ± 0.02	3 ± 0.01	
1500	1.70 ± 0.08	5 ± 0.1	9.1 ± 1.3
1550	1.90 ± 0.07	7 ± 0.1	9.5 ± 1.4
1575	1.70 ± 0.1	9 ± 0.4	11.0 ± 1.6
*1600	0.9	10.3 ± 0.1	
1650	1.40± 0.06	22 ± 0.4	31.5 ± 4.0
1675	1.5	16 ± 2	4.5 ± 1
1700	1.8 ± 0.1	6 ± 0.4	1.6 ± 0.5

Table 6.14: *Kinetic parameters of the sample B451 as obtained from the simulation with the grain boundary model (I_B) and the fit of the classical JMAK equation.*

Temperature (°C)	JMAK exponent	k_{JMAK} (s^{-1}) x 10^{-5}	I_B($m^{-2}s^{-1}$) x 10^6
1500	1.5 ± 0.04	3.2 ± 0.05	3 ± 0.9
1550	1.60 ± 0.04	7.0 ± 0.02	6.8 ± 1.7
1575	1.20 ± 0.03	8.0 ± 0.02	9.0 ± 2.2
1600	1.80 ± 0.08	9.0 ± 0.15	6.0 ± 1.5
1650	1.90 ± 0.02	18.0 ± 2	13 ± 3.5
1675	1.5 ± 0.02	13.0 ± 5	4.0 ± 1.0
1700	1.6 ± 0.2	10.0 ± 3	1.7 ± 0.5

6.3.2 Activation enthalpies

As explained before, diffusion is one of the two important mechanisms involved in the precipitation of the diboride solid solutions. The diffusion coefficients in the volume are obtained by the method presented in paragraph 6.2.6. These diffusion coefficients follow an Arrhenius behaviour and lead to an activation enthalpy of ΔH_g = (3.6 ± 0.3) eV for both samples B352 and B451 (Fig. 6.61) and with a pre-exponential factor of $D_0 = 3.8 \times 10^{-5}$ m^2s^{-1}. For comparison, the extrapolation of tracer diffusion coefficients are represented in the same figure. This result is in good agreement within the estimated error with the activation enthalpy, (3.9 ± 0.5) eV, obtained by Schmidt [Sch05] from measurements of Ti tracer diffusivities in this ceramic system. Ti is found to be the slowest-diffusing species in these materials and should consequently be growth limiting. This result confirms also that the growth of the W_2B_5 platelets is fully controlled by the volume diffusion. As pointed out in paragraph 6.2.6 the Ti tracer diffusivities are lower by about three orders of magnitude. This difference is unexplained at the moment. However, because precipitate growth should be governed by chemical diffusion in the gradient of the chemical potential, interdiffusion measurements are necessary for correct interpretation of the data. A further possible reason for the discrepancy between the tracer diffusivities and the diffusivities obtained from the growth data might be the influence of dislocations or stacking defaults, which are present in the diboride compounds [Sch01]. The same value of the activation enthalpy however indicates that the same energetic processes are present.

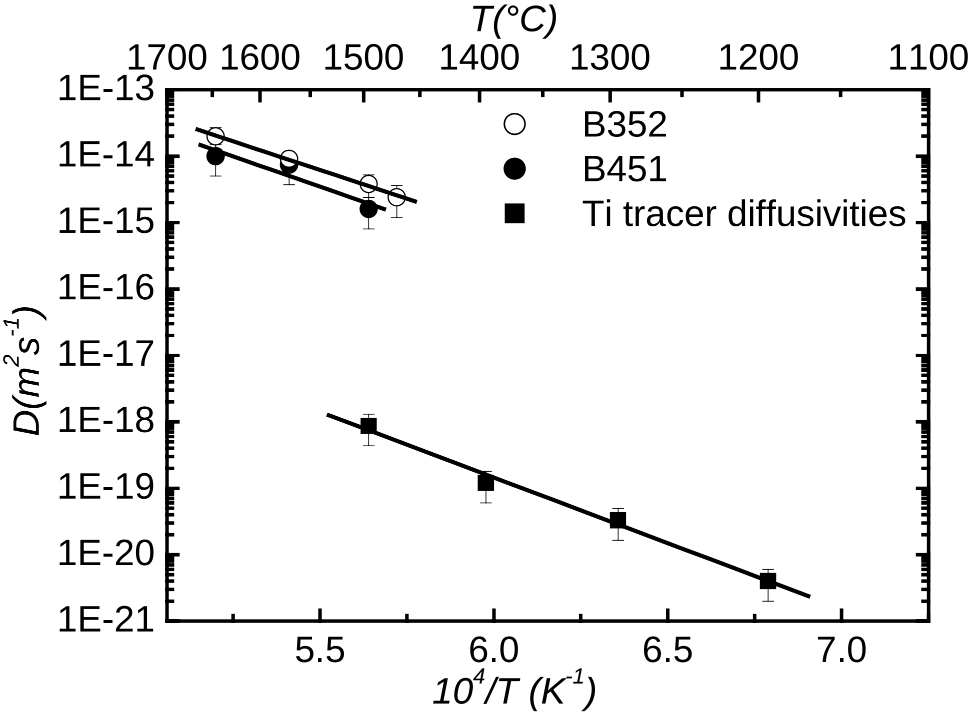

Fig. 6.61: *Arrhenius plots of the diffusion coefficients for samples B352 and B451 obtained using the time dependence of the precipitate sizes. For comparison the tracer diffusivities of titanium in the same system are also plotted [Sch05].*

Moreover, activation energy for nucleation can be calculated using the thermally activated nucleation rate obtained from the GB model. According to the theory of homogeneous nucleation, the nucleation rate can be related to the Gibbs free energy change for the formation of a critical particle ΔG* and the activation enthalpy ΔH_N which an atom needs to cross the phase interface and its subsequent incorporation into the lattice of the precipitate. The relation corresponding to the nucleation from the condensed phases is given by [Chr75]

$$I = \nu N \exp\left(-\frac{\Delta H_N + \Delta G^*}{k_B T}\right) \tag{6.22}$$

where N is the density of pre-existing nuclei in the volume and ν is the effective attempt frequency.

The modifications required for changing from the equation for homogeneous nucleation to that for heterogeneous nucleation consist in substituting N by N^s and by multiplying ΔG* by a function of a single parameter α [Chr75]. ΔG* is defined by equation (4.8) as the Gibbs free energy of formation in the volume, the parameter α is the contact angle between the nuclei and the surface of the gain boundary, and N^s is the number of nuclei in equilibrium at grain boundaries. It follows

$$I^S = \nu N^S \exp\left(-\frac{\Delta H_N + \Delta G^S}{k_B T}\right) \tag{6.23}$$

where

$$\Delta G^S = \Delta G^* \frac{2 - 3\cos\alpha + \cos^3\alpha}{4} \tag{6.24}$$

The Gibbs free energy of formation at grain boundaries is proportional to $\frac{1}{\Delta S^2 (T_e - T)^2}$ [Lia94]. $\Delta T = T_e - T$ is the undercooling of the material compared to a temperature T_e where matrix phase and precipitate phase are in equilibrium. Therefore equation (6.23) can be written as

$$I^S = I_0 \exp\left(-\frac{\Delta H_N}{k_B T} - \frac{B}{k_B (T_e - T)^2 T}\right) \tag{6.25}$$

where I_0 is the pre-exponential factor and B is given by

$$B = \frac{4\pi\sigma^3 \left(2 - 3\cos\alpha + \cos^3\alpha\right)}{3\Delta S^2} \tag{6.26}$$

It can be seen from Fig. 6.62 that the nucleation rates exhibit a non-monotonic behaviour, where $\log(I_B)$ increases with reciprocal temperature between 1700 °C and 1675 °C, has a maximum around 1675 °C and decreases for lower temperatures. This observation can be explained by the fact that, at temperature around 1675 °C the matrix tends the equilibrium and the driving force is reduced. Consequently the reaction is slowed down.

The best fitting of the plots of the nucleation rates as function of inverse temperature with equation (6.23) is obtained with an activation enthalpy of about $\Delta H_N = (3.6 \pm 0.3)$ eV for both types of samples. According to the JMAK theory it is possible to determine rate constants from the steps (ii) and (iii) in paragraph 6.3.1.3. The rate constants obtained directly by fitting the experimental and the simulated data with JMAK were identical indicating the good accuracy of the GB model.

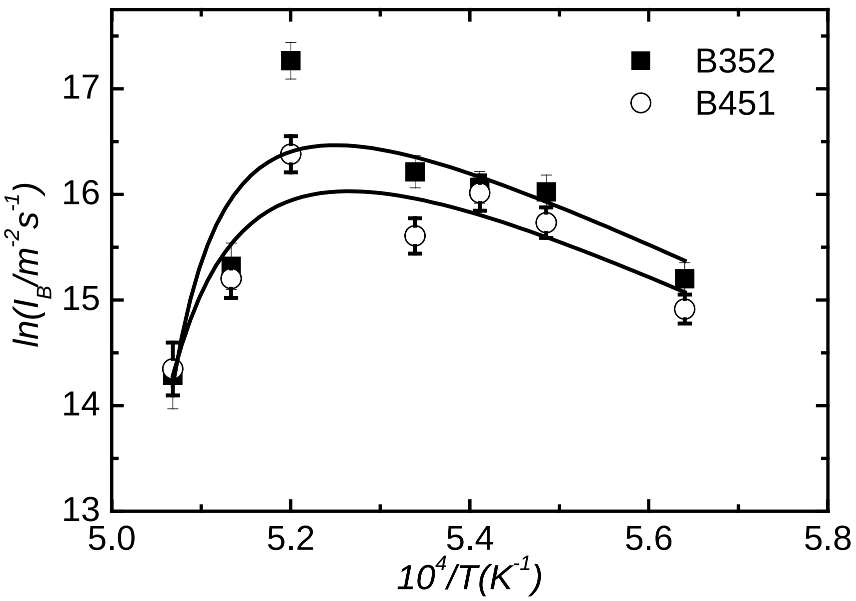

Fig. 6.62: *Plots of the nucleation rates obtained form the GB model as function of inverse temperature for samples B352 and B451and fitted with equation (6.25) and with* $I_0 = 7.7 \times 10^{16}\ m^{-2}s^{-1}$ $T_e = (1750 \pm 50)$ *°C and* $B = 4.9 \times 10^{-16}\ JK^2$.

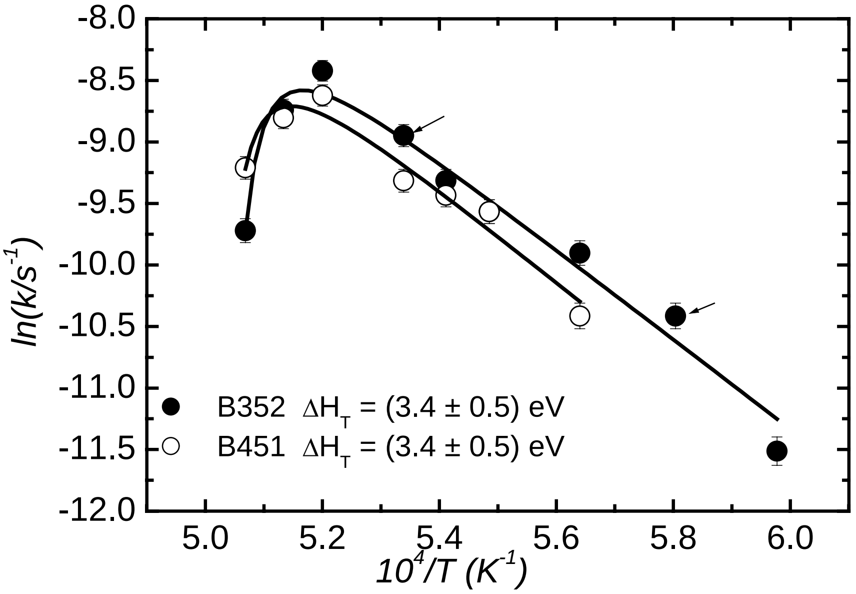

Fig. 6.63: *Plot of the rate constants obtained from the JMAK model for samples B352 and B451. The arrows indicate the rate constants measured from the pre-annealed sample (A352).*

This non-linear behaviour is a consequence of the undercooling. It can be also observed on Fig. 6.63 that these rate constants have the same behaviour as the nucleation rates.

By fitting the rate constants as function of inverse temperature with an equation similar to equation (6.25), an activation enthalpy can be obtained. In fact the rate constant can be related to the temperature via the Arrhenius equation:

$$k(T) = k_0 \exp\left(-\frac{\Delta H_T}{k_B T} - \frac{\Delta G^*}{k_B T}\right) \qquad (6.27)$$

The obtained enthalpy can be considered as the total energy for the whole precipitation process since the JMAK theory takes into account the nucleation as well as the growth processes. For both samples a total activation enthalpy of ΔH_T = (3.4 ± 0.5) eV was calculated.

But the determination of the rate constants with the JMAK model implies that the complete precipitation proceeds in the volume. This means that the homogeneous nucleation of the particles is assumed, which is in contradiction with the heterogeneous nucleation at grain boundary. However, it has been reported that, for phase transformation proceeding in the volume and for a mixture of nucleation modes, a general relation between the total activation enthalpy, the enthalpy of growth, ΔH_g activation enthalpy of nucleation, ΔH_N and the JMAK exponent can be found. Considering a two-dimensional growth controlled by diffusion this equation has been given [Kem01], [Rag81], [Krü93]:

$$\Delta H_T = \frac{\Delta H_g + (n-1)\Delta H_N}{n}. \qquad (6.28)$$

Taking an average JMAK exponent of 2, equation (6.28) leads to $\Delta H_T = \Delta H_N = \Delta H_g$ which is, within the margin of error, consistent to result obtained from the simulation.

As further results, from the fit of the nucleation rates to equation (6.25), an equilibrium temperature of about T_e = 1750 ± 50 °C is determined which means that at temperatures above T_e no precipitates are formed. For $T << T_e$, ΔG^* reaches a constant value of 4×10^{-4} eV, meaning that nucleation is controlled by the transfer of an atom across the phase boundary between precipitate and the matrix with an activation enthalpy of 3.6 eV. In contrast for $T_e < T < T^{max}$, ΔG^* becomes the dominating term which results in the decrease of the nucleation rate with increasing temperature and can be explained by the fact that ΔT becomes very small and the driving force of the nucleation approaches zero. Moreover, the fit of the experimental data in Fig. 6.62 and Fig. 6.63 to equation (6.25) with $\Delta H_N = 0$ does not give a reasonable description for the data, which means that the atomic transfer across the phase boundary is an important factor determining nucleation.

6.3.3 Role of chromium

Regarding the above results, it is worth to discuss the influence of the addition of chromium on the precipitation kinetics. The obtained activation enthalpies of growth and of nucleation are obviously identical for the samples B352 and B451 within the estimated error. This implies that the addition of chromium does not accelerate the precipitation kinetics. However, this conclusion does not mean that chromium has a negligible role but that the added amount must be chosen carefully and adequately. For instance Fig. 6.64 presents the time evolution of the diffraction patterns for a sample B550 (without chromium) at 1600 °C. It can be clearly observed that the precipitation process is substantially slowed down so that at high temperatures one has to wait more than 10 hours to observe the first significant XRD peaks corresponding to the presence of W_2B_5 precipitates.

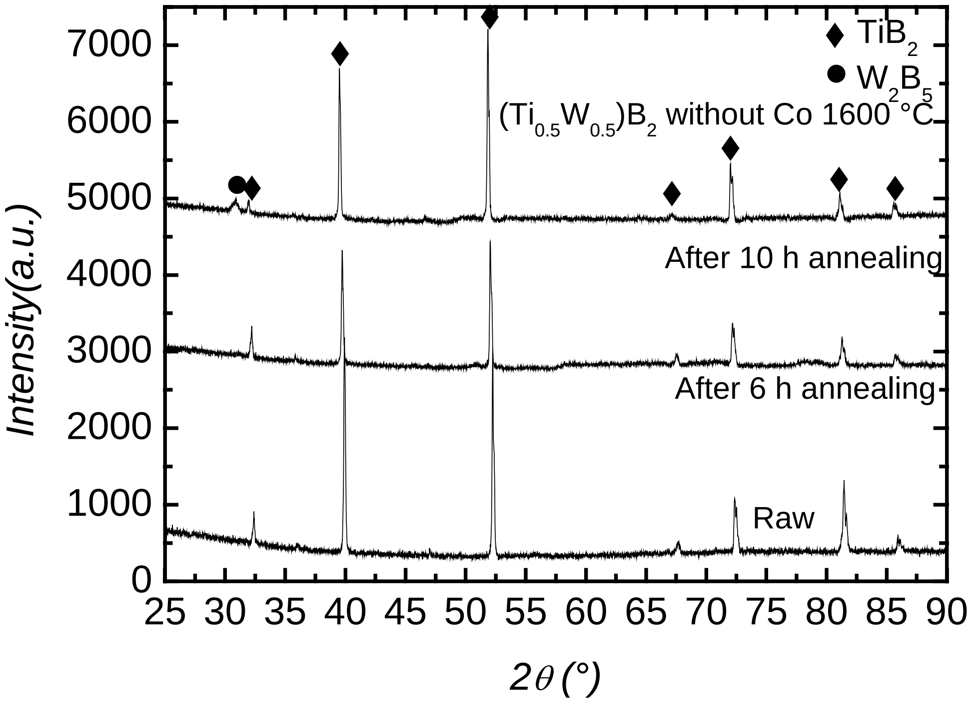

Fig. 6.64: *Sample B550 (without chromium and cobalt): Diffraction patterns of the raw sample and that annealed at 1600 °C for different times. The first small characteristic* W_2B_5 *peak appears after 10 hours.*

6.3.4 Role of cobalt

All samples that were milled and hot-pressed contained a small amount of Co (0.5 at. % - 1.5 at. %) resulting from the WC/Co milling balls (Table 6.6). The presence of cobalt influences the precipitation mechanism. The precipitation in the bulk of the sample A352 is the consequence of the addition of small amounts of Co. Thus cobalt increases considerably the density of the precipitates. This indicates that the milling step before the reaction sintering and the homogenisation steps enhances the precipitation of the second phase. A similar result was found in [Wat86] where the addition of 1.0 wt. % CoB markedly increased the densification of TiB_2. Therefore, samples having small amounts of Co present a high amount of pre-existing nuclei.

Moreover, the increase of the rate constants (indicated with arrows in Fig. 6.63) with increasing temperature is identical within the estimated error to those determined using the samples without cobalt. This indicates that the small amount of cobalt in the supersaturated matrix does not accelerate the precipitation kinetics. A consistent way to explain these results can be found under the assumption that for samples prepared from milled powders a significant additional amount of pre-existing nuclei are present before the grain growth (and additional continuous nucleation) starts. The Co impurities introduced by the milling process act as additional sites of heterogeneous nucleation and lead to the higher density of crystallites. Another possible interpretation is interaction between the borides and Co. Nickel, cobalt and iron were reported to form borides when added to TiB_2 [Jue91], [Fen01].

Therefore milled samples present a precipitation kinetics compatible with an JMAK exponent of about unity, which is consistent with a two-dimensional diffusion controlled growth and with pre-existing nuclei. This means that during the homogenisation (8 hours at 2000 °C) of the sample all particles are already nucleated. The grain boundary model can thus be applied to the kinetics of this sample in the case $N_{0B} >> I_B \Delta t$ or $I_B = 0$ corresponding to two-dimensional growth of pre-existing nuclei. Fig. 6.65 illustrats a comparison of this model with the experimental kinetics of such samples at 1450 °C.

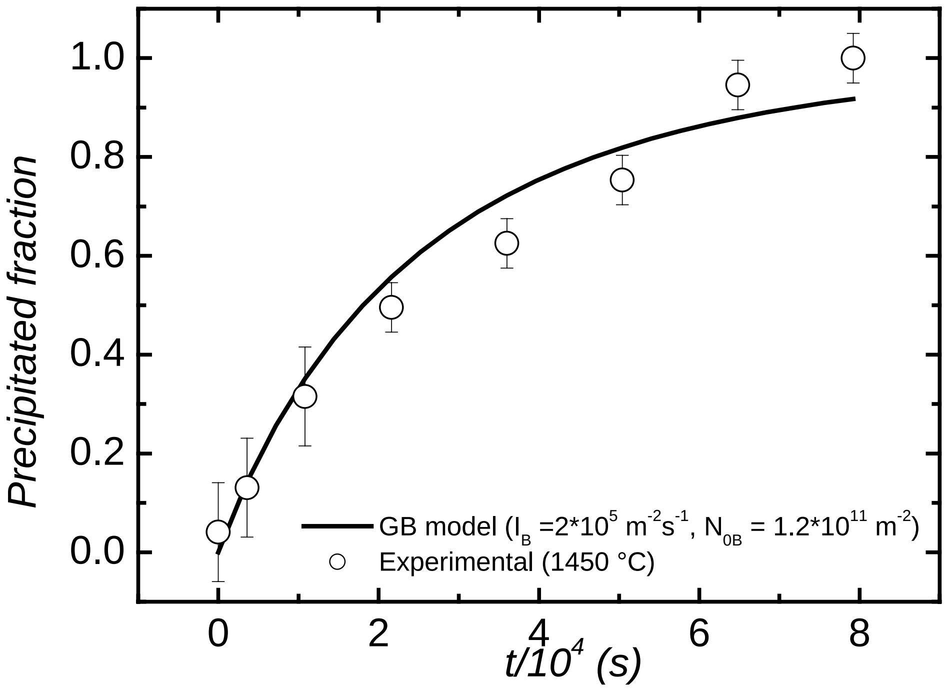

Fig. 6.65: *Time dependent precipitation kinetics of the sample A352 compared with the GB model. The best fit corresponds to the cases* $N_{0B} > I_B t$ *or* $N_{0B} = I_B t$.

7 Appendixes

7.1 Modelling of diffusion controlled precipitation with soft impingement

In this model, the influence of the soft impingement on the growth rate is investigated, i.e. the decrease in the growth rate due to overlapping between the diffusion fields of two adjacent particles. In the earlier stages of the transformation it is assumed that, after formation, the emerging nuclei are surrounded by the supersaturated matrix, but when local equilibrium is reached at the interface diffusion of the atoms becomes the limiting grain growth mechanism, i.e. there is an initial growth-transient for each individual grain, in which the steady state regime (local equilibrium between the emerging nuclei and the surrounded matrix) is established. During this growth–transient, the diffusion plays a preponderant role so that the growth rate can be given by equation (4.18). More details on this model can be found in [Cre96], [Cre97].

In the case of a variation of the matrix concentration, it is important to determine the time-evolution of this concentration. For this purpose, the mass balance between the emerging grain and the matrix can be used:

$$\gamma X(t)C_p + (1-\gamma X(t))C = C_0 \tag{7.1}$$

where γ is the volume fraction available for the growth of primary crystals at temperature T or, in other words, the crystallised fraction at the end of the primary crystallisation (*X(t) = 1*). Γ is defined as follows:

$$\gamma(T) = \frac{V^e(t \to \infty, T)}{V_0} \tag{7.2}$$

Imposing that $C(\to \infty) = C_s$, equation (7.1) becomes the lever rule

$$\frac{\gamma}{1-\gamma} = \frac{C_s - C_0}{C_0 - C_p}. \tag{7.3}$$

Finally, substituting equation (7.3) into equation (4.18), one obtains the new form of the growth rate:

$$\frac{dR}{dt} = \frac{D_0(T)}{R}\psi(X(t)), \tag{7.4}$$

where

$$D_0(T) = \frac{D(T)(C_S - C_0)}{C_S - C_p} = \gamma D(T) \tag{7.5}$$

It is important to note that we have the hard impingement, i.e. classical diffusion controlled growth, if $\psi(X(t)) = 1$, and for the soft impingement this function becomes:

$$\psi(X(t)) = \frac{1 - X(t)}{1 - \gamma X(t)} \tag{7.6}$$

Following the derivation procedure of the JMAK equation explained in paragraph 4.2.1, a non-linear Volterra integral equation of second kind is obtained for the three-dimensional diffusion controlled growth,

$$X(T,t) = 1 - \exp\left[-\frac{4\pi}{3} I_0(T)(2\gamma D(T))^{\frac{3}{2}} \int_0^t \exp[-k_N \tau]\left[\int_\tau^t \psi(X(\xi))d\xi\right]^{\frac{3}{2}} d\tau \right] \tag{7.7}$$

In the case of two dimensional diffusion controlled growth, cylindrical particles can be assumed. Under the condition of a radial growth, a similar integral equation can be obtained.

$$X(T,t) = 1 - \exp\left[-2\pi h I_0(T)(2\gamma D(T)) \int_0^t \exp[-k_N \tau]\left[\int_\tau^t \psi(X(\xi))d\xi\right] d\tau \right] \tag{7.8}$$

The integral equation (7.8) can be easily transformed into the following simple form with the corresponding initial condition,

$$\begin{cases} 1 - X(t) = \exp\left[-\int\limits_a^t K(t,s,X(s))ds \right] \\ a = 0, f(a) = 0 \end{cases} \tag{7.9}$$

The simple procedure to solve equation (7.90 is to establish a grid for the time axis with t_1, $t_2 \ldots t_N$ which has a constant step width *m*, so that $t_i = s_i = a + im$, where i = 1, 2, 3,…N is an integer. For a uniform mesh the simplest scheme is the trapezoidal approximation [Wil92] leading to

$$(I - X_i) = (I - X(t_i)) = \exp\left[-\sum_{j=1}^{i} \int\limits_{t_{j-1}}^{t_j} K(t_i, s, X)ds \right] \approx \exp\left[-\frac{1}{2} m \sum_{j=1}^{i} \left(K_{i,j-1} + K_{i,j}\right) \right], \tag{7.10}$$

where $K_{i,j} = K(t_i, s_j, X_j)$.

The summation in equation (7.10) leads to a discrete value of the crystallised fraction X_i at time t_i.

$$X_i = I - \exp\left[-m\left(\frac{1}{2} K_{i,0} + \sum_{j=1}^{i-1} K_{i,j} + \frac{1}{2} K_{i,i} \right) \right], \tag{7.11}$$

where *I* is the unit vector.

During the calculation process some considerations have to be made. For instance $X(t_i) = X_i$ and, consequently, $\psi(X_i)$ must be considered as slowly varying variables. Therefore their variation during the integration step is neglected so that the integral $\int_{\tau}^{t} \psi(X(\xi))d\xi$ can be recomputed at each iteration. If we interpret equation (7.8) as a vector equation of m functions $X(T,t)$, then the kernel $K(t,s,f(s))$ is a $m \times m$ matrix. For each *i* we have to solve the $m \times m$ set of non-linear equations. The computational solution of the system was carried out using the Newton-Raphson method, which is implemented in the *mathematica computational software* by *Findroot* [Wol91]. It is important to note that this numerical analysis can be extended to more or less complicated integral equations just by changing the analytical form of the kernel $K(t,s,X(s))$. For example, the linear kernel $K(t,s)$ where the function X(t) does not appear in the integral, is consistent with the classical form of the Avrami equation and can be numerically solved following the same procedure. Fig. 7.1, Fig. 7.2 and Fig. 7.3 show some examples of the crystallisation kinetics, the time dependence of the local JMAK exponent and of the JMAK plots. Fig. 7.2 clearly shows the constancy of the Avrami exponent in the case of the hard impingement. For other cases, a variation (decrease or increase) is observed.

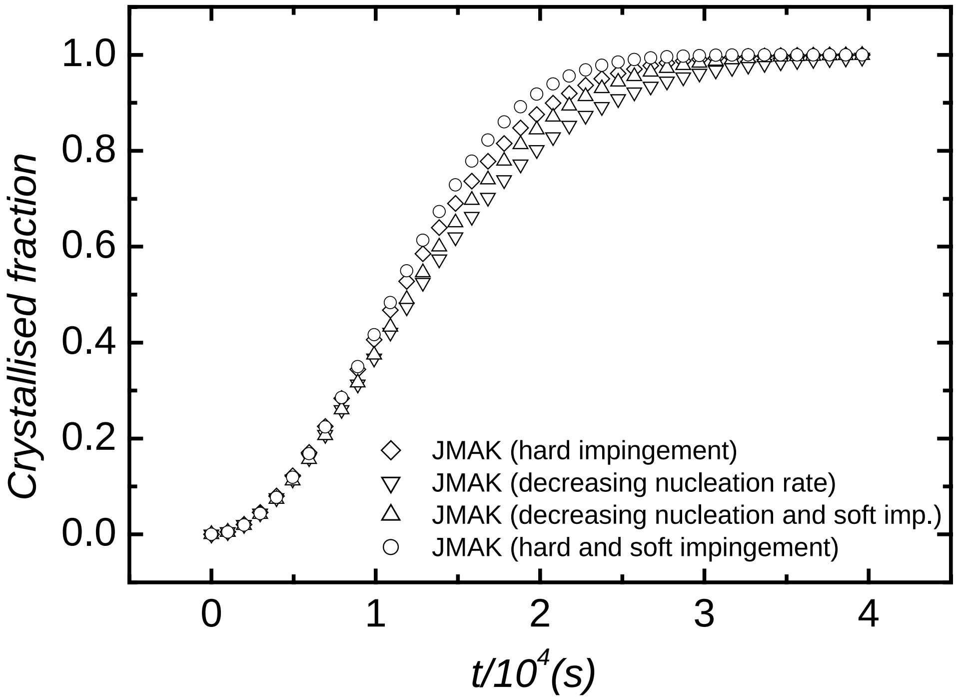

Fig.7.1: *Simulation of the time dependent crystallisation kinetics of the two-dimensional growth controlled by diffusion.*

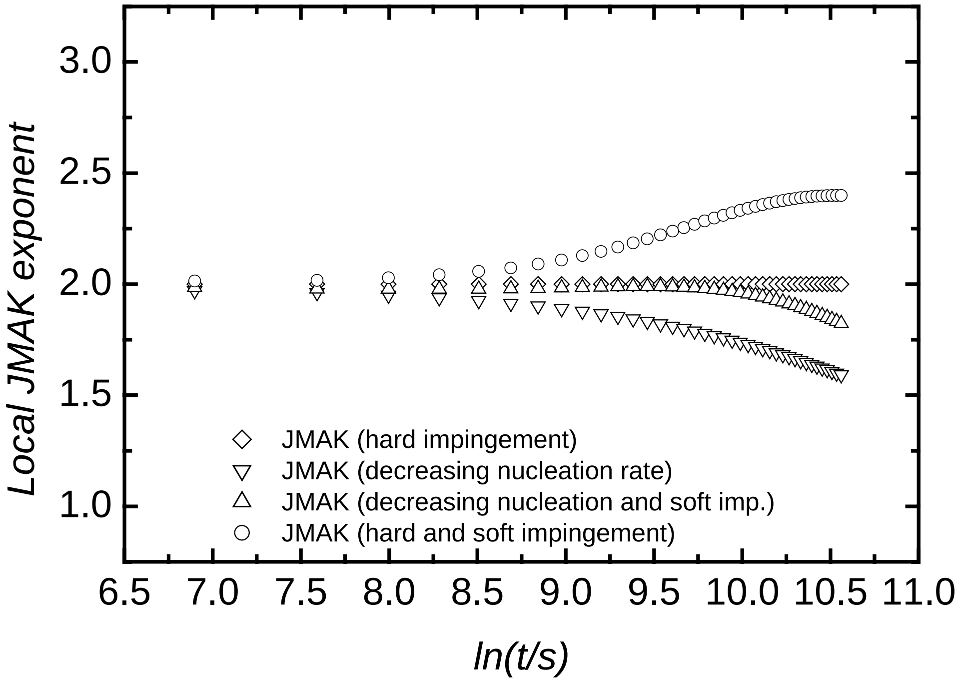

Fig. 7.2: *Two-dimensional diffusion controlled growth: Simulation of the local JMAK exponent.*

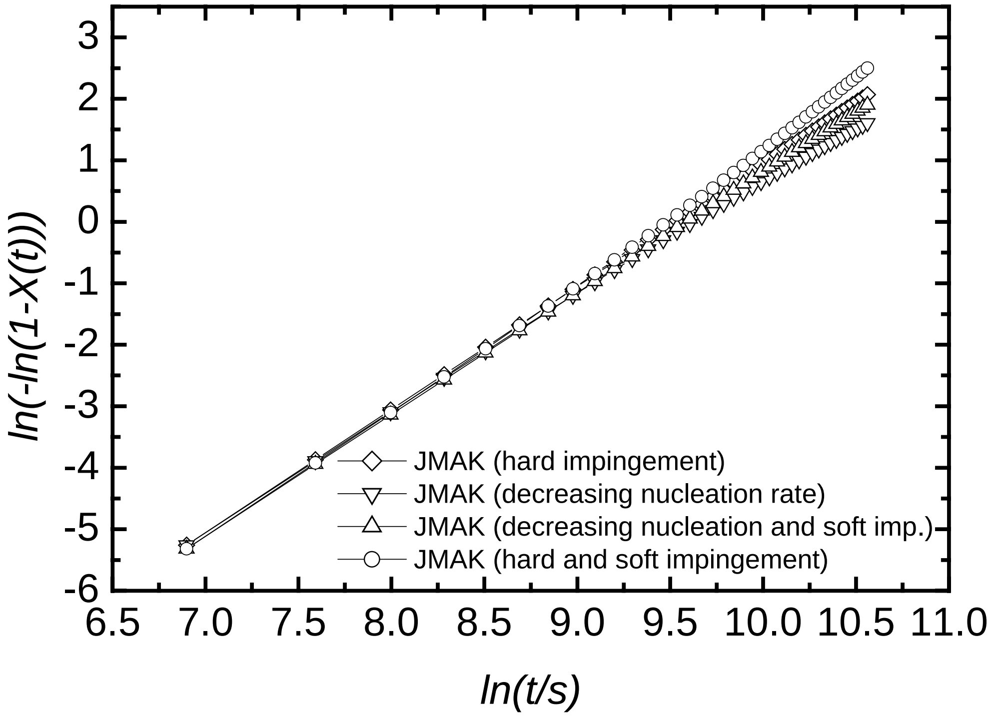

Fig. 7.3: *Two-dimensional diffusion controlled growth: Simulation of the JMAK plots.*

7. 2 Modelling of three-dimensional heterogeneous nucleation and growth

Considering a spherical precipitate of radius R growing because of both bulk diffusion and boundary diffusion, the stationary flux of atoms to this precipitate from the bulk is [Bak02]

$$J_V = D_V \frac{C_m - C_s}{R}, \tag{7.12}$$

where D_V is the diffusion coefficient of atoms in the volume and C_m and C_s are the mean concentrations in the matrix and at the precipitate-matrix interface, respectively.

An identical equation is given for the flux of atoms from the grain boundaries

$$J_B = D_B \frac{C_m - C_s}{R}, \tag{7.13}$$

where D_B is the diffusion coefficient in the grain boundaries.

The integral flux to the precipitate is defined by

$$J = 4\pi R^2 J_V + 2\pi a R J_B \tag{7.14}$$

where *a* is the width of the grain boundary in the order of about one interatomic spacing.

The law of mass conservation gives the equation of the precipitate volume growth due to diffusion.

$$J = \left(C_P - C_S\right)4\pi R^2 \frac{dR}{dt}, \tag{7.15}$$

where C_P is the concentration of the equilibrium components in the precipitate.

Combining equations (7.14)-(7.15) the expression for precipitate growth is given by

$$\frac{dR}{dt} = \left(\frac{D_V}{R} + \frac{aD_B}{2R^2}\right)\frac{C_m - C_s}{C_P - C_s} \tag{7.16}$$

The solution of equation (7.16) leads to the following expression for the time dependence of the radius of the precipitate nucleated at the moment τ

$$R(t,\tau)\left(R(t,\tau) - 2L\right) + 2L^2 \ln\left(1 + \frac{R(t,\tau)}{L}\right) = \alpha\left(t - \tau\right), \tag{7.17}$$

where

$$\alpha = \frac{2D_V\left(C_m - C_s\right)}{C_P - C_s} \tag{7.18}$$

and the parameter $\frac{2L}{a}$ gives the relation between the boundary and the volume diffusivity:

$$\frac{2L}{a} = \frac{D_B}{D_V} \tag{7.19}$$

The expression of the transformed volume fraction can be given using the JMAK approach and by taking into account the grain boundary contribution. It follows,

$$X(t) = 1 - \exp\left[\left(1 - a\rho_B\right)Y_V(t) - \rho_B Y_B(t)\right], \tag{7.20}$$

Using the concept of Cahn [Cah56] for the derivation of rate laws for transformations in which new phases nucleate at grain boundaries, considering that the set of all intersections represented a two dimensional Boolean model [Bak02], the total contribution of the boundaries to the crystallized volume fraction is defined by

$$Y_B(t) = 2\int_0^{R(t,0)} \left\{1 - \exp\left[-\pi Z\left(R(t,0), y\right)\right]\right\} dy \tag{7.21}$$

where R(t, 0) is the maximum radius in the system and the function *Z(R,y)* has the form:

$$Z(R,y) = N_{0B}\left(R^2 - y^2\right) + \frac{2}{\alpha}\int_y^R \frac{I(R')\left(R'^2 - y^2\right)}{R' + L} R'^2 \, dR' \tag{7.22}$$

If the nucleation rate is assumed to be not dependent on time, i.e. $I_B(t) = I_B$, the integral in equation (7.22) can be expressed directly and the function *Z(R, y)* is given by

$$Z(R,y) = N_{0B}\left(R^2 - y^2\right) + \frac{I_B}{\alpha}\left\{\frac{1}{2}\left(R^4 - y^4\right) - \frac{2}{3}L\left(R^3 - y^3\right) + \left(L^2 - y^2\right)\left[\varphi(R) - \varphi(y)\right]\right\} \tag{7.23}$$

Equation (8.20) gives the total volume fraction and the combination of equations (7.21)-(7.23) allows to find the dependence of the total volume fraction on time. Fig. 7.4, Fig. 7.5 and Fig.

7.6 show the precipitation kinetics, the variation of the local JMAK exponent and the corresponding JMAK plots.

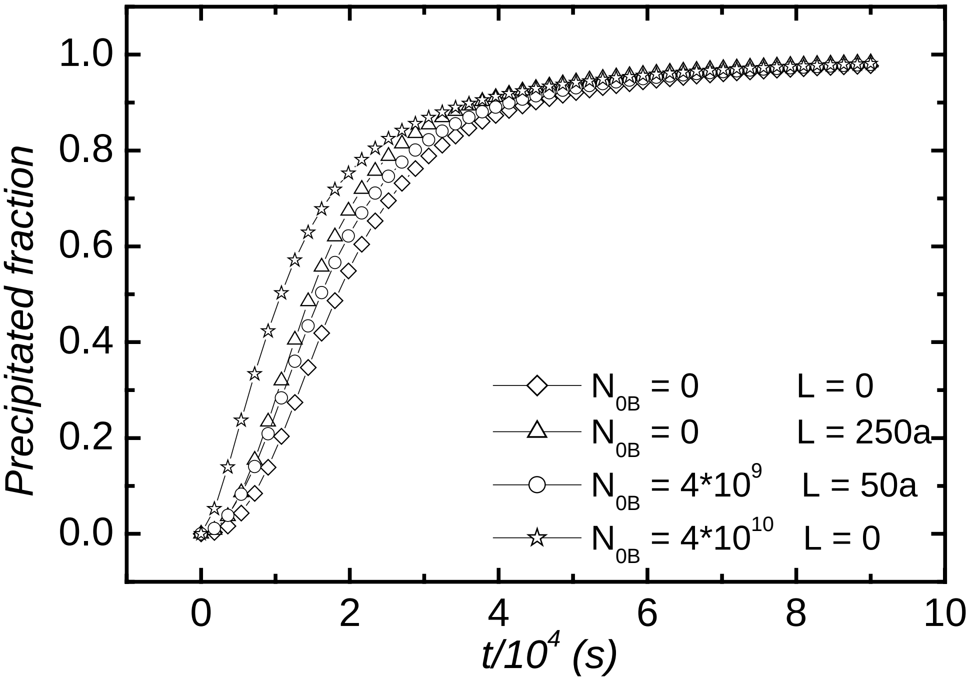

Fig. 7.4: *Three-dimensional growth with contribution of grain boundaries: Simulation of the time dependent precipitation kinetics* ($I_B = 3x10^6$ $m^{-2}s^{-1}$).

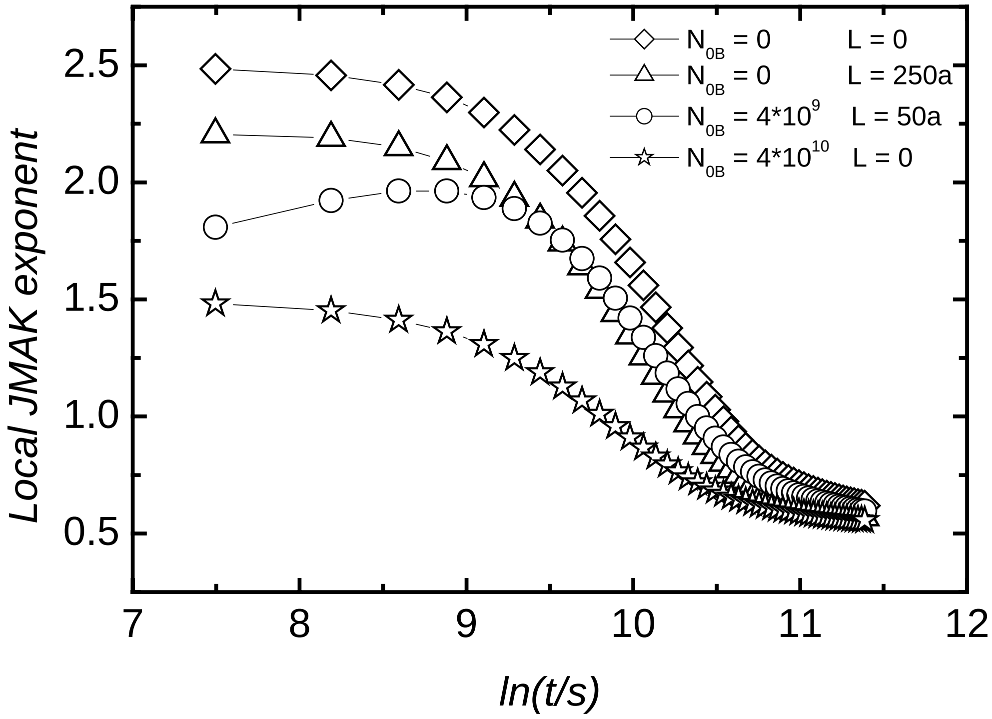

Fig. 7.5: *Three-dimensional growth with contribution of grain boundaries: Simulation of the local JMAK exponent (I_B = $3x10^6$ $m^{-2}s^{-1}$). The values of the JMAK exponent range between 2.5 and 0.5. The first value corresponds to the three-dimensional diffusion controlled growth with constant nucleation rate, the second one to one-dimensional diffusion growth with pre-existing nuclei and soft impingement of the growing particles.*

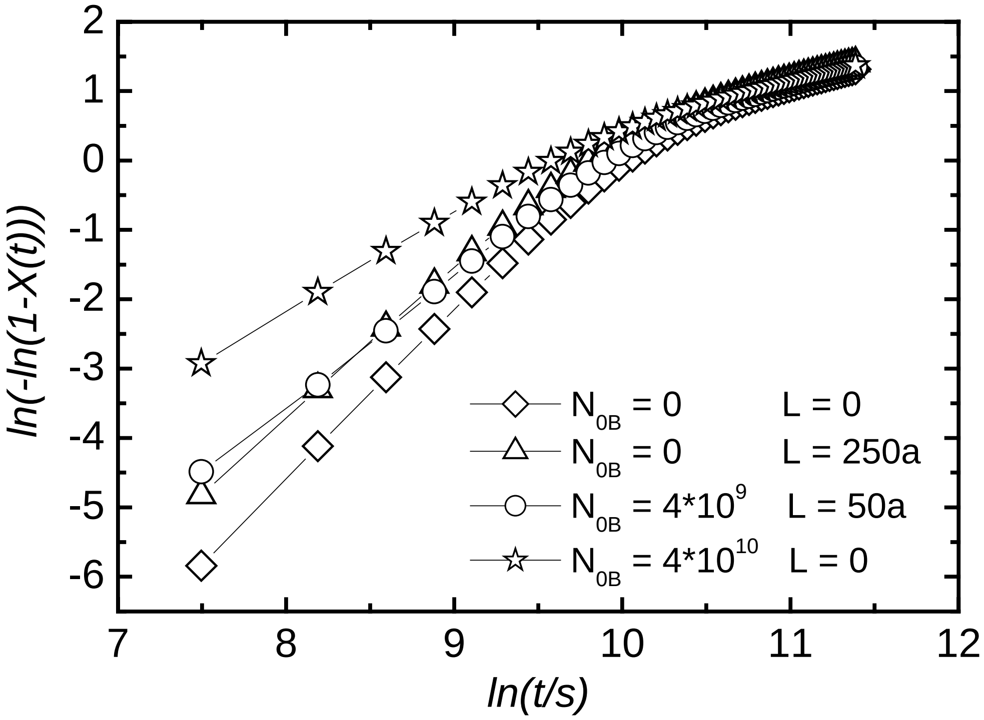

Fig. 7.6: *Three-dimensional growth with contribution of grain boundaries: Simulation of the JMAK plots ($I_B = 3x10^6\ m^{-2}s^{-1}$). The non-linearity of the JMAK plots due to heterogeneous nucleation can be observed.*

7.3 Pre-existing nuclei and estimation of the relative error for amorphous SiC films

Following the derivation procedure of the JMAK equation in the case of the three-dimensional interface controlled growth, one can write the crystallised fraction in the case of the growth of pre-existing nuclei in the following form:

$$X(t) = 1 - \exp\left(-\frac{4\pi N_0}{3} R^3\right) \tag{7.24}$$

where R is the time dependence radius of the growing particles and N_0 the density of the pre-existing nuclei. This equation enables the determination of N_0, knowing the crystallised fraction and the radius.

$$N_0 = \frac{-3\ln(1 - X(t))}{4\pi R^3} \tag{7.24a}$$

Taking the logarithmic form of equation (7.24a) one obtains

$$\ln\left(-\ln(1-X)\right) = \ln N_0 + 3\ln R + \ln\frac{4\pi}{3} \tag{7.25}$$

The differentiation of equation (7.25) leads to

$$\frac{dX}{(1-X)\ln(1-X)} = \frac{dN_0}{N_0} + 3\frac{dR}{R} \tag{7.26}$$

The radius $R = \frac{d}{2}$ is related to the Bragg angle via the equation of Scherrer ($d = \frac{0.9\lambda}{F\cos\theta}$) where F is the full width at half maximum. The differentiation of this equation leads to

$$\frac{d(d)}{d} = -\frac{dF}{F} + \tan\theta d\theta \tag{7.27}$$

Introducing equation (7.27) in equation (7.26) and substituting all differentials by differences one obtains the expression of the relative error made on the density of the pre-existing nuclei

$$\frac{\Delta N_0}{N_0} = \frac{\Delta X}{\left|(1-X)\ln(1-X)\right|} + 3\left(\frac{\Delta F}{F\Delta\theta} + \tan\theta\right)\Delta\theta \tag{7.28}$$

For this analysis we took ΔX = 0.1 and Δθ = 0.05 °.

Table 7.1: *Density of pre-existing nuclei of the amorphous SiC films deposited on crystalline silicon and annealed at 1250 °C.*

Time (s)	N_0 (10^{22} m^{-3})	Relative error (%)
10800	1.46	87.5
16800	4.58	71.21
21600	8.43	42.7
26400	1.19	32.9
31200	1.75	31.1
38400	1.92	30.8
67200	2.95	44.13
8160	2.98	45.8

Table 7.2: *Density of pre-existing nuclei of the amorphous $Si_{0.33}C_{0.67}$ films deposited on crystalline silicon.*

Time (s)	N_0 (10^{22} m^{-3})	Relative error (%)
3600	4.49	72.3
7200	3.8	54.35
14400	1.25	57.1
25200	0.86	42.04
39600	4.68	39.15
64800	3.1	42.7
86400	4.06	75.41

7.4 Additional figures

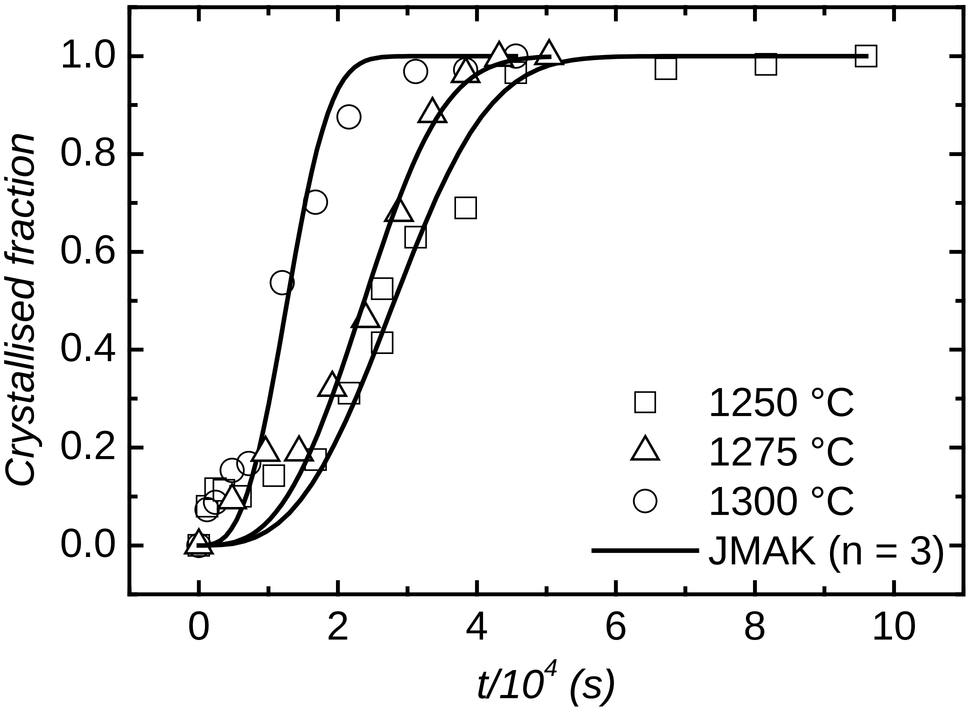

Fig. 7.7: *Time evolution of the crystallised fraction of the films deposited on a silicon substrate and annealed at different temperatures. The solid line corresponds to the fit with the JMAK model.*

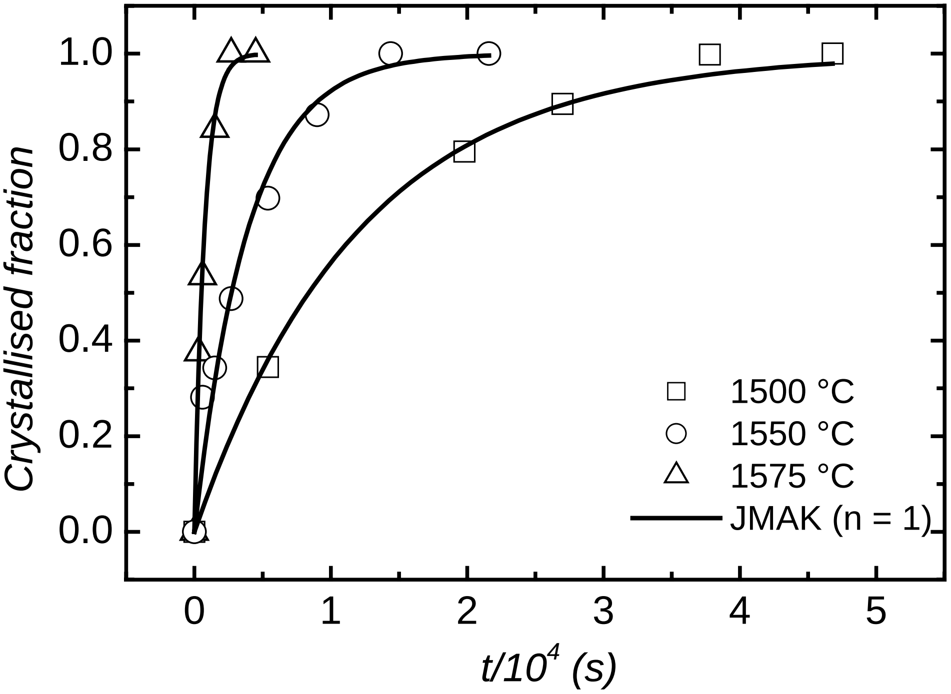

Fig. 7.8: *Time evolution of the crystallised fraction of the films deposited on a glassy carbon substrate and annealed at different temperatures. The solid line corresponds to the fit with the JMAK model.*

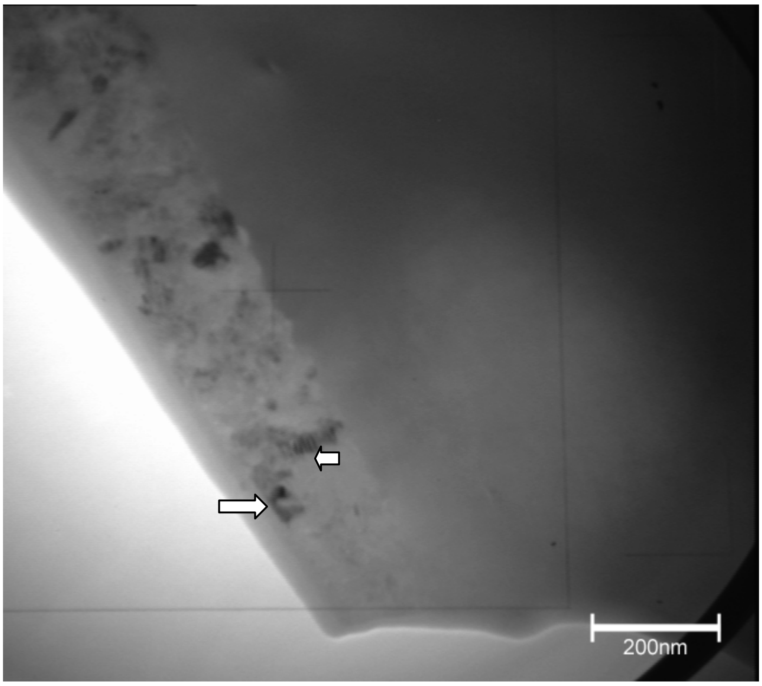

Fig. 7.9: *TEM micrograph: Bright field image of the film deposited on a silicon substrate and annealed at 1275 °C. Crystallites are indicated with arrows.*

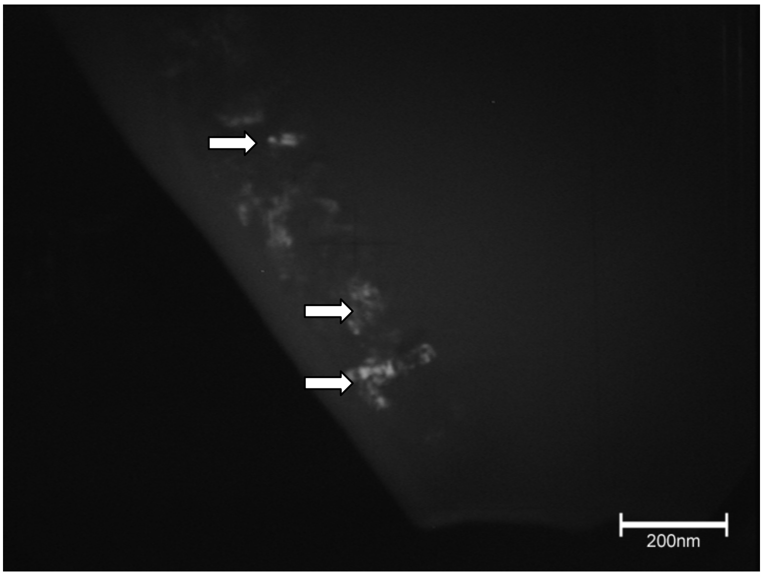

Fig. 7.10: *TEM micrograph: Dark field image of the film deposited on a silicon substrate and annealed at 1275 °C. Crystallites are indicated with arrows.*

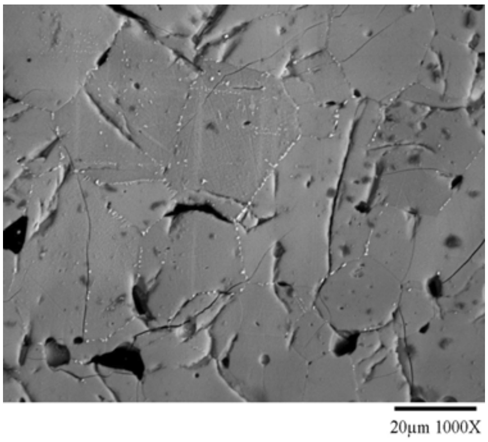

1h30

Fig. 7.11a*: Precipitation at grain boundaries.*

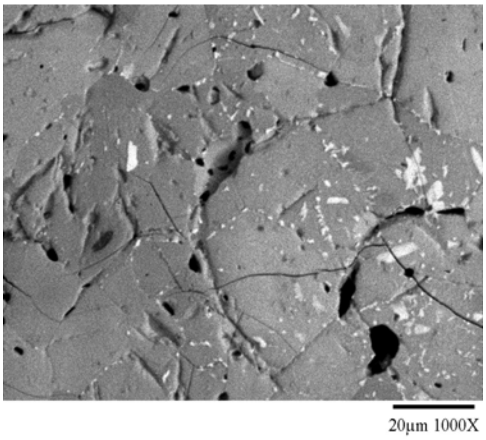

3h15

Fig. 7.11b*: Progression of the precipitation at the grain boundaries.*

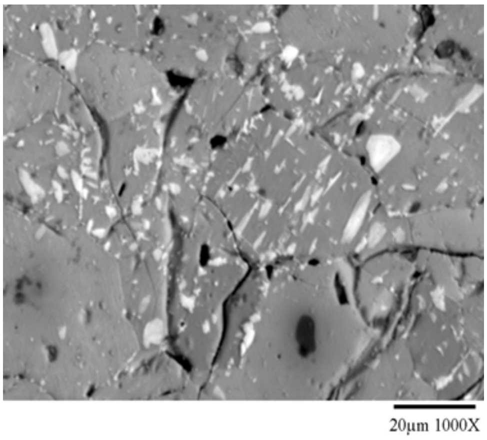

12h30

Fig. 7.11c: *Growth at grain boundaries and in the interior of the grain.*

Fig. 7.11: *Illustration of the precipitation mechanism in diboride-based materials. Sample annealed at 1525 °C.*

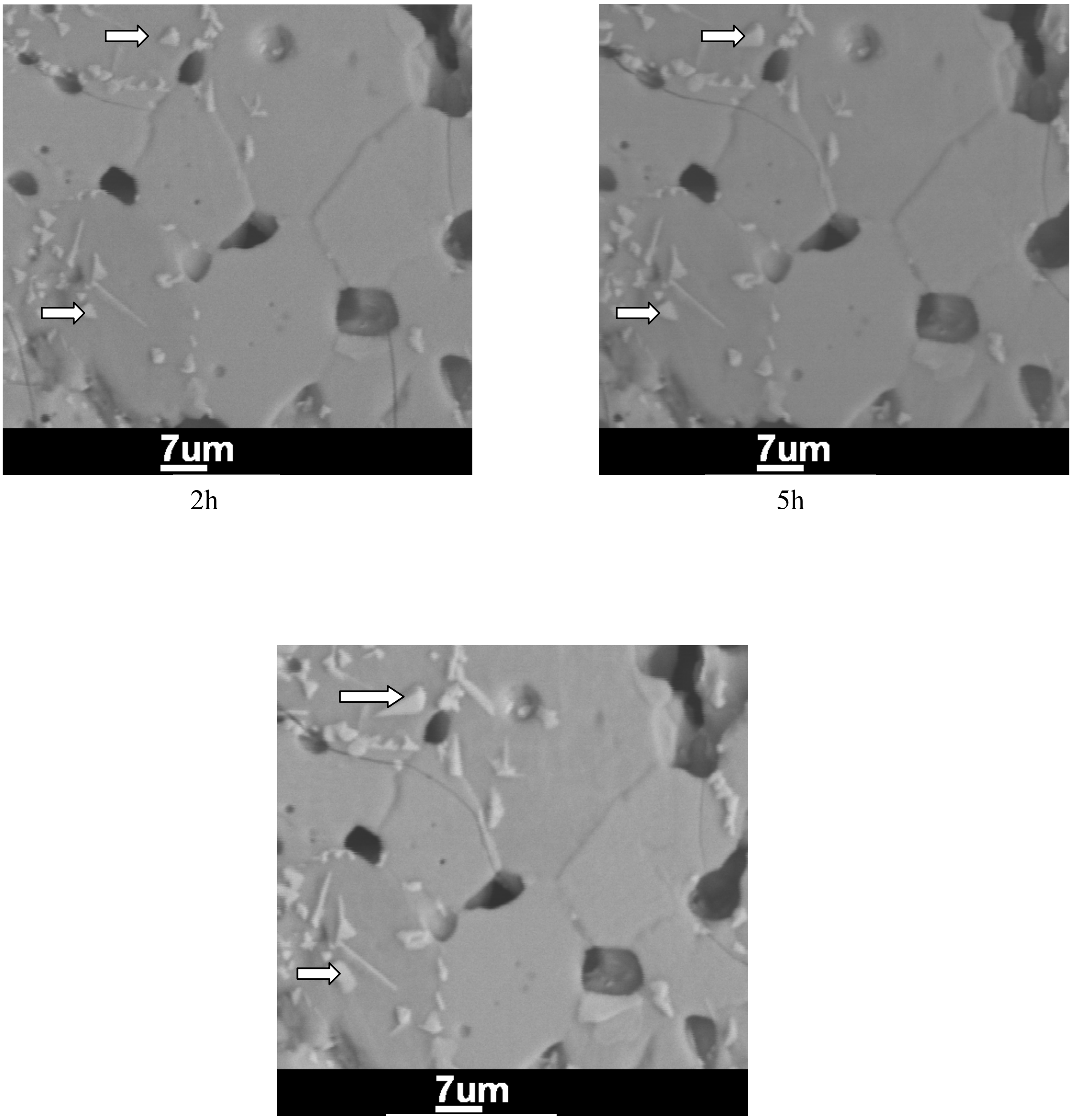

2h

5h

9h

Fig. 7.12: *Growth of W_2B_5 platelets of the sample B325 annealed at 1575 °C. The arrows indicated the growth of the precipitates with the annealing time.*

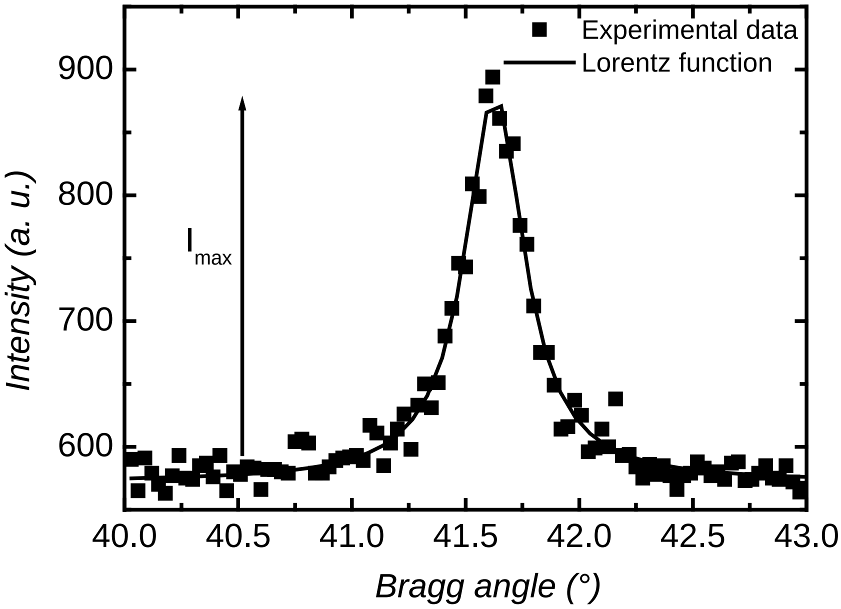

Fig. 7.13: *Illustration of the determination of the precipitated or crystallised fraction using the Lorentz function. The crystallised fraction corresponds to the surface between the Lorentz function and the Bragg angle axis.*

8 List of tables

9 List of figures

10 References

[Ame97] S. Amelinckx, D. van Dyck, J. Van Landuyt, G. van Tendeloo, Handbook of Microscopy: Applications in Materials Science, Solid-State Physics, and Chemistry. VCH Weinheim (Germany) 1997.

[Avr39] M. Avrami, "Kinetics of phase change I", J. Chem. Phys. 7 (1939) 1103.

[Avr40] M. Avrami, "Kinetics of phase change II", J. Chem. Phys. 8 (1940) 212.

[Avr41] M. Avrami, "Kinetics of phase change III", J. Chem. Phys. 9 (1941) 177.

[Bak02] A. S Bakai, H. Hermann, N. P. Lazarev, "Diffusion limited crystallisation of heterogeneous glasses", Phil. Mag. A 82 (8) (2002) 1521.

[Bil00] J. Bill, J. Schumacher, K. Müller, S. Schemp, J. Seitz; J. Dürr, H.-P. Lamparter, J. Golczewski, J. Peng, H. J. Seifert, F. Aldinger, "Investigations into the structural evolution of amorphous Si-C-N ceramics from precursors", Z. Metallkd. 91 (2000) 335.

[Blu72] N. A. Blum, C. Feldman, "The crystallisation of amorphous silicon films", J. Non-Cryst. Solids 11 (1972) 242.

[Bre55] L. Brewer, H. Haraldsen, " The thermodynamic stability of refractory borides", J. Electrochem. Soc. 102 (7) (1955) 399.

[Cal01] L. Calgano, P. Musumeci, F. Roccaforte, C. Buongiorno, G. Foti, "Crystallisation mechanism of amorphous silicon carbide", Appl. Surf. Sci. 184 (2001) 123.

[Cal02] L. Calgano, P. Musumeci, F. Roccaforte, C. Bongiorno, G. Foti, "Crystallisation process of amorphous silicon –carbon alloys", Thin Solid Films 411 (2002) 298.

[Cah56] J. W. Cahn, "The kinetics of grain boundary nucleated reactions", Act. Metall. 4 (1956) 449.

[Cah57] J. W. Cahn, "Nucleation on dislocations", Act. Metall. 5 (1957) 169.

[Cah99] J. W. Cahn, Challenge of Paradigm Building for Solid-State Transformation. In PTM'99, 1999, Kyoto, The Japan Institute of Metals, p. 3-14.

[Cai01] Y. Cai, A. Zimmermann, S. Prinz, A. Zern, F. Phillipp and F. Aldinger, "Nucleation phenomena of nano-crystallites in as-pyrolysed Si-B-C-N ceramics", Scripta Mater. 45 (2001) 1301.

[Cal88] A. Calka, A. P. Radlinski, "The effect of surface on the kinetics of crystallisation of $Pd_{85}Si_{15}$ glassy metallic alloys: description of isothermal crystallisation by local value of the Avrami exponent", J. Mater. Res. 3(1) (1988) 59.

[Cas77] Castaing, J. P. Costa, "Properties and use of diborides", in: Boron and Refractory borides, ed. Matkovich (1977) 19-30.

[Chr75] J.W. Christian, “The theory of transformation in metals and alloys”, Pergamon Press, Oxford, (1975).

[Clu03] D. C. Clupper, L. L. Hench, “ Crystallisation kinetics of tape cast bioactive glass 45S5”, J. Non-Cryst. Solids. 318 (2003) 43.

[Cre96] D. Crespo, T. Pradell, “Evolution of time-dependent grain-size populations for nucleation and growth kinetics”, Phys. Rev. B 54(5) (1996) 3101.

[Cre97] D. Crespo, T. Pradell, M. T. Clavaguera-Mora, N. Clavaguera, “Microstructural evaluation of the primary crystallisation with diffusion-controlled grain growth”, Phys. Rev. B 55(6) (1997) 3435.

[Dav93] R. F. Davis, “ Silicon carbide and diamond semiconductor thin films: growth, defect analysis, and device development”, Am. Ceram. Soc. Bul. 72 (1993) 99.

[Ell65] R. P. Elliot, in Constitution of binary alloys, first supplement, MacGraw Hill: New York (1965), P. 227-229.

[Fab83] K. T. Faber, A. G. Evans, “Crack deflection processes-I. Theory & II. Experiments”, Acta Metall. 31(4) (1983) 565 and 577

[Fen01] E. Fenard, M. Desmaison-Brut, T. Joyeux, “Interfacial reactions between titanium nitride-titanium diboride ceramics and nickel”, Key. Eng. Mater. 206-213 (2001) 563.

[Fuy89] T. Fuyuki, M. Nakayama, T. Yoshinobu, H. Shiomi, H. Matsunami, “Atomic layer epitaxy of cubic SiC by gas source MBE using surface superstructure”, J. Cryst. Growth 95 (1989) 461.

[Goe83] U. Gosele, T. Y. Tan, in: S. Mahajan, Defects in semiconductors, North-Holland, New York, 1983, p. 45.

[Gos91] G. Ghosh, M. Chandrasekaran, L. Delaey, “Isothermal crystallisation kinetics of $Ni_{24}Zr_{76}$ and $Ni_{24}(Zr\text{-}X)_{76}$ amorphous alloys”, Acta Metall. 39 (1991) 925.

[Gre82] A. L. Greer, “Crystallisation kinetics of $Fe_{80}B_{20}$ glass”, Acta Metall. 30 (1982) 171.

[Ham88] Y. Hamkawa, D. Kruangam, M. Deguchi, Y. Hattori, T. Toyama, H. Okamoto, “Visible light thin film LED made by a-SiC p-i-n junction”, Appl. Surf. Sci. 33-34 (1988) 1142.

[Hee97] V. Heera, F. Probert, N. Schell, H. Seifarth, W. Kukarek, M. Volskow, W. Skorupa, Density and structural changes in SiC after amorphization and annealing, Appl. Phys. Lett., 70 (1997) 3531.

[Hei96] D. Heimann, “Oxydationsschutzschichten für kohlefaserverstärkte Verbundwerkstoffe durch Polymer-Pyrolyse“, in Jahrbuch des Max-Planck-Instituts für Metallforschung. 1996, Universität Stuttgart: p. 215.

[Hei97] D. Heimann, “Epitaxial growth of ß-SiC thin films on 6H-SiC substrate using the chemical solution deposition method”, J. Mater. Res. 12(11) (1997) 3099.

[Her97] H. Hermann, N. Mattern, S. Roth, P. Uebele, “Simulation of crystallisation processes in amorphous iron-based alloys”, Phys. Rev. B 56(21) (1997) 13888.

[His01] H. Kaga, E. M. Heian, Z. A. Munir, “Synthesis of hard materials by field activation: the synthesis of solid solutions and composites in the TiB_2-WB_2-CrB_2 system”, J. Am. Ceram. Soc. 84(12) (2001) 2764.

[Hof96] F. Hofer, P. Warbichler, B. Buchmayer, S. Kleber, “On the detection of MX-precipitates in micro-alloy steels using energy-filtering TEM, J. Microsc. 184 (1996) 163.

[Hol91] J. C. Holzer, K. F. Kelton, “Kinetics of the amorphous to icosahedral phase transformation in Al-Cu-V alloys“, Acta Metall. 39 (1991) 1833.

[Hon80] J. D. Hong, R. F. Davis, “Self-diffusion of carbon-14 in high purity and N-doped α-SiC single crystals”, J. Am. Ceram. Soc. 63 (1980) 546.

[Hon81] J. D. Hong, R. F. Davis, D. E: Newbury, “Self-diffusion of silicon-30 in α-SiC single crystals”, J. Mater. Sci. 16 (1981) 2485.

[Ino87] S. Inoue K. Yoshi, M. Umeno and H. Kawabe, “Crystallisation behaviour of amorphous SiC films prepared by r.f. sputtering”, Thin Solid Films 151 (1987) 403.

[Joh39] A. M Johnson, R. F. Mehl, “Reaction kinetics in processes of nucleation and growth”, Trans. Am. Inst. Min. Engrs. 135 (1939) 416

[Jue91] T. Jueling, R. Oberacker, F. Thuemmler, L. Sigi, K. A. Schmetz, “Pressureless sintering of TiB_2-Fe materials”, Powder Metall. Int. 23 (1991) 296.

[Kel85] K. F. Kelton, F. Speapen, “A study of the devitrification of $Pd_{82}Si_{18}$ over a wide temperature range“, Acta Metall. 33 (1985) 455.

[Kem01] A. T. W. Kempen, “Solid State Phase Transformation Kinetics”, PhD thesis, Universität Stuttgart (2001).

[Kie50] R. Kiessling, “The borides of some transition elements”, Act. Chem. Scand. 4 (1950) 209.

[Kin75] W. D. Kingery, H. K. Bowen, D. R. Uhlmann, “Introduction to ceramics”, second edition, John Wiley & Sons, New York (1975).

[Kis57] H. E. Kissinger, “Variation of the peak temperature with heating rate in differential thermal analysis”, J. Res. NBS 57 (1957) 217.

[Kis57] H. E. Kissinger, “Reaction kinetics in differential thermal analysis”, Anal. Chem. 29 (1957) 1702.

[Kle90] Kleber, I., H.-J. Bautsch, and J. Bohm, Einführung in die Kristallographie. 17 ed. 1990, Berlin: Verlag Technik GmbH, p.152ff.

[Kle01] I. Kleps, A. Angelescu, “Correlation between properties and application of the CVD amorphous silicon carbide films”, Appl. Surf. Sci. 184 (2001) 107.

[Klu74] H. P. Klug, L. E. Alexander, X-ray procedures for polycrystalline and amorphous materials, (Wiley and Sons, New York, 1974).

[Kra96] W. Kraus, G. Nolze, “POWDER CELL - a program for the representation and manipulation of crystal structures and calculation of the resulting X-ray powder patterns”, J. Appl. Crystallogr. 29 (1996) 301.

[Krü93] P. Krüger, “On the relation between non-isothermal and isothermal Kolmogorov-Johnson-Mehl-Avrami crystallisation kinetics”, J. Phys. Chem. Solids 54(11) (1993) 1549.

[Kur99] D. Kurtenbach, B. S. Mitchell, H. Zhang, M. Ade, E. Müller, “Crystallisation kinetics of amorphous silicon carbide derived from polymeric precursors”, Thermochim. Acta 337 (1999) 155.

[Kuz69] Y. B. Kuz’ma, S. I. Svarichevskaya, V. S. Telegus, “Systems Ti-W-B, Hf-Ta-B and Ta-W-B”, Transl. Poroshk. Metallurgya 6(1029) (1969) 61.

[Lee90] E.-S. Lee, Y. G. Kim, “A transformation kinetic model and its application to Cu-Zn-Al shape memory alloys-I. Isothermal conditions”, Acta Metall. Mater. 38 (1990) 1669.

[Lev97] L. E. Levine, K. Lakshmi, K. F. Kelton, “Finite size corrections for the Johnson-Mehl-Avrami-Kolmogorov equation”, J. Mater. Res. 12(1) (1997) 124.

[Lia94] J. M. Liang, L. J. Chen, I. Markov, “Crystallisation of amorphous $CoSi_2$ thin films I. Kinetics of nucleation and growth”, Mat. Chem. Phys. 38 (1994) 250.

[Lun68] T. Lundström, “The structure of Ru_2B_3 and WB_2 as determined by single crystal diffractometry, and some notes on the W-B system”, Arkiv för Kemi 30(11) (1968) 115.

[Lut98] H. Lutz, M. Bruns, F. Link, H. Baumann, “Surface- and microanalytical characterization of silicon-carbonitride thin films prepared by means of radio frequency magnetron co-sputtering”, Thin Solid Films 332 (1998) 230.

[Mad01] W. Mader, B. Freitag, K. Kelm, R. Telle, C. Schmalzried, “Combined HRTEM and EFTEM study of precipitates in tungsten and chromium-containing TiB_2”, Mat. Res. Soc. Symp. 595 (2001) 289.

[Mas03] M. Shibuya, T. Yomeda, Y. Yamamoto, M. Ohyanagi, Z. A. Munir, “Effect of Ni and Co additives on phase decomposition in TiB_2-WB_2 solid solution formed by induction field activated combustion synthesis”, J. Am. Ceram. Soc. 86(2) (2003) 354.

[Mas03] M. Shibuya, M. Kawata, M. Ohyanagi, Z. A. Munir, “Titanium diboride-tungsten diboride solid solution formed by induction-field-activated combustion synthesis”, J. Am. Ceram. Soc. 85(4) (2003) 706.

[Mit97] I. Mitra, R. Telle, “Phase formation during anneal of supersaturated TiB_2-CrB_2-WB_2 solid solutions”, J. Solid State Chem. 133 (1997) 25.

[Mit98] I. Mitra, “Gefügeentwicklung und Plättchenwachstum im System der Übergangsmetallboride TiB_2, W_2B_5 und CrB_2 zur Dispersionsverstärkung von Carbidkeramik“, PhD thesis, RWTH Aachen (1998).

[Nas82] T. S. Nashashibi, I. G. Austin, T. M. Searle, R. A. Gibson, W. E. Spear, P. G. LeComber, “Electroluminescence in amorphous silicon p-i-n junction”, Philos. Mag. B 45 (1982) 553.

[Nic92] M. M. Nicolaus, H.-R. Sinning, F. Hässner, “Crystallization behaviour and generation of nanocrystalline state from amorphous $Co_{33}Zr_{67}$” Mater. Sci. Eng. A 150 (1992) 101.

[Nis80] S. Nishino, Y. Hazuki, H. Matsunami, T. Tanaka, “Chemical vapour deposition of single crystalline ß-SiC films on silicon substrate with sputtered SiC intermediate layer”, J. Electrochem. Soc.127 (1980) 2674.

[Nis83] S. Nishino, J. A. Powell, H. A. Will, “ Production of large-area single crystal wafers of cubic SiC for semiconductors devices”, Appl. Phys. Lett. 42 (1983) 461.

[Ota95] S. Otani, H. Ohashi, Y. Ishizawa, “Lattice constants and nonstoichiometry of WB_{2-x}”, J. Alloys Compd. 221 L8-L10 (1995).

[Ota95] S. Otani, Y. Ishizawa, “Preparation of WB_{2-x} single crystals by floating zone method”, J. Cryst. Growth 154 (1995) 81.

[Oza71] T. Ozawa, “Kinetics of non-isothermal Crystallization”, Polymer 12 (1971) 150.

[Pal88] J. W. Palmour, K. Das, R. F. Davis, “Electrical properties of ion-implanted p-n junction diodes in ß-SiC”, J. Appl. Phys. 63 (1988) 922.

[Phi91] J. Philibert, Atom movements, (Les éditions de Physique, Les Ulis) (1991)

[Pin02] E. Pineda, T. Pradell, “Non-random nucleation and Avrami kinetics”, Philos. Mag. A 82(1) (2002) 107.

[Por81] D. A. Porter, K. E. Easterling, “Phase Transformation in Metals and Alloys”, Chapman and Hall, (1981), p. 189.

[Pos54] B. Post, F. W. Glaser, D. Moskowitz, “Transition metal diborides”, Acta Metall. 2(1) (1954) 20.

[Pow88] J. A. Powell, and L.G. Matus, “Recent developments in SiC”, Springer Proc. Phys. 34 (1989) 2.

[Pow92] J. A. Powell, “Progress in silicon carbide semiconductor technology”, Mat. Res. Soc. Symp. Proc. 242 (1992) 495.

[Pra98] T. Pradell, D. Crespo, N. Clavaguera, M. T. Clavaguera-Mora, “Diffusion controlled grain growth in primary crystallisation: Avrami exponents revisited”, J. Phys.: Condens. Matter 10 (1998) 3833.

[Rag81] S. Ranganathan, M. von Heimendahl, “The three activation energies with isothermal transformation: application to metallic glasses”, J. Mater. Sci. 16 (1981) 2401.

[Ram47] L. S. Ramsdell, “Studies on Silicon Carbide” Am. Mineral. 32 (1947) 64.

[Rau00] C. Rau “Untersuchung zur substratinduzierten Kristallisation amorpher SiC-Precursor-Keramiken“, PhD thesis, Universität Stuttgart (2000)

[Rei95] L. Reimer, “Energy Filtering Transmission Electron Microscopy”, Springer, Berlin, (1995).

[Rick38] J.B. Austin, R. I. Rickett, “Kinetics of the decomposition of austenite at constant temperature”, Trans. Am. Inst. Min. Engrs. 135 (1939) 396.

[Rie96] R. Riedel, “Advanced ceramics from inorganic polymers”, Mater. Sci. Technol. 17 B (1996) 1.

[Rie96] R. Riedel, A. Kienzle, W. Dressler, L. Ruwisch, J. Bill, F. Aldinger, “A silicoboron carbonitride ceramic stable to 2000 °C“, Nature 382 (1996) 796.

[Ruf94] M. Ruff, H. Mitlehner, R. Helbig, “SiC devices: Physics and numerical simulation”, IEEE Trans. Electron. Dev. 41 (1994) 1040.

[Sca60] R. I. Scace, G. A. Slack, Silicon carbide - A high temperature semiconductor, J. R. O’Connor, J. Smiltens (Eds.), (Pergamon Press, Oxford, London, New York, Paris) (1960) 24

[Sch01] C. Schmalzried, R. Telle, B. Freitag, W. Mader, “Solid state reactions in transition metal diboride-based materials”, Z. Metallkd. 92 (2001) 1197.

[Sch03] H. Schmidt, G. Borchardt, C. Schmalzried, R. Telle, H. Baumann, S. Weber, H. Scherrer, “Material transport in $(Ti_{0.3}W_{0.5}Cr_{0.2})B_2$ ceramics: simultaneous diffusion of ion implanted ^{49}Ti and ^{54}Cr”, J. Europ. Ceram. Soc. 23 (2003) 991.

[Sch04] H. Schmidt, G. Borchardt, M. Rudolphi, H. Baumann, M. Bruns, “Nitrogen self-diffusion in silicon nitride thin films probed with isotope heterostructures”, Appl. Phys. Lett. 85 (2004) 582.

[Sch05] H. Schmidt, G. Borchardt, C. Schmalzried, R. Telle, H. Baumann, S. Weber, H. Scherrer, "Self-diffusion of transition metals in (Ti W Cr)B_2 solid solutions", J. Mater. Sci., in print.

[Spi98] C. Spinella, S. Lombardo, F. Priolo, "Crystal grain nucleation in amorphous silicon", J. Appl. Phys. 84 (1998) 5383.

[Star97] M. J. Starink, "Kinetic equation for diffusion-controlled precipitation reactions", J. Mater. Sci. 32 (1997) 4061.

[Sto95] D. Stoyan, W. S. Kendall, J. Mecke, Stochastic Geometry and its Applications, second edition (Chichester, West Sussex, Wiley).

[Str93] A. Strecker, U. Salzberger, J. Mayer, "Specimen preparation for Transmission Electron Microscopy: reliable method for cross-sections and brittle materials", Prakt. Metallogr. 30 (1993) 482.

[Tan85] T. Y. Tan, U. Goesele, "Point defects, diffusion processes, and swirl defect formation in silicon" Appl. Phys. A37 (1985) 1

[Tel68] V. S. Telegus, Y. B. Kuz'ma, "Phase equilibria in the system tungsten-chromium-boron and tungsten-molybdenum-boron, Poroshk. Met. 68(2) (1968) 133.

[Tel92] R. Telle, E. Fender, G. Petzov, "The quasibinary systems CrB_2-TiB_2, CrB_2-WB_2, and TiB_2-WB_2", J. Hard Mat. 3 (1992) 211.

[Ueb96] P. Uebele, H. Hermann, "Computer simulation of crystallisation kinetics with non-Poisson distributed nuclei", Modelling Simul. Mater. Sci. Eng. 4 (1996) 203.

[Va97] P. Vavassori, F. Ronconi, E. Puppin, "Surface crystallisation and magnetic properties of amorphous $Fe_{80}B_{20}$ alloy", J. Appl. Phys. 82(12) (1997) 6177.

[Vas00] J. Vasquez, P. L. Lopez-Alemany, P. Villares, R. Jimerez-Garay, "Generalisation of the Avrami equation for the analysis of non-isothermal transformation kinetics. Application to the crystallisation of the $Cu_{0.20}As_{0.30}Se_{0.50}$ alloy", J. Phys. Chem. Sol. 61 (2000) 493.

[Wat86] T. Watanabe, H. Miura, Y. Tokuma, "Densification mechanis of TiB_2-1% CoB and TiB_2-5% TaB_2-1% CoB systems", J. Jpn. Soc. Powder Metall. 33 (1986) 38.

[Wei96] M. C. Weinberg, "Avrami exponents for transformations and producing anisotropic particles", J. Non-Cryst. Solids 202 (1996) 290.

[Wer50] C. Wert, C. Zener, "Interface of growing spherical precipitate particles", J. Appl. Phys. 21 (1950) 5.

[Wil92] W. P. Press, S. A. Teukolsky, W. T. Vetterling, B. P. Flannary, "Numerical Recipes in C", 2nd Ed., Cambridge University Press, Cambridge, (1992).

[Wol91] S. Wolfram, “Mathematica: A system for doing mathemathics by computer”, 2nd Ed. (Addison-Wesley Publ. Co., Redwood City, (1991).

[Yak01] R. Yakinova, M. Syväjarvi, T. Iakimov, H. Jacobson, A Kakanakova-Georgieva, P. Raback, E. Janzen, “Growth of silicon carbide: process-related defects”, Appl. Surf. Sci. 184 (2001) 27.

[Yu00] M. B. Yu, Rusli, S.F. Yoon, S.J. Xu, K. Chew, J. Cui, J. Ahn, Q. Zhang, “Hydrogenated nanocrystalline silicon carbide films synthesized by ECR-CVD and its intense visible photoluminescence at room temperature”, Thin Solid Films 177 (2000) 377.

[Zha00] H. Zhang, B. S. Mitchell, “A method for determining crystallisation kinetics parameters from one non-isothermal calorimetric experiment”, J. Mater. Res. 15(4) (2000) 1000.

CURRICULUM VITAE Dr.-Ing. Edith Roland Fotsing

Name: Fotsing, Edith Roland.
Date of Birth: July 03, 1975.
Nationality: Cameroonian.
Status: Single, 1 Child.

EDUCATION

01/2002 – 03/2005	**PhD** at the Clausthal University of Technology (Germany). Institute of metallurgy. Research group of **Prof. Dr. -Ing. Günter Borchardt**
09/2000 – 03/2001	German course: German as foreign language, ***DSH examination***
09/1997 - 08/2000	University of Yaounde I. Faculty of science. Department of physics (Cameroon) - ***DEA*** in quantum and solid mechanics (April 2000) - ***Masters of Sc.*** in mechanics and theoretical physics (April 1999)
09/1994 – 09/1997	University of Douala. Department of physics (Cameroon) - ***Bachelor of Sc.*** in physics, June 1997
06/1994	- **University entrance diploma**

WORK EXPERIENCE

04/2001 –02/2005	Clausthal University of Technology, Institute of metallurgy ***Scientific Co-worker***
09/1998 – 09/2000	University of Yaounde I, Department of physics (Cameroon) ***Scientific Co-worker***, quantum and solids mechanics

LANGUAGES

French	Native speaker
German	read, write and speak good
English:	read, write and speak satisfyingly

HOBBIES

Sport, movies, reading and journeys

Acknowledgements

Writing a PhD thesis is truly a difficult task, and I would not have been able to achieve this goal without the aid and support of countless people over the past four years.

I must first express my gratitude towards my advisor, Prof. Dr.-Ing. Günter Borchardt, who gave me the opportunity to do this work. His leadership, support, attention to detail, hard work, and scholarship have set an example.

Very special thanks to Dr. Harald Schmidt, whose expertise, understanding, and patience, added considerably to my graduate experience. I appreciate his assistance in the preparation of all experiments and in writing publications. His advice, motivation, encouragements and moral support in periods of hesitation were determinant.

I would also like to thank Prof. Dr.-Ing. Jürgen G. Heinrich, who promptly accepted to be the second reviewer of this work.

Many thanks to Prof. Dr. rer. nat. Rainer Telle and Dr. Clemens Schmalzried of RWTH Aachen (Germany) for the preparation of the (Ti, W, Cr)B_2 solid solutions.

I must also acknowledge Dr. M. Bruns (Research Centre Karlsruhe) and Dr. H. Baumann (University of Frankfurt) for the preparation and the characterization of the amorphous SiC films.

My gratitude goes also to Dr. Sébastien Chevalier and Dr. Rémy Chassagnon of the University of Burgundy (France) who helped in the preparation and the execution of TEM experiments.

I would like to thank E. Ebeling for the preparation of the samples and for the technical support and A. Mühlhan for her assistance in SEM and EDX analyses. I am also grateful to Dr. P. Klein (Rechenzentrum) for helpful discussions in relation to the numerical calculations.

It was really a pleasure to work within the group of thermochemistry and microkinetics, whose characteristics are aid, solidarity and efficiency. I will never forget this wonderful ambiance. Special thanks to all of you.

Many thanks to all my friends for their support and encouragements.

I would also like to thank my family for the support they provided me through my entire life and in particular, I must acknowledge my life partner, Rosine, my daughter, Jessica Carmen, my mother, Makoudjou Odette and my uncle, Mr. Fotsing Marcel, without whose love, encouragements and support I would not have finished this thesis.

Finally, I would like to dedicate this work to my late father.